Multi-band Studies of Blazars with *XMM-Newton*

A THESIS

SUBMITTED TO GAUHATI UNIVERSITY FOR THE DEGREE
OF DOCTOR OF PHILOSOPHY IN PHYSICS IN THE
FACULTY OF SCIENCE

By

Nibedita Kalita

Department of Physics, Gauhati University
Guwahati – 781014, Assam, India
&
Aryabhatta Research Institute of observational sciencES (ARIES)
Manora Peak, Nainital – 263002, India

November 2016

Dr. Kalpana Duorah
Retired reader
Department of Physics, Gauhati University, Guwahati–781014
Email: khowang56@yahoo.co.in
Phone: +91 9864030857 (M)

CERTIFICATE

This is to certify that **Nibedita Kalita** has worked under my guidance and co-supervision for this thesis. The research work reported in this thesis is original and candidate's own work. She has fulfilled all the requirements for submission of her thesis, as per the Ph.D. regulations of Gauhati University.

This thesis has not been submitted for the award of any degree, diploma, associateship or fellowship of any other University or Institute.

Place: Guwahati
Date:

Dr. Kalpana Duorah
(Supervisor)

Dr. Alok Chandra Gupta
Scientist–E
Aryabhatta Research Institute of Observational Sciences (ARIES),
Manora Peak, Nainital–263 002, India
Email: alok@aries.res.in (official), acgupta30@gmail.com (personal)
Phone: +91 5942 270709 (O)

CERTIFICATE

This is to certify that **Nibedita Kalita** has worked under my guidance for this thesis. The research work reported in this thesis is original and candidate's own work. She has fulfilled all the requirements for submission of her thesis, as per the Ph.D. regulations of Gauhati University.

This thesis has not been submitted for the award of any degree, diploma, associateship or fellowship of any University or Institute.

Place: Nainital
Date:

Dr. Alok Chandra Gupta
(Co-Supervisor)

Declaration

I hereby declare that the work presented in this thesis entitled **"Multi-band studies of blazars with XMM-Newton"** is a result of my own investigation conducted under the supervision of Dr. (Mrs.) Kalpana Duorah, Department of Physics, Gauhati University, Guwahati and Dr. Alok Chandra Gupta, Aryabhatta Research Institute of observational sciencES (ARIES), Nainital. No part of this thesis has been submitted for the award of any degree, diploma, associateship or fellowship of any other University or Institute.

Place : Guwahati
Date : (Nibedita Kalita)

Acknowledgements

At the very beginning I take this opportunity to express my heartfelt gratitude and indebtedness to all those individuals who accompanied me during my Ph.D. journey, who provided advice, guidance, encouragement and friendship, and helped me to overcome all the difficulties and obstacles that I came across. I would like to begin this thesis by expressing my sincere thanks to all these people.

First of all I wish to acknowledge my supervisor, Dr. Kalpna Duorah, Dept. of Physics, Gauhati University for the significant effort she has put into supervising me during my Ph.D. tenure. Her endless support and constant encouragement have made this journey so wonderful and pleasant.

I am equally indebted to my co-supervisor, Dr. Alok C. Gupta (ARIES), for being endlessly generous with his time and expertise. I particularly thank him for providing enthusiasm and direction to my research work and also for his endless support in excelling my research career.

I sincerely thank Director, ARIES for providing all the facilities at ARIES that supported my research work and for establishing the observational facilities.

I am also indebted to Prof. A. Gohain Barua, Head, Department of Physics, Gauhati University for always keeping a positive attitude towards me and providing necessary Departmental Laboratory and Library facilities during the course of my study.

I deeply thank Prof. H. L. Duorah Sir for his suggestions, comments and encouragement which helped me a lot to improve my scientific outcomes. I particularly

enjoyed all those inspiring and mind stimulating discussions we had, at our Dept. in Gauhati University.

I express my heartfelt gratitude and indebtedness to the organizing committee of the **2nd IUCAA X-Ray Astronomy School**, held at IUCAA in 2013 which introduced me to X-ray astronomy and improved my research orientation. I particularly thank Dr. Gulab C. Dewangan and Dr. Ranjeev Mishra for improving my understanding in this framework.

I would also like to express my gratitude to Prof. Paul J. Wiita from Department of Physics, The College of New Jersey, Ewing, USA, for his help in understanding the AGN Physics and providing the necessary advice in time of need.

I thankfully acknowledge Department of Science & Technology (DST) for supporting my initial work with a fellowship grant under the project "Photometric and Spectroscopic Study of RSCVn Stars and Study of Active Galaxies through Archival Data." which was supervised by Dr. H. L. Duorah as PI (2009–2012) and for funding my research work during 2014–2016 under the Women Scientist Scheme-A (WOS-A). In this context I would like to thank Dr. HB Singh, the Officer-in-charge of WOS-A and Dr. Vandana Singh Scientist-D (DST) for their help and support.

I am thankful to Mr. Bharat Singh, Assistant Registrar of ARIES, Nainital for his support and help in undertaking the WOS-A project at ARIES. I would also like to thank Abhisekh K. Sharma, Vijay Meena, Hemant Kumar, Pavan Tiwari, Mohit Joshi, the Library staff & the administrative staff of ARIES, for their support and friendly and harmonic environment I needed.

I thank all my colleagues (Jai, Aditi, Ashwini, Vishi and Yugam) at ARIES and (Jayashri Medhi) at Dept. of physics, Gauhati University for fruitful discussion and timely help and also thank Arti and Shubhajeet for their company, support and for the discussions related to X-ray data analysis at ARIES. I would also like to thank Mridweeka for her help during my observing nights with 40 inch telescope

at ARIES and all others who directly or indirectly help me to carry out this research.

A special thanks to Raman for his continuous help, support and encouragement in the time of need during my stay at ARIES. I particularly enjoyed our evening walks, talks and all those tea and dinner parties. Those are memories to be cherished.

I am out of words to express my gratitude toward my parent and my brother Diganta & all the family members. Without their constant support and inspiring words, research wouldn't have been possible for me. My heartfelt gratitude goes to my best friends Santana for her endless support and friendly advices during the difficult days in this journey.

Nibedita Kalita

Abstract

Blazars are sub-class of the radio-loud Active Galactic Nuclei (AGN), which emit extremely luminous, polarized and non-thermal radiation covering the entire electromagnetic spectrum from a highly compact center (i.e., SMBH). The blazars with higher luminosity and jet angle are known as FSRQs (Flat spectrum radio quasars), while the BL Lac objects show comparatively low luminosity and smaller jet angle (in both cases the jet angle is $\leq 10^{\circ}$). Moreover, the SED synchrotron peak of FSRQs lies in the radio to optical range but for BL Lacs the synchrotron hump peaks in optical to X-ray range. One of the most interesting phenomenon that blazars show is the multi-frequency flux variation on diverse timescales. In the X-ray domain almost all blazars are strong emitters and it is found from studying emission line properties in X-ray spectra, that the X-ray emissions are coming from regions nearer to the SMBH. So, X-ray study of blazars can give deeper insight of the central engine improving our understanding of the source. In this thesis our aim is to understand different physical mechanisms involved with X-ray emission and to get better understanding of different variability properties observed in blazars. In order to investigate this we have undertaken two different approaches : (1) temporal study in multi-frequency domain and (2) X-ray spectral study. The whole work presented in this thesis is based on the blazar observations made by XMM-Newton observatory since its launch.

As part of the first approach, we have studied multi-band variability on Intraday and Long (years, during 2000-2012) timescales for the FSRQ 3C 273 and found that the source was not variable on intraday timescales in 0.3-10 keV X-ray band, but found to be highly variable on long timescales in optical, UV and X-ray bands. For the long term light curves flux variability increases with increasing frequency in optical/UV bands, but an opposite trend was observed for X-ray bands. A correlated variability study between optical, UV & X-ray bands revealed that, two electron populations with different Lorentz factors were involved in low and high energy emissions. Moreover, hardness ratio analysis in the X-ray regime indicates that the particle acceleration mechanism dominates the cooling mechanism during most of

the time ($\sim$ 12 years, 2000$-$2012).

In order to understand the relation between synchrotron peak of multi-frequency SED and the intraday variability in X-ray bands, a sample of blazars (including 10 LSPs and 2 ISPs) is also investigated. When considering the absence of X-ray IDV in LSP blazars, together with the high duty cycle of optical IDV in LSPs, a link can be drawn between presence/absence of IDV in these bands with the corresponding position of low energy peak of SED. Here we have proposed that since, X-ray bands lie below the peak of the SED of LSPs where inverse Compton mechanism is dominating rather than synchrotron radiation, the highest energy electrons available for synchrotron emission would have a retarded effect on X-ray variability in LSPs. Hence, reducing their intra-day variability in X-ray bands as compared to the variability in optical bands.

X-ray spectral study of the border line blazar 3C 273 in the energy range 2.5$-$10 keV (from 2000 through 2015) revealed some new information about the source. A new minimum flux state of 3C 273, even lower than the historical minimum during 2003$-$2004, was observed in 2015. A "harder-when-brighter" trend is observed in these long-term multi-epoch observations of 3C 273 for the first time. A significant detection of Fe K_α line at 5.8 keV during the historical minimum of the source indicates that the line was emitted from neutral matter near the disc moving with velocity $\sim$ 20,000 km s^{-1}. With simultaneous study of the X-ray continuum and optical/UV emissions during the low/quiescent state of the source, we have detected a significant anti-correlation between the X-ray spectral slope and the logarithm of the ratio of X-ray to optical/UV fluxes; however, the relation we have found is not applicable for flaring state of the FSRQ. From this detection we conclude that the 2.5$-$10 keV X-ray emission in 3C 273 is the result of inverse Compton scattering of soft seed photons (optical/UV) by highly energetic electrons in a thermal corona based above the accretion disc. The temperature of the hot gas is found to be 5.4 $\times$ 10^2 keV, while the optical depth (τ) varies between 0.16 to 0.23 with a covering factor (η) ranging between 0.0014 to 0.0031.

List of Publications :

In Refereed Journals : *(Related to Ph. D. Thesis)*

1. **Kalita, N.**; Gupta, A. C.; Wiita, P. J.; Bhagwan, J. and Duorah, K.,
Multiband variability in the blazar 3C 273 with XMM-Newton,
Monthly Notices of the Royal Astronomical Society, **451**, 1356−1365 (2015).

2. Gupta, A. C.; **Kalita, N.**; Gaur, H. and Duorah, K.,
Peak of spectral energy distribution play an important role in intra-day variability of Blazars?,
Monthly Notices of the Royal Astronomical Society, **462**, 1508−1516 (2016).

3. **Kalita, N.**; Gupta, A. C.; Wiita, P. J.; Dewangan, G. C. and Duorah, K.,
Origin of X-ray in the low state of the FSRQ 3C 273: Evidence of inverse Compton emission,
Monthly Notices of the Royal Astronomical Society, **Under Revision**, (2016).

In Refereed Journals : *(Others: Not Related to Ph. D. Thesis)*

1. **Kalita, N.**; Gupta, A. C. and Duorah, K.,
Search for QPO & variability timescales in a sample of ISP blazars in outburst state,
Under Preparation.

Notations & Abbreviations

All the notations and abbreviations have been explained on their first appearance in the text. The most frequently used notations and abbreviations are collected here for quick referencing. If a symbol has been used in a different connection than listed here, the same has been explained at the appropriate place.

AGN	Active Galactic Nuclei
B	Magnetic field
BBB	Big Blue Bump
BH	Black Hole
BL Lac	BL Lacertae objects
BLR	Broad Line Region
CCD	Charge Coupled Device
DCF	Discrete Correlation Function
EC	External Compton
EPIC	European Photon Imaging Camera
ESA	European Space Agency
FR I	Fanaroff−Riley type I
FR II	Fanaroff−Riley type II
FWHM	Full Width at Half Maximum
FSRQ	Flat Spectrum Radio Quasars
HSP	High synchrotron peaked blazar
HBL	High energy peaked blazar
IC	Inverse Compton
IDV	Intra-Day variability
kpc	kilo-parsec
LBL	Low energy peaked blazar
LSP	Low synchrotron peaked blazar
LC	Light Curve
LTV	Long Term Variability
NLR	Narrow Line Region
pc	Parsec

PSD	Power Spectral Density
QPO	Quasi-Periodic Oscillation
RXTE	Rossi X-ray Timing Explorer
SED	Spectral Energy Distribution
SF	Structure Function
SSC	Synchrotron Self Compton
SMBH	Super Massive Black Hole
WEBT	Whole Earth Blazar Telescope
XMM	X-ray Multi Mirror

Contents

List of Figures

LIST OF FIGURES

LIST OF FIGURES

List of Tables

LIST OF TABLES

Chapter 1

Introduction

1.1 Active Galactic Nuclei

The spectra of most galaxies typically show absorption lines, and their emission are the combined output of gravitationally bound stars within them. It has been found that a small number of galaxies show broad and narrow emission lines superimposed on their spectra and have exceptionally bright central source which is often visible in all the wavelengths starting from radio to γ-rays. Most of the time the extremely luminous core outshines the host galaxy, resulting in star-like appearance of the galaxy. These special type of galaxies are called active galaxies and their highly luminous nuclei are termed as "Active Galactic Nuclei" or in short "AGN". The power emitted by an active galaxy is comparable to that emitted by several thousands of normal galaxies.

AGN are one of the most powerful and luminous objects in the universe, which emit an enormous amount of energy covering the entire electromagnetic spectrum from a very compact, tiny region reaching bolometric luminosities of $10^{40}-10^{48}$ ergs s^{-1}. Their emission is predominantly of non-thermal origin and cannot attributed to the stellar emission. AGNs show highly variable emission in all frequencies, on time scales of hours, days, to years, which infer that these radiations are coming from a very small region having size comparable to the Solar System. These facts lead to the hypothesis, which is now widely believed, that the supermas-

sive black holes (SMBHs) having mass of the order of $\sim 10^6 - 10^9$ $M_\odot$ are present in the central power-house, and the strong nuclear radiation from AGN is due to the accretion of matter onto such black holes.

1.1.1 A Brief History of AGN

Optical spectrum of an active galaxy was first obtained by Edward A. Fath in 1908 at Lick Observatory while analyzing the spectrum of the nebula NGC 1068 and he observed that the spectra contains strong emission lines (Fath, 1909). Later, a high resolution spectra of the same object was studied by V. M. Slipher, who found that these lines are resolved and very broad, having widths of the order of 10^2 kms^{-1} (Slipher, 1917). In 1943, Carl Seyfert discovered that there are several similar kind of galaxies which possess broad emission lines in their spectra and realized that these objects form a distinct class of galaxies showing high excitation nuclear emission lines, covering a wide range of ionization states and composing of a luminous quasi-stellar nuclei. Later, this class was named as *Seyfert galaxies* (Seyfert, 1943). An interesting discovery was made in 1955 when the two Seyfert galaxies, NGC 1068 and NGC 1275 were detected as radio sources, attracting the attention of astrophysicists. The first attempt to understand the physics of Seyfert galaxies was made by Woltjer (1959), who studied these objects and found that the centre of these galaxies are not resolvable yields being smaller than 100 pc, the emission lines are emitted from a low density gas and mass of the central source is in the order of $\approx 10^{9\pm1}$ $M_\odot$.

Quasars were originally discovered in the first radio survey of the sky in late 1950s (Edge et al., 1959). After that, several radio sources were discovered in succeeding radio surveys. Some of them contain optical counterparts and they looked like normal stars however, unlike stars their photographic spectra showed very broad strong emission lines and their photometric study revealed that these sources are anomalously blue as compared to normal stars. Another radio source, 3C 273 with stellar-like appearance was discovered in 1963 and over a lunar occultation of the source resulted in precise determination of its position, as well as its structure being a two-component system (Hazard et al., 1963). In a contemporary study of the

source carried out by Maarten Schmidt detected that the emission line in the optical spectra of 3C 273 are hydrogen Balmer lines and MgII lines at a surprisingly high redshift $z = 0.158$. This was among the highest redshift ever measured at that time and was larger by an order than those of Seyfert galaxies (Schmidt, 1963). Later, these objects were named as quasar (stands for quasi-stellar radio sources, QSR) due to their stellar like appearance.

BL Lacertae also known as BL Lac were first discovered in 1929 by Cuno Hoffmeister in the constellation Lacerta. Originally it was thought to be a variable star because of its stellar-like appearance with variable brightness which was later detected in radio survey (Schmitt, 1968) and identified as AGN. In addition to highly variable surface brightness, the source showed featureless optical continuum and high degree of polarization in both optical and radio bands. Later, many sources with similar characteristics were identified and they were categorized as a new class of AGN, BL Lacertae or BL Lacs.

Currently, the AGN phenomenon is a vast topic and an exciting research field. The enormous luminosity of these objects yields extreme physical environment which is not found elsewhere in the nearby universe. The extremely luminous and high redshift quasars can be used as cosmological probes to understand the evolution of the universe. Researchers are exploring in different regime, such as, the interaction between clusters of galaxies and AGN jet, how the AGN jet outflows affect the star formation and galaxy evolution to fully understand the link between different astronomical phenomenon in order to visualize the broader picture. The physical structure, different observational properties and broad-band emission of AGN are discussed in the following sections.

1.1.2 The Physical Picture of AGN

AGN produce emissions of the order of several trillion stars in a volume smaller than a cubic parsec, thus implying an enormous mass concentration of the AGN. The current paradigm for the AGN phenomenon is a central supermassive black hole (SMBH, $\sim 10^6 - 10^9$ $M_\odot$) surrounded by an accretion disk of matter which

powers up the AGN. In the following subsections, main components of AGN are briefly discussed. A schematic picture of an ideal radio-loud AGN is displayed in the Fig. 1.1.

1.1.2.1 Supermassive Black Hole (SMBH)

A BH is an extremely compact object formed due to gravitational collapse of a massive star at the end of their life cycle, which satisfy the condition M $\geq 3M_{\odot}$, and characterized by only three parameters: mass, spin and charge. After a BH has formed it can continually grow by accreting dust and particle from its surrounding, or by absorbing nearby stars and by merging with other BHs. The rate of growth of a BH is defined by their mass and availability of matter in the host galaxy. A BH is termed as supermassive black hole (SMBH) when its mass crosses the limit of 10^6 $M_{\odot}$. Although BH has no physical surface their characteristic size can be defined in terms of Schwarzschild radius R_S, which is the event horizon for a non-rotating BH (Peterson, 1997) and is given as

$$R_S = \left(\frac{2\,G\,M_{BH}}{c^2}\right) \tag{1.1}$$

Where, M_{BH} is the BH mass and G is the gravitational constant. In general, all the distances around a BH are presented in terms of Schwarzschild radius as $R_S \propto M_{BH}$, where the distance measurements are scaled to R_S.

1.1.2.2 Accretion Disc

Accretion of matter onto a supermassive black hole is the most efficient energy extracting process from mass and also the foremost way to power the AGN. It is believed that the infalling gas has finite angular momentum (due to its rotation) and consequently instead of falling straight onto the BH, it will assemble in a disk-like structure through friction with other gas particles and by resulting momentum transfer, which is oriented perpendicular to the angular momentum vector; rotating with Kepler velocity (Schneider, 2006). The gas in the disk rotates differentially and the internal friction cause small deceleration of the rotational velocity, due to which the gas will slightly move inwards. In this process gravitational potential energy will be

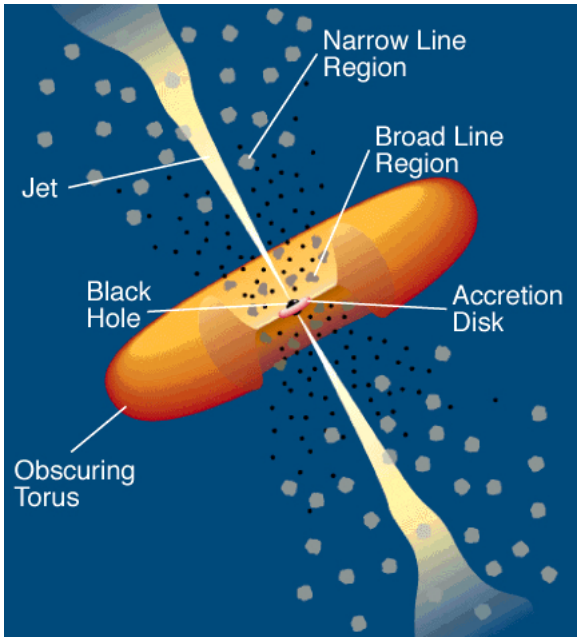

Figure 1.1: A schematic diagram of broadly accepted model for radio-loud AGN provided by Urry & Padovani (1995). The main constituent components of AGN are shown in the figure.

released at the rate $GM\dot{m}/r$ (according to conservation of potential energy), where, $\dot{m}$ is the mass accretion rate and other symbols have their usual meaning. Half of this released energy is used in heating the gas and the other half is radiated away. The thermal radiation emitted from this accretion disk is responsible for most of the optical, UV and soft X-ray continuum emission in AGNs (Peterson, 1997; Schneider, 2006).

The detailed structure of the disk is governed by different parameters, e.g., the magnetic field strength, $\dot{m}$ and the presence or absence of jets. There are many parameters like, viscosity of the rotating gas and role of thermal instabilities, which might play an important role to define the disk structure but our understanding about these parameters is limited. There are different models for accretion disk and among them the most simple one is the geometrically thin and optically thick disk provided by Shakura & Sunyaev (1973), whose spectrum can be explained by a blackbody (radiation).

1.1.2.3 Broad emission Line Region (BLR)

Broad emission lines are the most interesting characteristic observed in the spectra of many AGN. These lines are interpreted through Doppler-broadening and the width of the line gives the velocity distribution of the gas in the emitting region which is generally measured in terms of the full width at half maximum intensity (FWHM). Width of these lines varies from object to object and ranges in between 500 km s^{-1} (still broader than majority of the the narrow lines) to $\geq 10^4$ kms^{-1}, with typical values $\approx$ 5000 km s^{-1} (Schneider, 2006). These lines cannot attributed to thermal line broadening for which an extremely high temperature of the order $T \sim 10^{10}$ K is required. At such high temperatures all atoms would be fully ionized, hence no emission lines would be emitted. Thus the emitting particles must be moving with very high velocity which cause the broadening. The gas clouds emitting these lines has large-scale velocities and resides at a distance of about 1000 R_s ($\sim$ 1 parsec) from the centre. This region is called as broad-line region (BLR). The density of the gas can be measured from the allowed and semi-forbidden lines emitted from the BLR region and is found lie in the range $\sim 10^9 - 10^{12}$ cm^{-3}. The ionization states of the line emitting gas indicates that the temperature of the gas is of the order of $\sim 10^4$ K (Peterson, 1997).

1.1.2.4 Dusty Torus

Outside the accretion disk and BLR, there is a region of thick gas and dust particles in the shape of doughnut, residing on a scale of one to few parsec in the radial direction of the accretion disk. This dust wrapped structure is known as dusty torus and is the main cause for the observed differences between Type 1 and Type 2 AGN. This gas belt blocks the radial emission coming from the accretion disk and absorbs the optical/UV photons coming from the nucleus and re-radiate it in (near) infrared frequencies. It is also one of the main supply source for matter which eventually falls onto the SMBH. The presence of an optically thick, dusty structure in the local environment of the SMBH was first proposed by Antonucci (1993) to interpret the observed differences between the two types of AGN.

1.1.2.5 Narrow emission Line Region (NLR)

Beyond the dusty torus, there are gas clouds moving with slower velocity around the central engine. Apart from the broad emission lines, most of the AGN spectra contain narrow emission lines whose FWHM lies in the range $200 \leq \Delta v_{FWHM} \geq 900$ kms^{-1} with a typical width of 400 kms^{-1} (still broader than characteristic velocities in normal galaxies). This line emitting region is known as narrow line region (NLR) and it resides at distance of ~ 1 kilo parsec from the central BH covering a spatial region extent up to ~ 100 pc. Due to the large extent of NLR, it is the only AGN component which can be spatially resolved for nearby Seyfert galaxies, in optical bands. It has been found that the shape of the NRL is not spherical but two cone-shaped. The particle density in NLR is lower than the BLR region and is low enough to emit forbidden lines. From these lines the density and temperature of the gas are estimated, whose average values are typically $\sim 10^3$ cm^{-3} and $T \sim 16000$ K, respectively (Koski, 1978).

1.1.2.6 Relativistic Jet

Some AGN, mainly the radio-loud one possess jet like features emerging from the nuclear region of the BH. These are highly collimated extended linear structures, which carry out radiation and plasma of energetic particles from the core to the outer space. The outflow of energy occurs along the two poles of the accretion disk and in most cases, the extended bipolar jets terminate into double structure in the form of giant radio lobes. These radio sources can extend from a few hundred kpc to 1 Mpc. In most of the cases, only one sided jet is observed and if two sided jets are present than one of them is much weaker than the other, which is a consequence of Doppler boosting effect. Jets are highly complicated and asymmetric in nature which have its own internal structure such as knots and kinks. They may accelerate to relativistic speed which is probably caused by combination of high gravitational fields near the SMBH and rapidly rotating strong magnetic fields which are anchored in the accretion disk. The rotating magnetic field lines (due to rotation of accretion disk) generate a helical shape which is assumed to be the reason behind highly focused jets. Jets can amplify and concentrate the continuum emission along the directions perpendicular to the disk. A model for the relativistic jet in AGN is shown in the

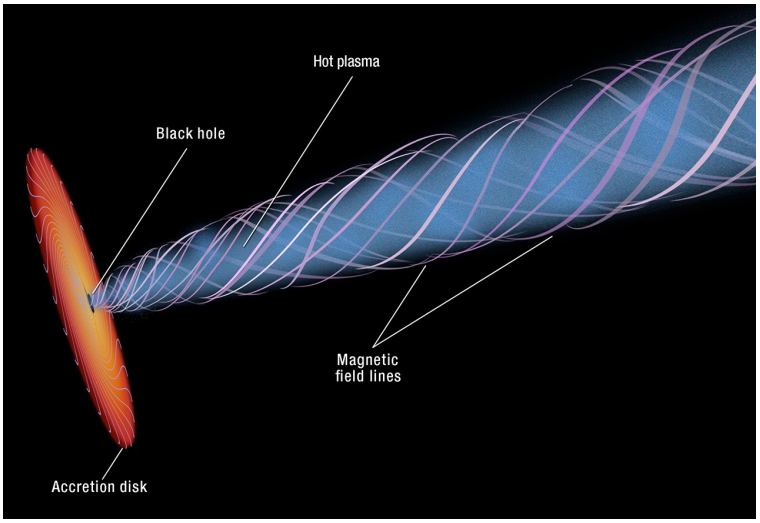

Figure 1.2: An illustration of relativistic jet model. The accretion disk that rotates around a SMBH generates strong magnetic fields which propel radiation and material from the disk to the extragalactic medium in favourable conditions. Image Credit: NASA, ESA, and A. Feild.

Fig. 1.2. A more detail description on AGN jet can be found in Blandford & Königl (1979); Harris & Krawczynski (2006); Marscher (1996).

1.1.2.7 Hot Corona

In addition to the above discussed components, BH systems often have a plasma layer of hot electrons associated with them, known as the "corona". The exact geometrical shape and nature of this sea of charged particles is not clear, though possible options are, a layer of hot electrons above and below the accretion disk (sandwich-type), or patches of hot electrons generated by magnetic reconnections like in the corona of the sun or perhaps a more-or-less spherical appearance (Paczynski, 1978). Alternatively, since BHs are often associated with bipolar jets, the plasma we assumed as coronal material may be charged particles in the base of such jets. Fig. 1.3 displays different possible geometries for the corona that are usually considered to describe the observed emission (Reynolds & Nowak, 2003). The X-ray spectra of some AGN show a hard power-law component (above 0.5 keV) in the form of $F_E \sim E^{-\tau}$, which can not be attributed as an extension of the blackbody component (due to the disk) to X-ray energies. This component is thought to

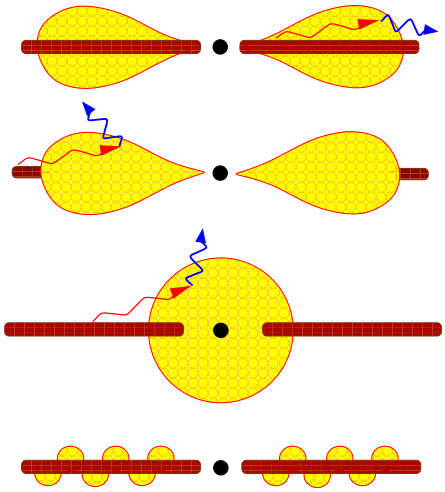

Figure 1.3: Possible geometries for a simple AGN corona are depicted in the above diagram. From top to bottom, the corona configuration is seen sandwiching the inner disk, truncating the inner disk, surrounding the inner disk isotropically, and existing in a patchy form around the disk as a pill-box. Spectra that are softer than generally observed for AGNs are explained by the top geometry. The other configurations are used to describe a photon-starved corona which is less effectively cooled by inverse Compton scattering of disk photons. Credit: Reynolds & Nowak (2003)

be produced by inverse Compton scattering of highly energetic electrons residing above the accretion disk in the form of a "hot corona".

1.2 AGN Taxonomy

AGNs are characterized by their bright cores, which outshine the host galaxy most of the time. Although AGN exhibit observable feature by which they could be subdivided into different groups, their classification tends to be complicated due to the large variation in the degree to which each feature is exhibited in different AGN. For instance some AGN possess radio jet while others do not, some show very rapid flare in different wavebands while comparatively some are extremely calm or steady.

The first classification used for AGNs was based on radio and optical properties of the sources. According to this, AGNs are broadly divided in to two subgroups:

radio-loud and radio-quiet AGN, depending on the *radio-loudness factor*, R_L, which is defined as the logarithm of the ratio of radio flux at 5 GHz, $F_{5\ GHz}$ to the optical B-band flux, F_B of the source, which is defined as,

$$R_L = log\left(\frac{F_{5\ GHz}}{F_B}\right) \tag{1.2}$$

AGNs with $R_L \geq 1$, belong to the radio-loud class and those with $R_L < 1$, are called radio-quite AGN (Kellermann et al., 1989). However, This ratio increases with optical and X-ray luminosity of the source (Della Ceca et al., 1994; Padovani, 1993). Around $10-15$ % of AGN are radio-loud. Here, radio-quiet does not mean that the object is necessarily radio-silent; it can still show a certain amount of radio emission. Radio-quiet and radio-loud AGN are further sub-classified based on their optical and ultraviolet spectra. Those with bright continua and broad emission lines are called Type-1 AGN, and Type-2 AGN are those which show weak continua and narrow emission lines (Lawrence, 1987, 1993). There is a small group of AGN which show unusual spectral behaviour, absent or very weak emission or absorption lines in their spectra. They also show very rapid variability, unusually high and variable polarization, superluminal motion of the compact radio core and extreme luminosity. This class of AGN is termed as Type-0 AGN, which includes the BL Lac objects and Quasars (Padovani & Giommi, 1995).

The different classes of AGN based on above classifications are briefly summarized below. Figure 1.4 displays typical optical spectra of different types of AGN.

Seyfert Galaxies– These are nearby low luminosity AGN, hence the host galaxy is clearly detectable, which tends to be spiral. They have massive galactic bulges with high central surface brightness and an interstellar medium. They usually possesses high-ionization emission lines and the line properties can be different in different Seyfert galaxies; Seyfert 1s and Seyfert 2s (Sy1s and Sy2s) (Khachikian & Weedman, 1974). The optical spectra of Seyfert 1s shows both narrow and broad emission lines superposed on one another, on the other hand Seyfert 2s spectra contain only narrow lines (see Fig. 1.4). In addition to the emission lines, weak absorption lines are also observed in the spectra of both Sy1 and Sy2, which corre-

sponds to the late-type stars in their host galaxies.

Quasars– Quasars (Schmidt 1963) are the most luminous of the AGN family, with a bolometric magnitude, $M_{bol} \approx 23$, and can now be seen out to redshifts, $z > 6$. quasars are basically similar to Seyfert galaxies but with higher brightness, where the nucleus is much more luminous than the host galaxy becomes faded as compared to the core (can be > 100 times fainter than the nucleus), hence undetected. Majority of the quasars lies in the radio-quite category ($\sim 90-95\%$). The difference between the spectra of Quasars and Seyfert galaxies is that the absorption lines in the spectra of quasars are very weak, if detectable at all, quasars show high variability and the emission lines are weaker relative to that in Seyferts (Peterson, 1997).

Radio Galaxies– These are strong radio sources, typically detected with giant elliptical galaxies. There are two types of radio galaxies which show AGN activity; the broad-line radio galaxies (BLRGs) and the narrow-line radio galaxies (NLRGs). The BLRGs and NLRGs are thought to be the radio-loud analogues of Sy 1 and Sy 2 galaxies, respectively. Although radio galaxies are considered, in some senses, to be radio-loud Seyferts, as a class they have number of features and differences from their radio-quite counterparts (i.e., Seyfert galaxies). NLRGs include two distinct types of object with different morphology: the low-luminosity Fanaroff-Riley type I (FR-I) and the high-luminosity Fanaroff-Riley type II (FR-II) radio galaxies (Fanaroff & Riley, 1974). FR-I objects show often radio jet and they are brightest in the centre, with the surface brightness decreasing outwards, while FR-II type objects have more highly collimated jets which leads to well defined lobes and are brighter further away from the nucleus.

LINERs– LINER stands for Low Ionization Nuclear Emission-Line Region galaxies and was identified by Heckman (1980). LINERs are the least luminous of the classifications and are very common, might be present in nearly half of all spiral galaxies (Ho et al., 1994). Spectroscopically they seem line Seyfert galaxies but their spectra contain low ionization lines, e.g. [O I] and [N II]. Nuclear activity of these these galaxies are very poor and as a result the emission coming from them

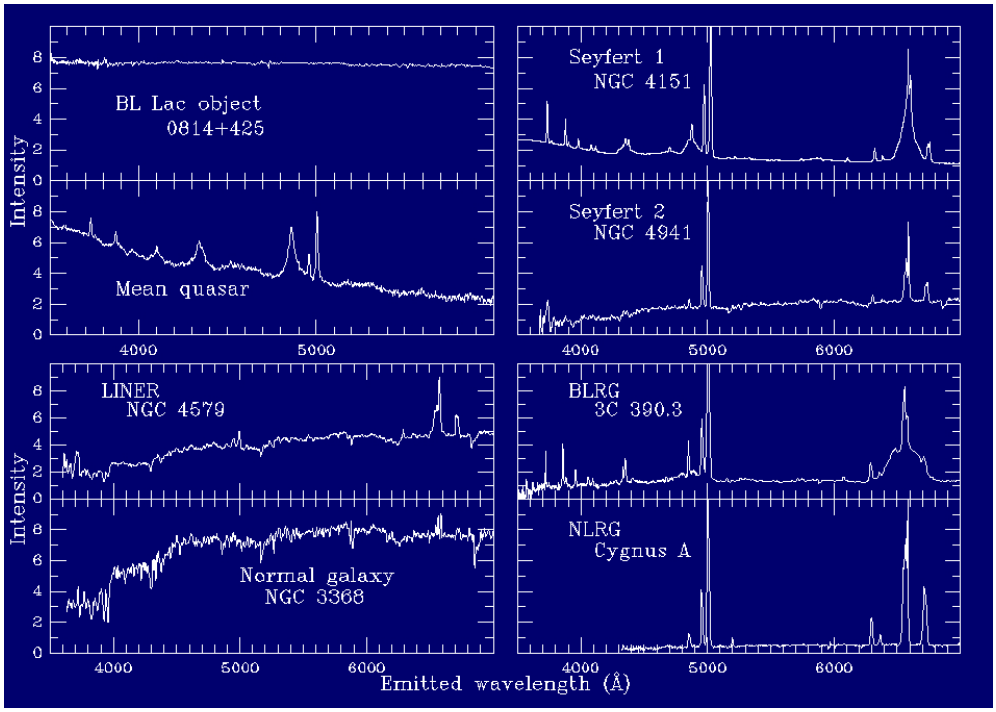

Figure 1.4: The above plot shows typical optical spectra for the different classes of AGN. The spectra have been redshift corrected, so the lines observed are at their rest frame wavelengths. From the figure it is visible that the Type-1 AGNs contain both broad and narrow emission lines, while Type-2 AGNs show narrow profiles only. Image taken from the website, at http://www.astr.ua.edu/keel/agn, based at the University of Alabama.

are dominated by starlight. These are classified as AGN due to the presence of non-stellar continuum in the emission line spectra. The observational difference between LINERS and other AGNs (Seyfert galaxies) is the relative strength of certain low-ionization lines e.g., [O III] λ5007 / H_β, [N II] λ6583 / H_α and [S II] λ6716 / H_α flux ratios (Peterson, 1997).

Blazars– Collectively, BL Lacs and flat spectrum radio quasars (FSRQs) are referred as Blazars, forming a very small subset of the AGN family. Only $\sim 1\%$ of radio-loud AGNs falls in this class and are related to a small jet angle w.r.t. our line of sight. Unlike other AGNs, these objects show abnormally large continuum variability in tiny timescales in certain wavelengths. They show high linear polarization which also varies in magnitude and position angle. BL Lacs objects either don't

show or show very weak emission lines whereas FSRQs show prominent emission lines in their spectra. However, high resolution spectroscopy indicates presence of weak stellar absorption features or weak nebular emission lines (Peterson, 1997). The possible host galaxy of blazars is elliptical galaxy (Urry et al., 2000).

1.3 The Unification Model

The idea of unification for different types of AGN is based on the evidence for anisotropy found in radio and high frequency emission which implies that the appearance of an AGN is highly dependent on the orientation of the axis of symmetry relative to our line of sight (see Antonucci, 1993, and references therein) implying that the classification of the nuclei might be function of the viewing angle.

Observational evidence of similar properties were found in different classes of AGN. The evidence of similar feature in Type I and type II Seyfert was reported by Osterbrock (1978), suggesting that the Seyfert 1s and Seyfert 2s are physically the same objects. The presence of very broad Sy1-like Balmer lines in the classical Sy2 galaxy NGC 1068, was reported by Antonucci & Miller (1985), when viewed in polarized light. Later, different studies discovered similar type of Sy2 which strengthen the idea that Sy1 and Sy2 galaxies are essentially identical, but observed at different angles. Scheuer & Readhead (1979) suggested that the radio-loud quasars were a counterpart of radio-quiet quasars which were more aligned to our line of sight. Later, It was suggested that the FSRQs are beamed versions of SSRQs (Orr & Browne, 1982). Another suggestion was made by Barthel (1989), where they linked SSRQs and FSRQs, as increasingly aligned version to FR II galaxies. BL Lacs, the sub-class of blazars which possess relatively narrow emission lines as compared to FSRQs, were thought to be more aligned version of quasars (Blandford & Ostriker, 1978). A detail picture of unification in radio-loud AGN was provided by Urry & Padovani (1995), where they have interpreted the isotropic properties between quasars & FR II type galaxies and BL Lacs & FR I type galaxies. Quasars (FSRQs and SSRQs) & FR II found to be showing similar extended radio luminosities at a few GHz and nearly similar narrow line emission luminosity while, these similarities were not clear between BL Lacs & FR II, but it was found that the

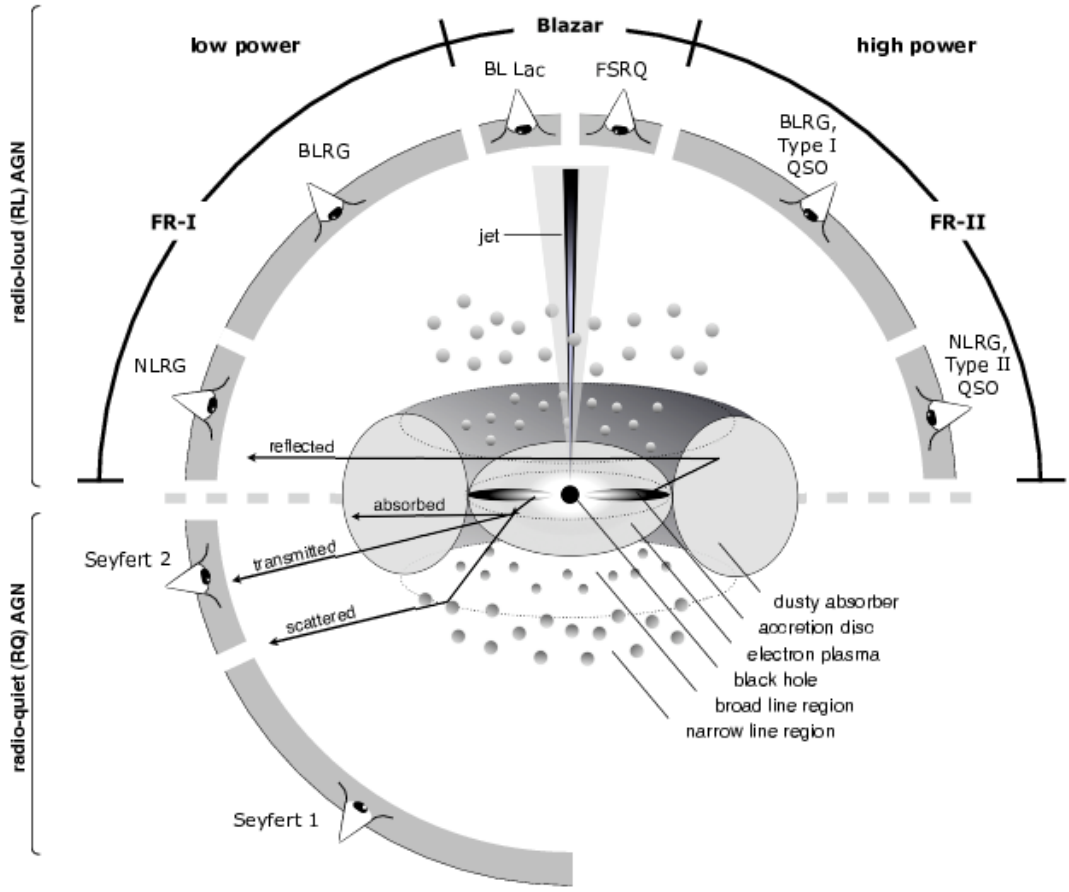

Figure 1.5: A schematic representation of the unified scheme for the AGN phenomenon taken from Beckmann & Shrader (2012) (graphic by Marie-Luise Menzel, MPE). The different classes of AGN are shown corresponding to different geometric orientations of the nucleus w.r.t. our line of sight. The upper part of the diagram, displaying jet emission contains all the radio-loud AGN, while the lower part without jet represents all the radio-quite AGN.

low-redshift BL Lacs reside in giant ellipticals as FR Is do, which means their host galaxies are same (Urry & Padovani, 1995).

According to the unified model, the key elements which control the observed diversity of AGN are the obscuring torus and relativistic jet. If the AGN is observed along the edge-on direction, then the dusty torus obscures the radiation coming from the central engine and at large angles nearer to radial direction, it would hide the BLR completely. In this case the resulting spectrum of an AGN possesses narrow emission lines emitted by the NLR e.g., Seyfert 2s and NLRGs. On the other hand, if the AGN is observed face-on, the BLR and the accretion disc related emission will be visible and the observed spectrum is featured by broad emission lines e.g. Seyfert 1s and BLRGs. The radio properties of AGN are characterized by relativistic jets, presence of these jets give rise to radio-loud AGN, while AGN without or very weak jet are classified as radio-quiet AGN. The diverse properties of different radio-loud AGN are based on the angle between the jet axis and direction of the observer. When we observe an AGN along its jet axis, relativistic beaming strongly amplifies the observed properties like, luminosity, flux variation, polarization, superluminal motion and all the other properties. Examples of face-on version of radio-loud AGN are BL Lacs and OVVs with the BL Lacs corresponding to the low luminosity radio sources (FR I) and the OVVs (FSRQs) corresponding to the high luminosity radio sources (FR II). Figure 1.5 illustrates the basic concept of unified model and shows a quantitative way of aspect dependent classification of AGN.

The unification model does not explain some basic properties of AGN like: why some radio-objects possess strong radio jets, while others do not or what is the physical reason behind the distinction between radio-loud and radio-quite AGN or why QSOs and Seyfert galaxies appear very similar with only difference between them being their individual luminosity. Also the model could not present a clear connection between FR I and FR I galaxies nor clear our confusion about jet formation and propagation. In the end, though there are several questions which are not answered by Unification scheme, we can not nullify the importance of this model due to its simplicity and ability to justify orientation dependent AGN classification, which improves our understanding.

1.4 Emission Mechanisms in AGN

AGN emits in a wide range of frequencies ranging from radio to gamma-rays and their broad-band spectrum is due to combined contribution of different emission mechanisms. Much of this radiated energy differ from the conventional stellar-emission which is attributed to thermo-nuclear process and is simply represented by blackbody radiation. The emission mechanisms which dominate the AGN phenomena are called nonthermal (or nonstellar) emission. There are several types of nonthermal emission processes, but in this section we will discuss only those which are more relevant to AGNs and to the physical conditions in the local environment of a massive BH.

1.4.1 Thermal Emission

The temperature dependent radiation emitted by a thermally hot matter is called thermal radiation which is characterized by Blackbody emission and defined by Planck's Law. The main source of thermal radiation in AGNs is the accretion disk. For a standard geometrically thick and optically thin disc (Shakura & Sunyaev, 1973), the temperature profile of the disc at a radial distance r, can be written as,

$$T(r) = 6.3 \times 10^5 \left(\frac{\dot{M}}{\dot{M}_E}\right)^{1/4} M_8^{-1/4} \left(\frac{r}{R_S}\right)^{-3/4} K \tag{1.3}$$

Where, $\dot{M}$ and $\dot{M}_E$, represents the mass accretion rate and Eddington accretion rate of the central engine, respectively and M_8 signifies the mass of the central black hole in units of $10^8\ M_\odot$. It is generally seen that the temperature of the accretion disk in AGN vary between $\sim$ 4000 to 40,000 K. From the above equation we see that the disk temperature is a function of the radial distance and increases inwards as $T \propto r^{-3/4}$. As a result, the total emission of the disk is a superposition of black bodies consisting of rings of different radii with different temperatures, where each annulus radiates following Planck's law and the overall emission spectrum of the accretion disc is obtained by integrating the Planck's equation over the radius, r and

is given by

$$F(\nu) \propto \nu^{1/3} exp\left(- \frac{h\nu}{kT(r_{max})} \right) \tag{1.4}$$

Here, h, c, and k are Planck's constant, the speed of light, and the Boltzmann constant, respectively and r_{max} is the radius at which the dissipation energy per unit area is maximum (Krolik, 1999). The resulting spectrum due to thermal emission from the disk does not follow a Planck shape but instead shows a much broader energy distribution due to the superposition of all the Planck's peaks resulting from each annulus of the disk. The optical/UV emission of AGN, observed mainly as the Big Blue Bump (BBB), is attributed to thermal radiation from the accretion disc (e.g., Malkan & Sargent, 1982).

1.4.2 Bremsstrahlung (free-free) Radiation

The acceleration of charged particle in the presence of nuclear Coulomb field of another charge triggers a particular types of radiation, called *Bremsstrahlung* or *free-free radiation*. In other words, when an electron is deflected by the Coulomb fields of heavy charged atomic nuclei it can emit or absorb photon. In non-relativistic framework, a charge particle which is accelerated or decelerated will radiate due to law of conservation of energy. Usually, free-free radiation is an optically thin, thermal process, but in case of AGN, the spectral shape due to this process is not similar to that of a blackbody. Since it is formally a thermal process, it depends on the total volume of the particles involved. With increasing opacity, the radiation becomes more and more thermal (blackbody-like). The strength of blackbody emission in an optically thick medium depends on the surface area of the emitter, rather than the total volume. In AGN, Bremsstrahlung emission could originate in the hot, ionized gas which is supposed to exist in the nearby region of the SMBH.

1.4.3 Synchrotron Radiation

Synchrotron radiation is caused by acceleration of relativistic particles in the presence of magnetic fields. Particles move in a magnetic field following a helical path

in which they are continually accelerated by the Lorentz force. Synchrotron radiation is highly linearly polarized emission which give rise to continuum spectrum distributed about a critical frequency (ν_c). Beaming effects concentrate the radiation in the forward direction within a narrows emission cone of half-angle $\sim 1/\gamma$, where $\gamma = \frac{1}{\sqrt{1-\frac{v^2}{c^2}}}$, is the Lorentz factor of the particle. If the energy distribution of emitting electrons follows a power-law shape of the form $P(\nu) \propto \nu^{-\alpha}$, than the Synchrotron radiation from these particles will also give rise to a power law continuum. If the distribution of these electrons with energy ranging between E and $E + dE$, is represented by, $N(E)dE \propto E^{-p}$ then the spectral index of the resulting power-law radiation (α) is related to the electron distribution index (p) by $\alpha = (p-1)/2$ (Rybicki & Lightman, 1979).

The relativistic jets of AGN emit synchrotron radiation at radio to optical bands and sometimes even X-rays and γ-rays. This radiation occurs when the highly energetic particles (blob of plasma) travel through twisted magnetic fields fastened with the jet. The maximum synchrotron power is emitted at a critical frequency, ν_c which is given by,

$$\nu_c = \frac{3\gamma^2 eB}{4\pi m_e c} sin\phi \tag{1.5}$$

Here, e & m_e are charge and mass of electron, B is magnetic field (in Gauss) and ϕ is the angle between B and direction of particle motion.

The true power law spectrum emitted due to synchrotron mechanisms will be observed only when there is no absorption by the emitting region, or by the intervening matter either in the AGN host galaxy or in the other galaxy along the light path. It is observed that the radio spectrum emitted from the lobes and jet of AGN often shows power-law distribution but the radiation from compact regions has flat, inverted or complex spectra (Kembhavi & Narlikar, 1999). These deformations in the synchrotron spectrum can be caused by different absorption processes. In presence of magnetic field, the emitted photons can be absorbed by the emitting electrons itself (synchrotron self-absorption). It is believed that most of the non-thermal emission in AGN is caused by synchrotron radiation. The main observed

and expected synchrotron sources in AGNs are the extended radio sources, radio jet, compact jet and the BH magnetosphere.

1.4.4 Inverse Compton (IC) Emission

The scattering of electromagnetic radiation by charged particles, mainly electrons is described by the Compton scattering theory where the interacting photons loss energy and the electron gain energy and momentum. But the process may occur in the reverse direction where the low energy photons are up-scattered by highly energetic electrons. This process is known as inverse Compton scattering. The mean energy of photons after scattering is larger than the mean energy before scattering, by a factor of γ^2. In the rest frame of the electrons, the process will behave as Thomson scattering. The expression for the power emitted in IC process can be given by,

$$\overline{P} = \frac{4}{3}\,\sigma_T\; c\; \gamma^2\; \beta^2\; u_{\,rad} \tag{1.6}$$

Here, $\beta = v/c$, where v is the speed of electron and σ_T & u_{rad} represents Thomson cross section and energy density of the radiation field, respectively. The spectral shape of the resulting spectrum depends on the original shape of the seed photon spectrum, the electron temperature and the Compton depth of the source. The process can repeat itself, in the same source by multiple scattering of the emergent photons. If the initial photons have energy $h\nu_i$, this process may repeat until the point where the condition $h\nu_i \ll m_e c^2$ no longer holds and no further up scattering of photons is possible. In this process the photons will gain energy during successive scatterings and the final energy of emergent photons, $h\nu_f$ is given by,

$$h\nu_f \simeq h\nu_i\; exp\left[N\frac{4kT_e}{m_e c^2}\right] \tag{1.7}$$

where, T_e is the electron temperature and N is total number of scattering. The strength of this interaction between electrons and photons is given by the Compton y-parameter (y), which is the product of average fractional energy change and mean number of scattering (see Netzer, 2013, for more detail). For $y > 1$, the inverse Comptonization reaches unsaturated regime and when $y \gg 1$, the Comptonization

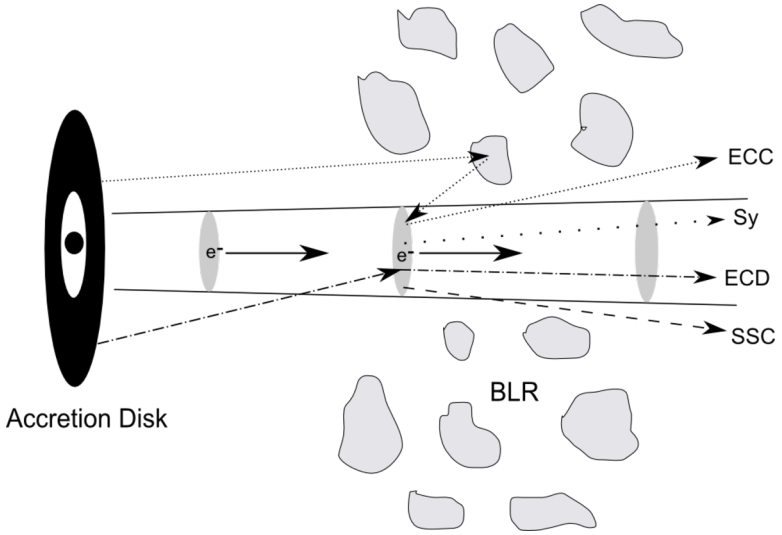

Figure 1.6: Sketch of the geometry and corresponding emission processes taking place in immediate environment of blazars (leptonic jet model) Different components are shown with name. Graphic: http://www.phy. ohiou.edu/ mboett/agn.html.

becomes saturated, where the average photon energy become equivalent to the thermal energy of electrons. These states are highly dependent of the emitting environment. In AGN the process is expected to be unsaturated and leads to a power-law spectrum over a limited energy range. High-energy emissions mainly in X-ray/γ-ray bands are produced due to inverse Compton scattering of low seed photons in AGNs.

1.4.5 Importance of AGN Study

Study of AGN is one of the most dynamic areas of modern astronomy. Due to their extreme and exotic properties like presence of SMBH powered by accretion of matter, extremely high rates of energy generation in the entire electromagnetic spectrum, jets of relativistic particles or their peculiar surrounding environment, they are the special laboratories for extreme physics. Understanding these phenomenon requires a wide range of knowledge in many different areas such as, the physics of dust and ionized gas, astronomical spectroscopy, BH physics, star formation and cosmological evolution of galaxies, etc.. Due to their extreme luminousity AGNs are observed up to a high redshift ($z > 6$), which makes them principal probes of

the early universe on large scales and thus their study broadens our understanding of the formation & evolution of the universe as a whole. By investigating the absorption line in AGN spectra, the intergalactic medium and the gravitational lensing effect can also be studied. As a consequence of the SMBH, the gravitational field is extreme around it, which allows the investigation of General Relativity in an extreme environment; for example, some AGN show very broad and skewed iron line profiles in their X-ray spectra indicating that they originate close to a spinning BH.

1.5 Blazars

This thesis is mainly focused on the study of blazars, which are observationally the most powerful and extreme emitter in the entire electromagnetic (EM) spectrum due to the close alignment of their relativistic jets toward us and belong to a small subclass of radio-loud AGN that includes BL Lac objects (BLLs) and flat spectrum radio quasars (FSRQs). They show rapid flux variability on timescales of hours to years in all wavelengths, have high and variable polarization and their emission is predominantly non-thermal. Their radio structures are dominated by compact cores, with some of their radio components showing superluminal motion due to Doppler boosting (Aller et al., 1992; Andruchow et al., 2005). The interesting fact about blazars is that they possess relativistic jets of highly collimated radiation and plasma emanating from the central region viewed at a small ($\lesssim 10^{\circ}$) angle to the observer's line of sight (Urry & Padovani, 1995) which drives almost all the observed features in blazars. The optical spectra of BL Lacs show featureless continua whereas spectra of FSRQs have prominent emission lines. The absence of emission lines in the spectra of BL Lacs often makes the quantification of the redshift difficult or impossible. The degree of polarization and the ratio of X-ray to radio flux in the two classes of blazars also differ. However, in some blazars these differences are very small or not clear and it has been also observed that some of them contain properties of both classes. The main observed characteristics of blazars are discussed in detail in the following subsections.

1.5.1 Variability

Variability of blazars is one of the widely used approach by the community to understand the different physical mechanisms involved in the vicinity of supermassive black hole (SMBH). The multi-bands flux of blazars varies on diverse timescales and depending on this timescale their variability is categorized in three different types; Intraday variability (IDV), short term variability (STV) and long term variability (LTV) where variation occurs in few minutes to one day, few days to one month and few months upto several years, respectively (Gupta et al., 2004). Out of all these timescales, the most interesting one is to study blazar in the intraday or intranight timescale. The variability timescales in blazars are different for different wavebands. Evidence for flux variation even within few minutes was observed in previous studies for higher energy bands (in X-ray & gamma-ray) (Aharonian et al., 2007; Böttcher et al., 2003). Since the higher energy photons are emitted from regions closer to the BH, IDV study in higher energy bands can provide information about the immediate environment of the central engine. The shortest timescale of variability can constraint the upper limit to the size of the emitting regions ($R \leq c\Delta t$) and can also be used to calculate the BH mass. Moreover, correlated variability study (time lags) between different wave-bands have been used to connect different radiation processes taking place in the source.

In the case of blazars it is widely believed that variability originates mainly from the enhanced emission in a small region within the relativistic jets (Begelman et al., 2008). It has already been assumed that IDV is an intrinsic phenomenon in AGNs (Wagner & Witzel, 1995). This type of variability may occurs due to different physical processes regarding different state of the source. If the source is in low or quiescent state, the observed IDV may originate through mechanisms which involve the accretion disc emission. In this scenario the IDV could occur as result of the pulsation of gravitational modes of the gaseous disc or/and it may arise due to hot spots on the accretion disc, which is orbiting the BH. However, in high state the picture is totally different, where we basically see the jet emission, hence any IDV detected during this period are the result of fluctuations in the jet. The widely accepted reason behind these variations is the shock propagation within the

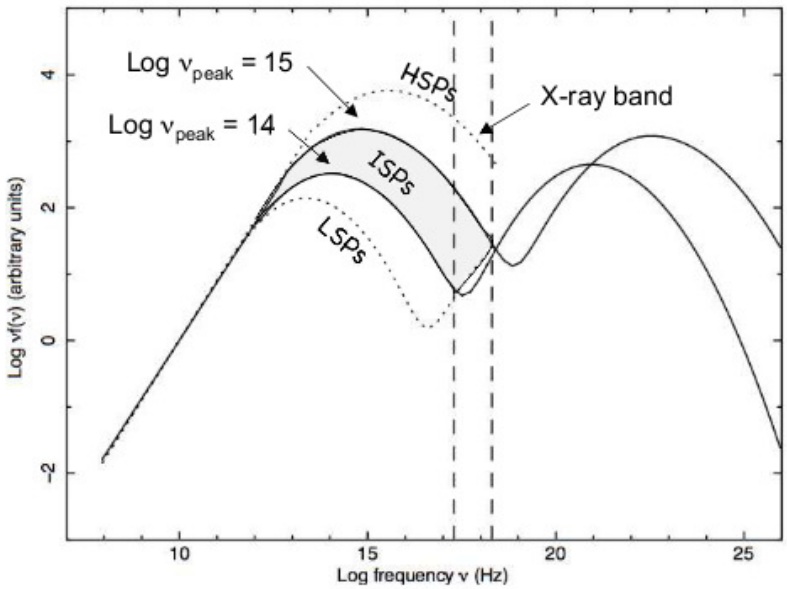

Figure 1.7: The broadband SED of blazars. Classification based on the peak frequency of the synchrotron component (ν_{peak}) in their SED is shown in the plot. Figure courtesy : Raino' et al. (2009)

jet (e.g. Gupta et al., 2012, and references therein). For example enhancement in emission could be triggered by dissipation inside the out-coming blob of material at the jet base or it may result from the instabilities within the jet itself.

1.5.2 Overall Blazar Continuum (SED)

The Spectral energy distribution (SED, νF_ν vs. ν representation) of blazars display two distinct broad humps, typically characterized by their peak energies. Across the entire SEDs of blazars, the emission is dominated by nonthermal processes such as synchrotron emission and inverse Compton scattering (see section 1.4). According to the current model, the low-energy peak is mainly due to the contribution of synchrotron emission from jet components, which lies in the range of infrared to hard X-ray regime and the high-energy component is likely due to one or more components related to IC emission which lies in the γ-ray bands. Depending on the peak frequency of the first hump blazars can also be classified as high synchrotron peaked (HSPs), intermediate synchrotron peaked (ISPs) and low syn-

chrotron peaked (LSPs) blazars and their synchrotron peak frequency, ν_s lies in the ranges, $\nu_s \leq 10^{14}$ Hz (far-IR or IR band), $10^{14} < \nu_s \leq 10^{15}$ and $\nu_s \geq 10^{15}$ (UV or higher energies), respectively (Abdo et al., 2010c). Fig. 1.7 shows SED-based classification of blazars. Generally, FSRQs belong to the LSP class and BL Lacs belong to either ISPs or HSPs. The high energy peak (γ-ray) of the SED show significant curvature, which is found to be convex for LSPs whereas very flat or even concave for HSPs (Giommi et al., 2009). As synchrotron peak of LSPs lies in the far-IR or IR band, their X-ray component of the SED appears flat, which is further flattened by the rising part of the inverse Compton component. At these relatively low energies the inverse Compton scattering occurs in the Thomson regime (Abdo et al., 2010c). In ISP blazars, the X-ray emission is due to combined contribution from the tail of the synchrotron emission and the rise of the IC component, while synchrotron peak for HSPs occurs in UV or X-ray bands, whereas synchrotron emission dominates the observed flux in the X-ray band and the inverse Compton scattering occurs in the Klein Nishina regime (Abdo et al., 2010c).

A simple homogeneous, one-zone, SSC model cannot explain the broad band SED of FSRQs and low energy peaked (LBL) BL Lacs, but more complex models involving EC radiation or multiple SSC components are required to describe the overall SED (Abdo et al., 2010c; Giommi et al., 2008). On the other hand, High energy BL Lacs (HBLs) have been well described by pure synchrotron self-Compton models. It has often been found that the blazar sequence (LSP→ISP→HSP) show a decreasing contribution of EC radiation (Ghisellini et al., 1998).

1.5.3 Different Models to Support Blazar Emissions

In order to replicate the multi-wavelength SED pattern observed in blazars, different emission models has been used by the community. Due to close alignment of the relativistic jet towards us, the emission coming from blazar is jet dominated and thus any signatures of accretion disk if present, is swamped out by the Doppler boosted jet emission. A general description of the primary blazar emission models are discussed below:

1.5.3.1 Leptonic Model

In this model, the high energy emission is believed to originate from Compton upscattering of low energy seed photons upto X-ray and γ-ray photons by the relativistic electrons in the jet. In a compact synchrotron source like blazars, the emitted photons can be upscattered by the same relativistic electrons which produce the synchrotron radiation. The radiation emerging through this process in refereed as *synchrotron self-Compton (SSC)* emission (Ghisellini & Maraschi, 1989; Marscher & Gear, 1985). The resulting spectrum will have a spectral index similar to that of the synchrotron source. This model is controlled by the parameters like, size of the emitting region, the bulk Lorentz factor of the emitting particles, strength of the magnetic field and the energy distribution of the electrons that are injected into the jet. The peak of the IC emission (ν_{ssc}) and the synchrotron emission (ν_{syn}) in SSC model is closely related by,

$$\nu_{ssc} \approx \frac{4}{3}\,\gamma^2 \nu_{syn} \tag{1.8}$$

The simplest form of SSC model uses a single, spherical emission zone moving in the jet, while multiple-zone SSC model is also in use to describe the blazar emission. The SSC is the dominating high-energy photons producing process in the jets. If this mechanism is working behind the scene, a correlation between the X-ray and γ-ray bands will be observed. Other sources of soft photons exist as well, which could be upscattered by the jet plasma. The possible sources of these external seed photons are the accretion disk emission or the reprocessed optical–UV emission by the BLR or photons could come from the dusty torus (Błażejowski et al., 2000) or synchrotron emission from other (faster/slower moving) regions of the jet itself (Ghisellini & Tavecchio, 2008). In this case the process is called as External Compton (EC) emission (or EC model) (e.g., Dermer & Schlickeiser, 1993; Sikora et al., 1994).

Leptonic models are very successful in explaining the blazar SEDs and also in some cases the blazar variability. In a magnetic field, B $\sim$ 1 Gauss, the radiative cooling timescales of synchrotron electrons are of the order of hours–1 d at optical bands and is $\leq$ 1 hr in X-rays and hence able to interpret the observed intraday

variability (Boettcher, 2012).

1.5.3.2 Hadronic Model

In an alternative scenario, if a significant fraction of jet power is used to accelerate the relativistic protons in presence of strongly magnetized environment, protons may directly emit synchrotron emission. These relativistic protons also may decay into neutral primary pions (π^0) which eventually decay into γ-ray photons and other hadrons and if the protons decay into charged pions ($\pi^{\pm}$), then the following emission of muons ($\mu^{\pm}$) and electron/positron (e^-/e^+) will generate synchrotron photons when the emitting region is opaque for $\gamma\gamma$ absorption (e.g. Boettcher, 2012; Mannheim & Biermann, 1992, and reference therein).

To accelerate the protons to the required ultra-relativistic speed ($E_p^{max} \geq 10^{19}$ eV), a strong magnetic field of several Gauss is needed. In presence of such high magnetic field a self-consistent synchrotron cascade will be established by the synchrotron radiation of the primary protons and of the secondary muons and mesons. The "π^0-cascades" and "$\pi^{\pm}-$cascades" generate featureless γ-ray spectra while the "p$-$cascades" and "$\mu^{\pm}-$cascades" produces γ-ray spectra with two components (Boettcher, 2012; Mücke et al., 2003).

1.5.3.3 Shock$-$in$-$Jet Models

Shock$-$in$-$jet models (Marscher & Gear, 1985), generally used to explain radio emission of extragalactic jet was first proposed to explain the high-energy spectra of blazars by Spada et al. (2001). Shock fronts in the jet are thought to be set up due to intermitten ejection of shells of relativistic plasma at varying speeds at the jet base (Joshi & Böttcher, 2011; Mimica et al., 2004), which travel down the jet. Multiple shocks propagating down the jet can lead to shock-shock interactions (Marscher, 1996), which will cause compression of the intervening plasma in the jet and also increases the magnetic field strength (B), and particle velocity. In this process, successive shock-crossing accelerate the particles upto a very high-energy before they leave the acceleration region (diffusive shock acceleration Schwadron et al., 2008) and due to internal scattering, the velocity distribution of the plasma

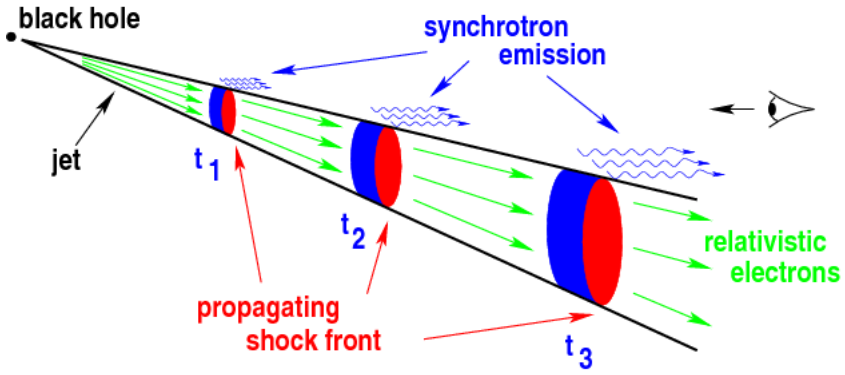

Figure 1.8: A schematic diagram of the standard shock-in-jet model showing a propagating shock wave in a relativistic jet. Image courtesy : Marscher & Gear (1985)

becomes isotropic with respect to the flow. Consequently the synchrotron emission from the jet will be highly amplified due to increase in magnetic field strength, internal energy or density behind a shock front or it could be due to diffusive shock acceleration. The frequency of the emitted photons in this process depends on energy of the accelerated particles.

Shock-shock interactions is one of the possible mechanisms that could accelerate particles upto ultarelativistic speed which result into broadband (multi-frequency) flares. The interaction between shocks can occur when a moving shock wave collide with a stationary shock (which are common characteristic of compact jets) (Fromm et al., 2013; Jorstad et al., 2001). In shock induced multi-frequency flare, the high energy photons (X-rays & γ-rays) emerge first from a smaller region closer to the jet base, while the lower energy emission occurs in regions with higher radius and distance from the core (Marscher, 1996). Shocks propagation and their corresponding emission mechanisms is depicted in the Fig. 1.8.

1.6 Motivation and Structure of this Thesis

The current state of understanding of AGN and blazars are described briefly in the previous sections. It is clear from the above discussions that for better understanding of different emission mechanisms and to obtain a clear picture of the local environment of blazars, multi-wavelength approach is very important. The motivation of this thesis is to explore different physical processes involved with blazars in multi-frequency domain through temporal and spectral study, and also to get better understanding of diverse variability properties observed in these objects. To achieve our aim we have studied a sample of blazars with observations made by *XMM-Newton* X-ray observatory. The study of the fairly big enough sample with highly sensitive data will lead to a better understanding of different X-ray emission mechanisms and their twisted connection with other bands emission in different activity states of blazars.

In persuasion of the motivations discussed above, the research work that has been done for this thesis is structured as below:

Chapter 2 : An overview of the satellite, X-ray multi mirror mission, XMM−Newton, the data analysis techniques for different science instruments used for this study are given in this chapter. A comparison of XMM−Newton with other X-ray missions has also been discussed.

Chapter 3 : This chapter is based on the variability study of the first discovered FSRQ 3C 373 in multi-frequency domain on diverse timescales. The correlation study between optical, UV and X-ray bands are also carried out to get an insight of different emitting zones involved within the nuclear region of the blazar.

Chapter 4 : The relation between SED synchrotron peak of blazars and its intraday variability in the X-ray domain is studied for a sample of 12 sources. From this study we come up with the conclusion that LSPs are less variable in X-rays but highly variable in optical bands on IDV timescales. An explanation for the results is given in terms of relative positions of these bands w.r.t. the synchrotron peak

frequency in the multi-band SED.

Chapter 5 : This chapter covers the study of spectral evolution of the borderline object, 3C 273 in the energy range 2.5–10 keV in X-ray regime during 2000-2015. The first time observed "harder-when-brighter trend" in long-term multi-epoch observations can be linked to lower accretion rate of the central SMBH. From the simultaneous study in optical/UV & X-ray bands, we ensure that the X-ray emission during this period was governed by inverse Compton scattering of optical/UV photons from a hot corona present above the disk.

Chapter 6 : All the studies that have been done in this thesis are briefly discussed in this chapter, highlighting only the major conclusions. A short discussion on our current work and future research plan is also presented.

Chapter 2

Observations & Data Analysis

The research work embodied in this thesis is the outcome of observations carried out by the X-ray Multi-Mirror Mission, *XMM-Newton*. To study the temporal variability on diverse timescales and their corresponding emission mechanisms as well the spectral evolution of blazars, we use multi-frequency data in optical, UV and X-ray regime. In this chapter we mainly discuss the scientific instruments on board the X-ray observatory and their characteristics, blazar observations by the satellite and archival data, the data processing methods for different instruments and last but not the least why *XMM-Newton* is preferred from rest of the X-ray satellites for blazar study.

2.1 XMM-Newton Satellite

XMM-Newton is one of the currently active X-ray mission which is exploring the nearby and distant universe through its multi-wavelength eyes/windows. The major difficulty in X-ray observations arises due to the Earth's atmosphere, which is opaque to X-rays. As a result X-ray photons can not be detected from ground based telescopes. Hence, to study celestial X-ray sources we need to place a telescope above the atmosphere i.e. in space. In this context different X-ray telescopes with different specifications have been projected into the space since *Uhuru*, the first earth-orbiting satellite dedicated entirely to X-ray astronomy launched in 1970. The *XMM-Newton* observatory was launched in December 1999 by European Space

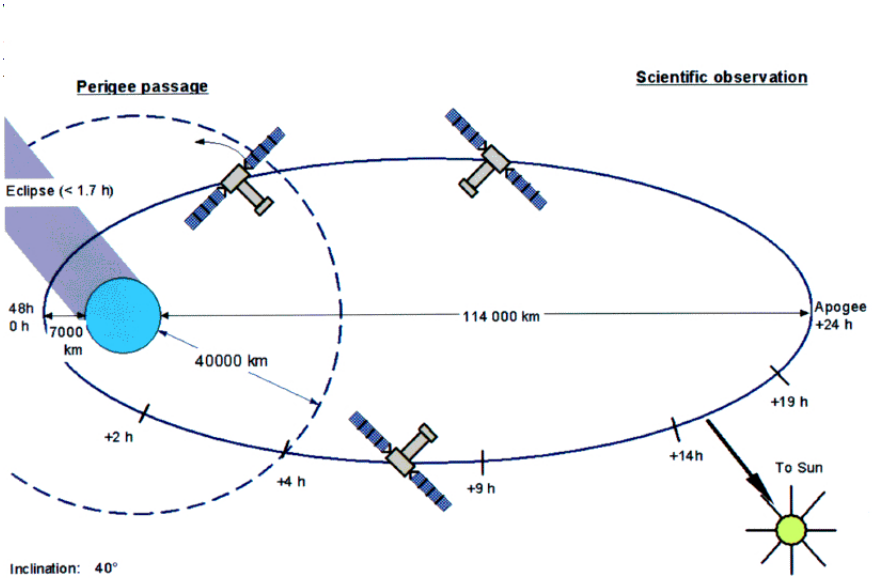

Figure 2.1: Orbit of *XMM-Newton* observatory. The high eccentric elliptical orbit of the satellite changes with time. Image taken from https://heasarc.gsfc.nasa.gov/docs/xmm.

Agency (ESA). The satellite was named in honor of Sir Isaac Newton. It carries four highly effective telescopes; three observe in X-ray bands and one observes in optical/UV bands. The ability to observe objects simultaneously in different electromagnetic bands is an outstanding advantage of the satellite. The operation of the spacecraft is jointly controlled by the European Space Operations Centre (ESOC, Darmstadt Germany) and the ground stations at Perth, Australia; Kourou, French Guiana; Villafranca, Spain; and Santiago, Chile. All the science operations of the satellite are controlled by *XMM-Newton* Science Operations Centre (SOC) which is located at the European Space Astronomy Centre (ESAC) in Spain, Europe. The length of the satellite is 10 m and its width is 16 m covering the huge solar arrays. The satellite mass is 3.8 tonnes.

The satellite orbit is highly elliptical with a launching perigee $\sim$ 20,000 km and an apogee about 120,000 km and it rotates around the earth making an inclined angle with an orbital period of 48 hrs. During each orbit the satellite passes through the Earth's radiation belt which can affect the detectors and hence the observation sig-

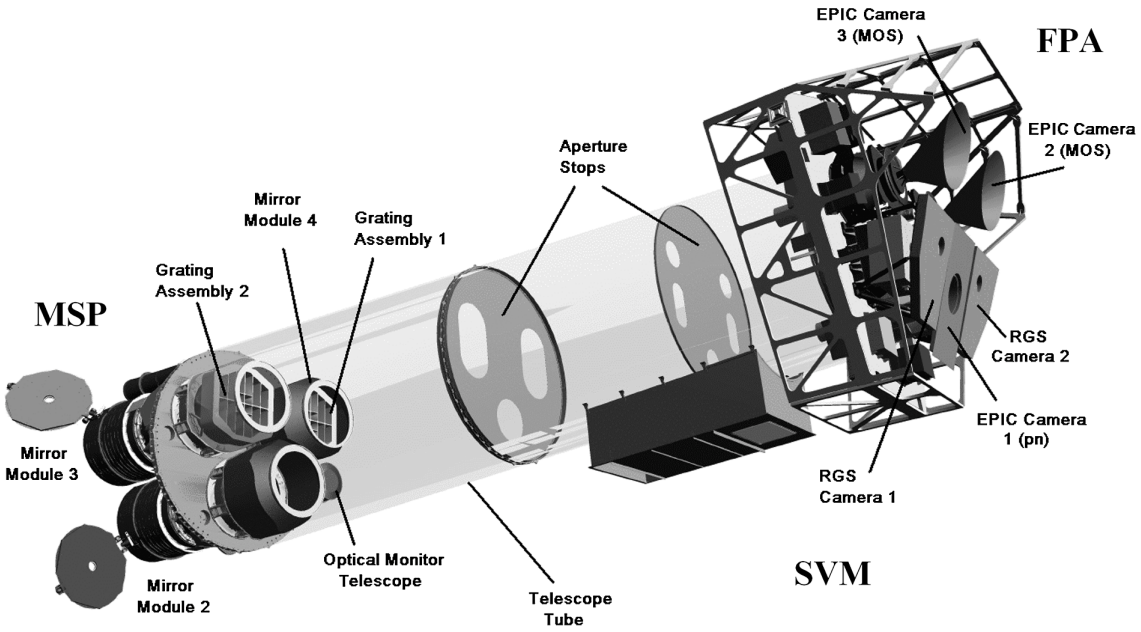

Figure 2.2: Schematic diagram of the *XMM-Newton* spacecraft subsystems. Image taken from (Lumb et al., 2012).

nificantly, therefore during this period all the science instruments are switched off. Thus, science observations are conducted only when the satellite elevation is above 46,000 km which provides around 138 ks of continuous target observation. Apart from these radiation backgrounds, the observation may also affected by solar emission. So, preventing detector from damage all payload instruments are switched off during major solar flares. The sketch of the satellite orbit is shown in the Fig. 2.1. The orbit keep changing with time.

The lifetime of the mission was originally fixed for a 10 years. But now due to high scientific demand and excellent performance of the spacecraft and instruments, its life time has been extended. Considering the fuel (hydrazine) limitation on board the mission could last up to 2019 (Kirsch et al., 2014).

2.1.1 Components of the Spacecraft

The different subsystems of the spacecraft are shown in the Fig. 2.2 and each are discussed below:

2.1.1.1 Focal Plane Assembly (FPA)

The FPA contains the focal Plane platform which carries one EPIC-pn and two EPIC-mos imaging detectors, two reflection grating spectrometer (RGS) readout cameras along with the data handling units. The assembly also contains the power distribution units for the cameras and radiators attached with the EPIC cameras and RGS units to cool their CCD detectors.

2.1.1.2 The Mirror Support Platform (MSP)

The mirror support platform carries the three X-ray mirror assemblies, the optical monitor (OM) and two star trackers to track targets.

2.1.1.3 Telescope Tube

The focal plane assembly and the mirror support platform are connected with a 6.8 m long carbon fibre telescope tube. The main function of the tube is to maintain the relative position between the two assemblies.

2.1.1.4 The Service Modules (SVM)

The service modules is the main resource centre of the satellite which carries the spacecraft subsystems. It also carries two solar-array wings, the Telescope Sun Shield (TSS) along with two S-band antennae.

2.1.2 X-ray Telescopes

Conventional mirror designs used in optical telescopes can not be used to focus X-rays. Since the energy of X-ray photon is very high, in near normal incidence it is either transmitted or absorbed by the mirror material. So, a special kind of telescope is used in X-ray observations, called Wolter telescope which works on grazing incidence optics. Two types of mirrors are used in this telescope to reflect the X-ray; a primary parabolic mirror and a secondary hyperbolic mirror. *XMM-Newton* X-ray telescopes consist of Wolter I grazing-incidence mirrors with a telescopes focal length of 7.5 m. A set of 58 such mirrors are designed in a coaxial and co-focal configuration (Jansen et al., 2001). This design is particularly adopted to achieve

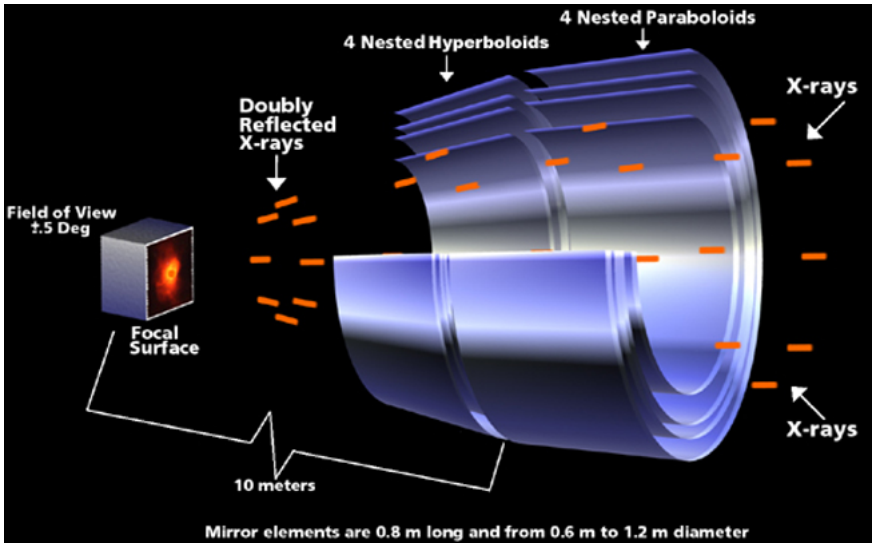

Figure 2.3: *XMM-Newton* mirror module with coaxial parabolic and hyperbolic mirrors. Image taken from ESA.

highest effective area in a wide range of energies. The grazing angle used in the mirror module for focusing of X-ray light is $30'$ and the largest mirrors have a diameter of 70 cm. The X-ray mirror module is shown in Fig. 2.3. Each of the X-ray telescope also contains baffles for suppression of visible and X-ray stray-light and a deflector for diverting soft electrons.

Two of the X-ray telescopes with MOS camera have grating assemblies in their light paths which diffract about 50% of incoming light towards the secondary focus. The light path of X-ray telescopes with pn and MOS detectors are shown in Fig. 2.4.

2.1.3 Main Scientific Instruments

2.1.3.1 European Photon Imaging Camera (EPIC)

XMM-Newton carries two types of CCD cameras; EPIC MOS (Metal Oxide Semi-conductor) and EPIC pn, attached with the X-ray telescopes. Two of the X-ray telescopes are connected with MOS CCD arrays and one is connected with PN CCD arrays. Each type of cameras have different properties and functions such as,

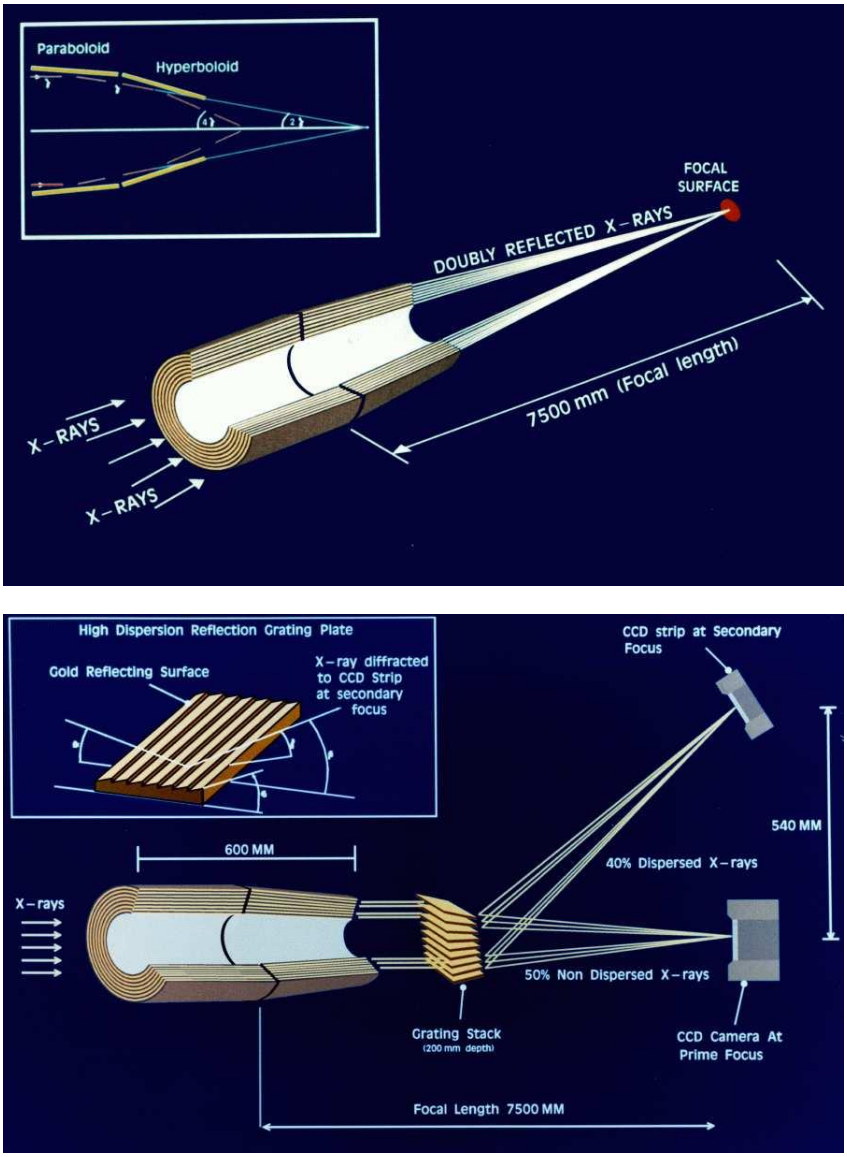

Figure 2.4: Upper panel: Light path in the X-ray telescope with only an EPIC-pn camera in its primary focus. Lower panel: Light path in the two X-ray telescopes with EPIC-MOS cameras in which the reflection grating assemblies are placed in the middle of light path. Image taken from ESA.

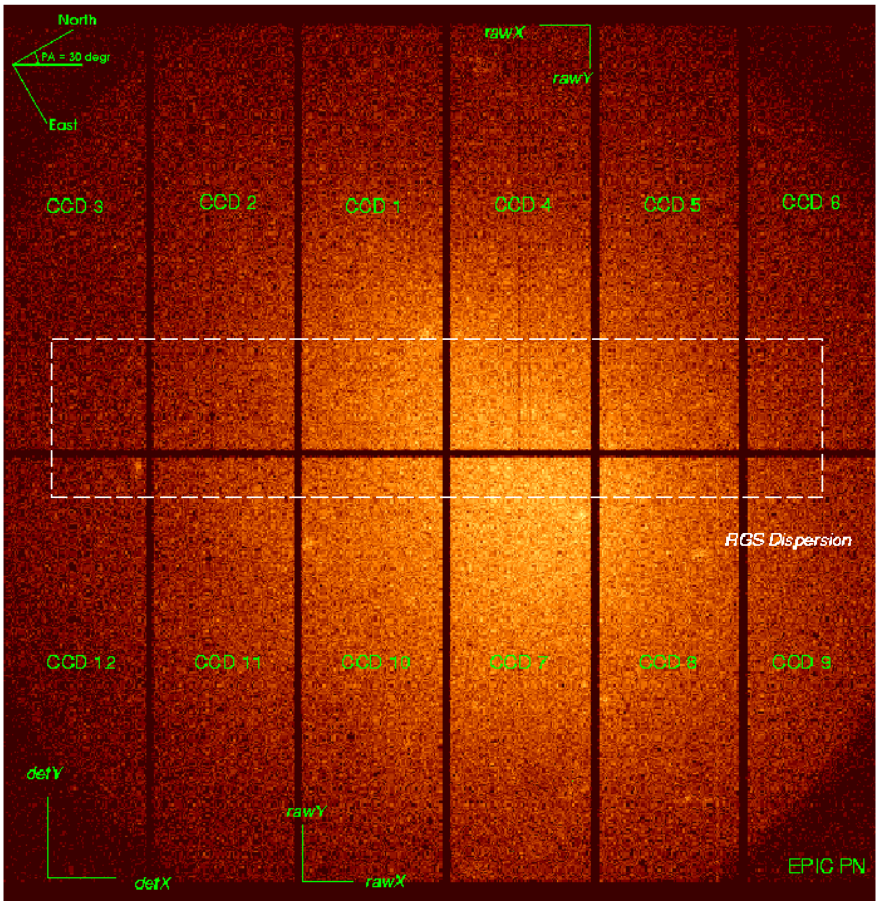

Figure 2.5: The geometry of the EPIC pn CCD array. The orientation of the detector coordinates [DETX/DETY] and CCD specific coordinates [RAWX/RAWY] are shown in the above diagram. Assuming a position angle of 30° the orientation of the celestial coordinates [North/East] is also shown in the figure. Image taken from SAS.

different orientation of CCD chips array with different readout times, their detector quantum efficiencies are different. These cameras can provide highly sensitive imaging observations and X-ray spectroscopy with moderate spectral resolution, $E/\Delta E$ nearly in the range 20–50. These EPIC cameras can detect X-ray photons in the energy range 0.15 to 15 keV (Strüder et al., 2001; Turner et al., 2001). The two types of detectors are discussed below:

EPIC−pn camera

This type of camera can provide imaging with very high time resolution (down to 0.03 ms in the timing mode). The pn detector contains 12 pn type CCD chips arranged in a linear fashion as shown in Fig. 2.5. These CCDs are back-illuminated and operate in photon counting mode. The pn camera is more sensitive for hard X-ray photons and detect the high energy part of the spectrum with higher energy resolution. The reason behind this is the high thickness (300 micron) of silicon of the double-sided processed silicon detector.

EPIC−MOS camera

Each MOS detectors compose of metal oxide semi-conductor (MOS) CCDs and contain an array of 7 CCD chips arranged on a curvy plane. The offset between the CCDs are introduced to make an equidistant plane from the focal plane of the X-ray telescopes. The layout of MOS CCDs are shown in Fig. 2.6. The MOS cameras are oriented perpendicular to each other. CCD3 and CCD6 of MOS1 camera is not in working condition due to impact of micrometeorite. The RGS units are also attached in the light path of the X-ray telescopes equipped with MOS detectors. As a result only about half of the reflected X-ray light incident on the MOS cameras. The MOS CCDs are front-illuminated and as pn CCDs they also operate in photon counting mode. Due to the small depth of sensitive silicon (40-micron) in the detectors, MOS cameras are more sensitive for soft X-ray photons than hard X-ray photons (e.g. Turner et al., 2001).

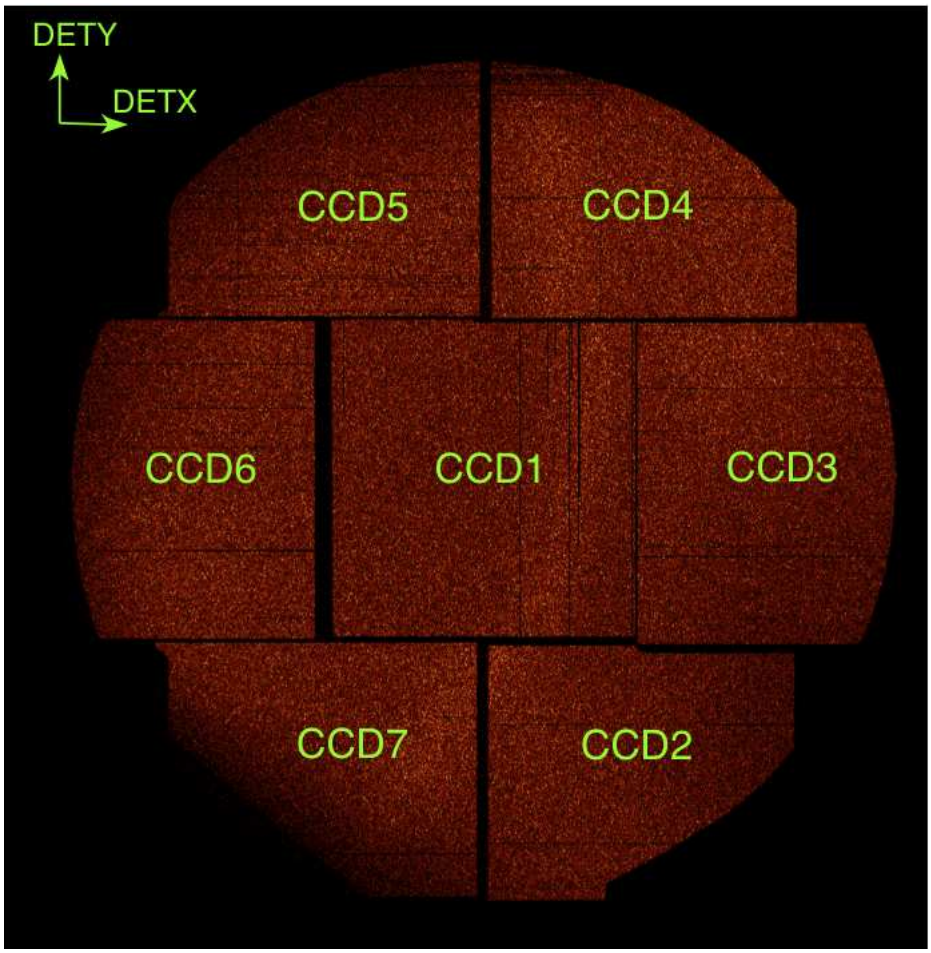

Figure 2.6: The geometry of the EPIC MOS CCD array. The image in detector coordinates [DETX and DETY] are shown in the figure. CCD3 and CCD6 of MOS1 camera are not in working condition and switched off for scientific observations. Image taken from *XMM-Newton* user handbook

EPIC−operating modes

The EPIC cameras can be operated in different science modes. The pn camera can operates in Full Frame and Extended Full Frame mode where all the CCDs are read out. It can also operate in Partial Window mode which includes, the Large Window mode where only half of the area of the CCD array is used and the Small Window mode where only CCD4 (Fig. 2.5) is used to collect data. In case of MOS cameras, the partial Window mode use only the central CCD for data acquisition. The MOS and pn cameras can also operate in Timing mode collecting one-dimensional image. An additional advantage of EPIC pn camera is that it can also operate in Burst mode which can provide very high resolution time series data.

EPIC−optical blocking filters

The CCDs used in EPIC cameras are also sensitive to low frequency photons like IR, optical and UV. So, these photons can contaminate the X-ray signal which may give spurious results. This problem is called optical loading. To overcome the problem a set of three aluminised optical blocking filters are included with each EPIC camera. Though introducing these filters reduce the detector effective area in the lower energy range, it is necessary to use them when the target is optically bright or if there is a bright optical source within 2 arcmin of the target in the field of view of X-ray telescopes. These filters are named as thick, medium and thin depending on their efficiency to block optical photons.

2.1.3.2 Optical Monitor (OM)

The exceptional advantage of *XMM-Newton* satellite is the optical/UV monitor coalinged with the X-ray telescopes which can observe a target, simultaneously with the X-ray telescopes. It is a 30 cm Ritchey-Chretien telescope with focal ratio f/12.7 and focal length of 3.8 m. A major plus point of this optical telescope is that it operates in absence of atmospheric extinction, diffraction and background

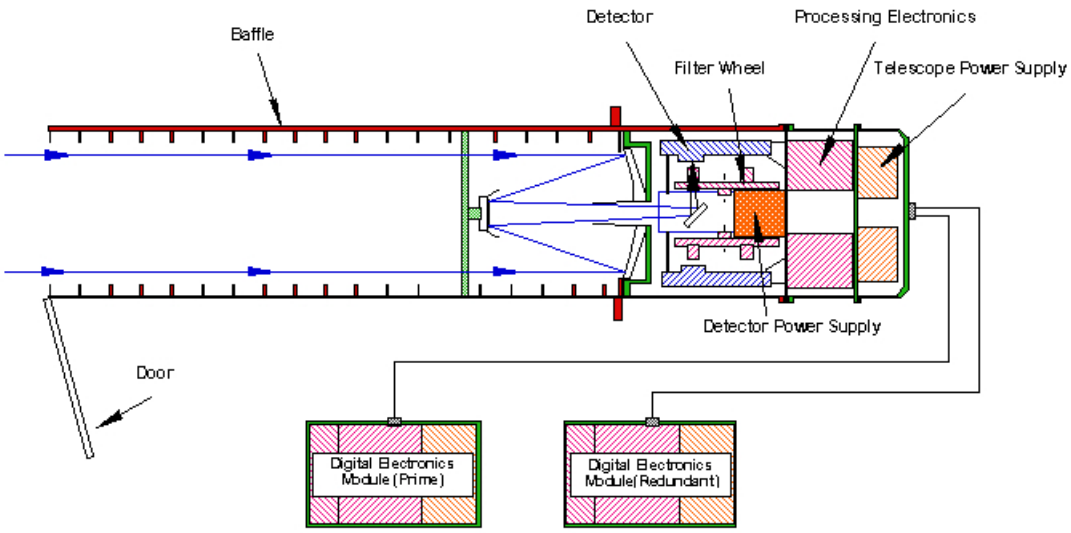

Figure 2.7: Schematic diagram of the optical monitor. Image taken from ESA

which makes it a very powerful optical instrument as compared to ground based telescopes. It operates in the wavelength range 170–650 nm and observe the central region of the X-ray field of view covering 17 arc minute area. The main purposes of this OM are to provide accuracy in tracking objects and to observe the target simultaneously in optical/UV bands with the X-ray telescopes.

The schematic diagram of the optical monitor is shown in Fig. 2.7. The primary mirror is kept at an inclined angle of 45° to the incident light which reflects the light onto a secondary mirror. The secondary mirror again reflects back the light to a inclined mirror from where it directly goes to one of two detector assemblies. A filter wheel is attached in front of the detector which contains different UV/optical filters, one white filter, two grisms (optical and UV) and one magnifier. The optical *U, B, V*, filters collect data in the wavelength ranges 300–390 nm, 390–490 nm, 510–580 nm, respectively and the ultraviolet *UVW2, UVM2, UVW1* filters collect data in the wavelength ranges 180–225 nm, 205–245 nm, and 245–320 nm, respectively (for more details see Mason et al. (2001)). With optical monitor we can obtain high time-resolution photometry with timing resolution = 0.5 s (in the Fast Mode) and low-resolution (Resolving power $\sim$ 180) optical/UV grism spectra.

The OM detectors are photon-counting instruments consist of micro-channel plate (MCP) intensified CCD (MICs). Each CCD has 384×288 pixels, 256×256 of which are usable for science observations. There are two operating modes of OM; imaging mode and fast photometry mode. Under suitable conditions both operating mode can be used simultaneously. The OM is suitable for observing faint objects up to a sensitivity limit of 20.7 mag (5-σ detection of an A0 star in optical B band). It can not be used to observe extremely bright object which cause damage of the high sensitivity detectors. The brightness limit of the detectors (i.e., highest magnitude of a star, which can be observed with the OM) is $m_V \leq$ ca. 7.4 mag.

2.1.3.3 Reflection Grating Spectrometer (RGS)

There are two reflection grating spectrometers on board *XMM-Newton* which operate in the energy range 0.33–2.5 keV to provide high resolution X-ray spectroscopy with resolution from 100 to 500 FWHM. Both RGSs cover the same FoV of the X-ray telescopes. The RGS units consist of two components; Reflection Grating Assemblies (RGAs) and RGS Focal Cameras (RFCs) and are attached to the X-ray telescopes with EPIC-MOS detectors. The RGAs of the RGS units are mounted at the primary focus (grazing incidence) of the X-ray mirror module which diffract about half of the total X-ray light focused by the mirrors. Each grating plate in the RGAs contains 645.6 tightly controlled groove lines (mm^{-1}) on it. The both RGA units consist of 182 such identical grating plates each. For more details see Brinkman et al. (1998); den Herder et al. (2001).

The RGS focal plane camera integrates the dispersed spectrum. It contain 9 back illuminated MOS CCD chips mounted in a row along the direction of diffracted light. These CCDs work in single photon counting mode and efficiently detect the dispersed X-ray photons. These CCDs are kept at a temperature of -80° C for better performance and lesser dark current. Each CCD chips contains 1024×768 pixels. The X-ray diffracted through the grating plates are dispersed on the detector at different position depending on the wavelength.

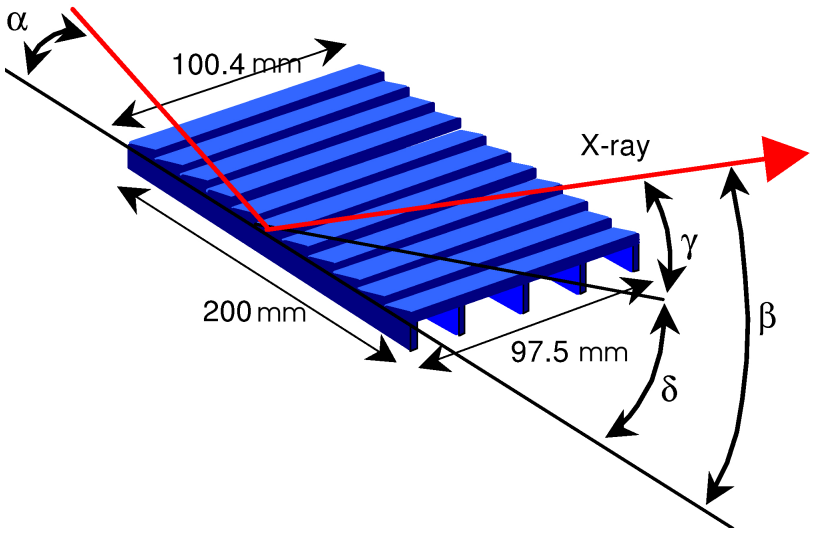

Figure 2.8: Schematic diagram for diffraction geometry of RGS. Image taken from https://heasarc.gsfc.nasa.govESA.

The diffraction geometry of RGS is shown in Fig. 2.8. Light incident on the grating plates with grating spacing d, at an angle α and reflected at an angle β following the dispersion equation

$$cos\beta = cos\alpha + m\lambda/d \tag{2.1}$$

Where m is spectral order and λ is the wavelength of incident light.

2.2 Data Reduction and Analysis

2.2.1 *XMM-Newton* Science Archive

XMM-Newton Science Archive (XSA) contains all the observations that have ever been made by the satellite. It also contains different source catalogues derived through its lifetime. Theses data are made publicly accessible at *XMM-Newton*

Science Operations Centre maintained by ESA and at The *XMM-Newton* Guest Observer Facility (HEASARC) maintained by NASA. There are two data formats available in the archive; Observation Data Files (ODF) and Pipeline Processing System (PPS) products. The ODF contains un-calibrated raw data files mostly in FITS format for all the available instruments for that observation ID. On the other hand the PPS file contains calibrated data files including cleaned event list for both EPIC-pn and EPIC-MOS cameras, source list, light curves, spectra, etc which can be immediately used. It also contains the quality reports of the PPS outcomes and graphical representation of different science product[1]. The observations of a target can be divided into several exposures tagged with separate observation IDs having different exposure time (data lengths). These observations can also have exposures made by different instruments in different operating mode (see 2.1.3.1)

2.2.2 Science Analysis System (SAS)

SAS[2] is the highly sophisticated software developed by Survey Science Centre (SSC) and Science Operation Centre (SOC). The software is used to reduce, extract and analyze the data taken from *XMM-Newton* observatory. There are several scripts, tasks and libraries inside the software, which are used in executing different steps of the data reduction process. Up to date version of SAS is released periodically. The software is improvised with each release by developing new software and fixing bugs. SAS is not required for science analysis of calibrated scientific products, while it is necessary to create scientific products according to ones own data selection criteria, to check up to what extent the source is affected by pile-up, to generate Good Time Interval (GTI) files, to make barycentric corrections, etc. SAS can not be use for temporal and spectral analysis.

2.2.3 X-ray Light Curve Generation

Though the calibrated events list file can be directly used from the PPS product directory, it is useful to reprocess the ODF directory data to achieve the benefit of

[1] http://www.cosmos.esa.int/web/xmm-newton
[2] http://www.cosmos.esa.int/web/xmm-newton/sas

the latest developments of software and/or the latest calibration files. The pipeline used for reducing *XMM-Newton* data are different for different instruments. The default meta tasks/chain task for pipeline processing of pn and MOS exposures are epproc/epchain and emproc/emchain, respectively. Through out this thesis, we have used only EPIC-pn observations taken in imaging mode. So, in this section, the reduction and analysis techniques used for imaging mode of EPIC-pn will be discussed.

The EPIC/pn camera takes images of a target source for the energy range $0.15-15$ keV, but data above 10 keV are dominated by strong proton flaring. X-rays emitted below 0.3 keV are highly affected by hydrogen along the direction of the object in our own galaxy. Moreover, the on-axis effective area of the EPIC pn camera play an important role in the performance of the X-ray mirrors. These mirrors can reflect X-ray photons most efficiently in the energy range from 0.1 to 10 keV. Therefore, for better quality and higher accuracy of the data set, we choose the energy range from $0.3-10$ keV for the light curve extraction. By doing this we automatically eliminate the effect of absorption in the lower energy range and the background noise in the higher energy range.

For scientific analysis, we required the event list files and the auxiliary files which contains detailed information of each frame recorded during the exposure. Event files of the pn detector were generated through the meta task *epchain*, which produces calibrated event lists running all the first-level pn task. It generates one event list for each exposure and bad pixel lists calling the main subroutine *epframes, badpixfind, badpix, epevents and attcalc*. Depending on requirements one can also run all the subroutines individually that are inside the proc meta tasks. The events list obtained from the pipeline processing meta task need to be reprocessed to generate scientific products e.g., image, time series data (light curve) and spectra. So the event list is filtered applying different selection criteria as per requirement of the user.

Before generating a cleaned event list, first we generated a light curve for energy range of 10–12 keV and see the soft proton flares effect on this and then generated

a good time interval file using the *TABGTIGEN* tool which contains information of the good times that are free from soft proton flares. In the next step, we used the event list file and GTI files as input to obtain cleaned event files and we later filtered the data using the condition $(PATTERN \leq 4)$ energy range $0.3-10$ keV and $(FLAG{=}0)$. The condition $(PATTERN \leq 4)$ allows both the single and double events that are registered by the detectors. FLAG represents the data quality. When we set $(FLAG{=}0)$ in the selection criteria, it removes all the events that are at the border of a CCD. With cleaned event files, we have generated source images and for source event files, the bright circular source region of 40 arcsec radius is selected in such a way that 90 per cent of the source flux lies inside the circle, for background event files, we selected a circular region of maximum possible size (which ranged between $40-50$ arcsec for different images/CCD chips), but as far away as possible on the same CCD chip to avoid any contribution from the source region.

Pile up is a common problem for very bright sources like blazars and is an issue for several observations in our studies. Pile up occurs when two or more X-ray photons fall on a single CCD pixel before the instrument's read out time, and as a result, the CCD will recognize these separate photons as a single one with energy equal to the sum of the individual energies of the two or more photons (see Jethwa et al. (2015) for more detail). It also may arise when more than one photon is detected by two or more adjacent pixels during a single read-out cycle. This pile up problem is detected by using *epatplot* routine for all the observation IDs. There are two ways to identify presence of pile-up through *epatplot*; (i) By checking the single to double events pattern ratio. If the observation is not affected by pile-up, the observed to model pattern ratio for both single and double events will be consistent with 1, but in presence of pile up the ratio for single events will be <1 and for double events it will be >1. and (ii) By checking the pattern distribution of data. Deviation of the observed (data) pattern distribution from the model will be there in presence of pile up. We removed the problem by selecting an central annulus region instead of circular region for both the source events file and background events file as used before in non-pile up affected observations on the same CCD chip. The pile-up affected pattern distribution in case of 3C 273 (Obs. ID 0414190501) is shown in the Fig. 2.9. Deviation of single and double distribution from the model is observed in

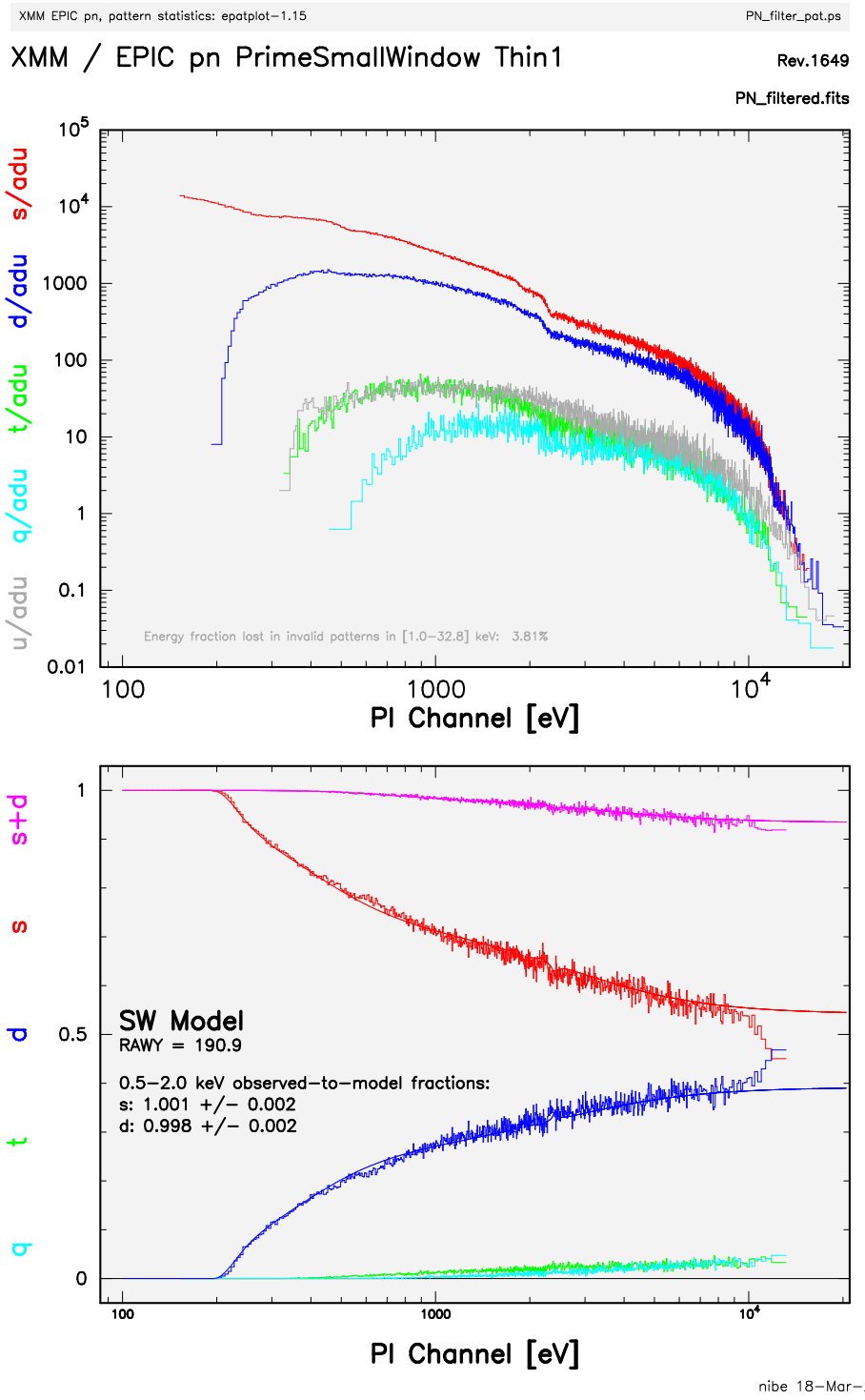

Figure 2.9: Pattern distribution of EPIC-PN with respect to energy (for the FSRQ 3C 273, Observation ID 0414190501) with pileup. The distribution is generated by the SAS task *epatplot* considering double events. Deviation of observed pattern from the predicted pattern distribution is visible above 8 keV

the higher energy range. Fig. 2.10 shows the pile-up corrected distribution of single and double events.

Since the observations we have used here in our study were carried out in different window mode (with different time resolution), we used different time binning for light curve generation. We obtain the final corrected events list by subtracting the background counts from the source counts. The events list files obtained by using the *epiclccorr* task contains some null points occurring when the window of the CCD chip was being closed during that exposure time. Also there are some fictitious points which show significantly larger error bars than the others with a peculiar deviation in counts from the normal order at the start or end in the events list; these originate when the source exposure time is less than 70 per cent of the window flag time. These points were removed to generate the final corrected time series. After correcting all these issues, we finally plot the light curves for observations.

2.2.4 Optical Light Curve Generation

In our study we have used only the imaging mode data of OM. Optical/UV data were processed with the *omichain* pipeline, as instructed in the SAS Analysis thread[1]. The meta task triggers different sub routine within SAS for full processing of raw ODF data set and gives the output files e.g., mosaiced sky-image, combined source-list, etc.. The observation source list contains the calibrated count rates and magnitude with their corresponding errors for each filters. The source list contains several objects and their corresponding data points are treated as background points. The objects near to the source coordinate appear in the source FOV with similar RA and DEC values. We identify our source from this object list by selecting the right RA and DEC value for our source and since the blazar is among the brightest objects in the OM FOV, the source will have very large counts rate in all filters.

[1] http://www.cosmos.esa.int/web/xmm-newton/sas-threads

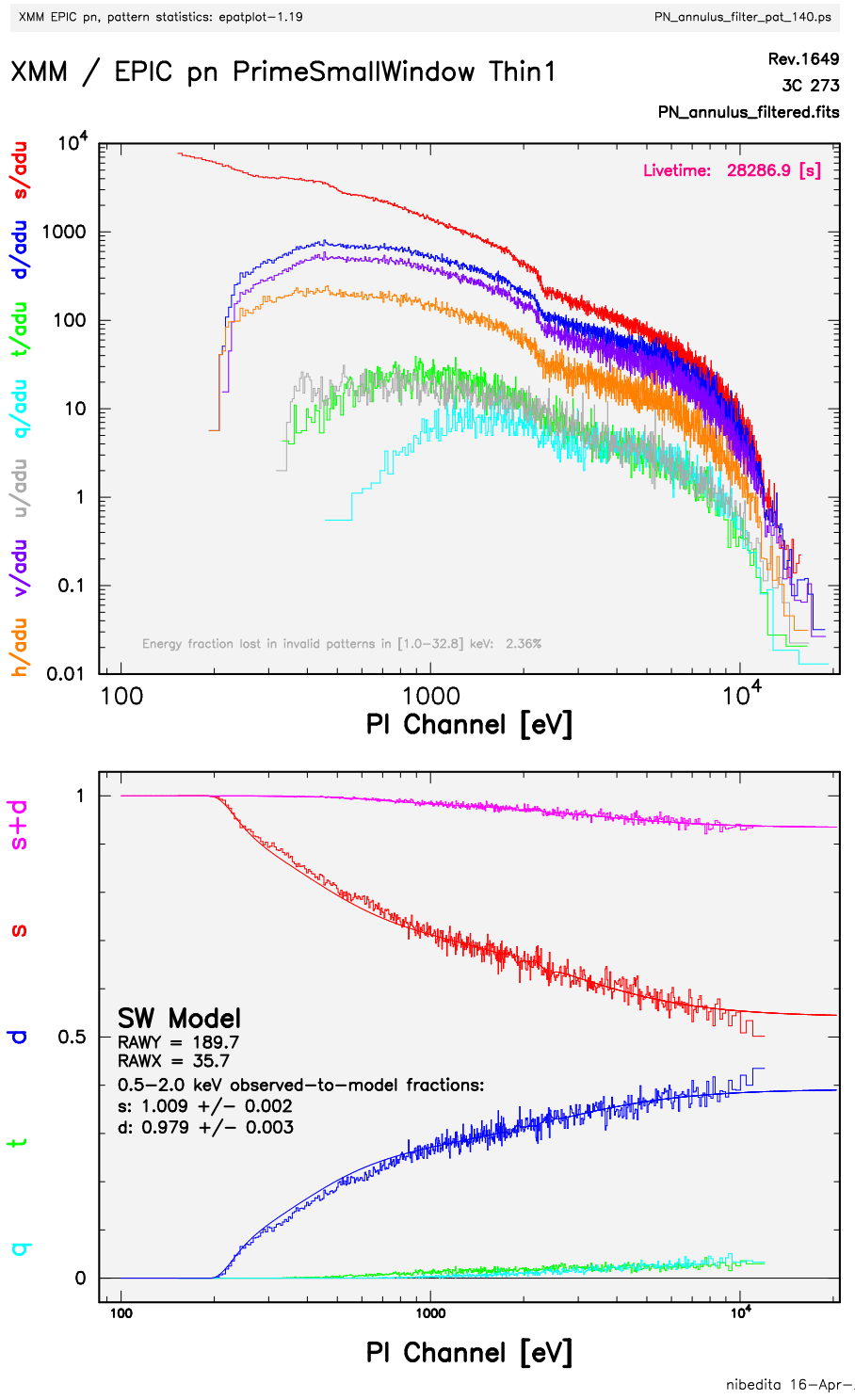

Figure 2.10: Pileup corrected pattern distribution of EPIC-PN with respect to energy (for the FSRQ 3C 273, Observation ID 0414190501). The distribution is generated by the SAS task *epatplot*

2.2.5 Spectral Product

For spectral analysis, Science Analysis Software (SAS) version-14.0.0 is used. Detailed information about the data and techniques used to reduce the data are discussed in above section, so here we will only discuss the methods used for spectral product generation.

Due to sensitivity limits we considered only EPIC-pn observations taken in imaging mode (e.g. Strüder et al., 2001). Lengths of the data trains are restricted to $\geq$ 8 ks, so as to produce statistically significant results. We only include on-axis observations in the spectral study. Like the time series data, filtering of calibrated event files is necessary for generating spectral products also.

For the source and background spectra, circular regions of 40 arcsec, centered on the source area and on a source-free region are selected, respectively, using the *EVSELECT* task. A spectral binsize of 5 is considered with both single and double events in the energy range 0.3–10 keV. Pile-up can be minimized to some extent by considering only single pixel events for the spectra, but this method reduces the sensitivity of the data and causes a loss of events. Therefore we have considered both single and double pixel events for spectra generation. The pile-up correction is tackled by removing the central portion of source region where depression of photon counts is maximum. The source and background spectra were extracted from an annulus region following the method explained in Molendi & Sembay (2003). The *SAS* task *EPATPLOT* is used to check for possible pile-up in the observations. For this, the pattern statistics were first checked for a circular region of 40″ radius centered on the source. If pile-up is detected, an annular region of inner radius of 6″ and outer radius of 40″ was considered first to reduce pile-up and then the pattern plot was rechecked. Depending on the degree of pile-up, the radius of the excluded inner area varies. We gradually increase the inner source radius till the pile up is removed which is determined through a pattern plot. Through this process the inner radius was varied from 6″–10″, but the outer radius was fixed at 40″ for all the pile-up affected observations. The redistribution matrix is then generated using the SAS task *rmfgen*. The final background-subtracted spectra were extracted using the

Table 2.1: Comparison of *XMM-Newton* with other X-ray observatories. Data taken from *XMM-Newton* User Handbook.

Satellite	Mirror PSF FWHM($''$)	E range (keV)	Mirror effective area at 1 keV (cm^2)	Orbital target visibility (hr)	Energy resolution at 1 keV (eV)
XMM-Newton	6	0.15-12	4650	36.7[a]	4 (RGS)
Chandra	0.2	0.1-10	555 (ACIS-S)	44.4[a]	1 (HETG)
ROSAT	3.5	0.1-2.4	400	1.3[b]	500
ASCA	73	0.5-10	350	0.9[b]	100
Suzaku	n.av.[c]	0.2-600	1760 (XIS)	0.72[b]	50
RXTE	n.a.[d]	2-250	n.a.[d]	1[b]	n.a.[d]
Swift	8.8	0.2-10(XRT)	133.5	$\sim$0.8[b]	70
NuSTAR	18	3-79	n.a.[d]	$\sim$0.8[b]	n.a.[d]

[a]Orbital visibility outside the particle-radiation dominated zone
[b]Low orbit with Earth occultation
[c] not available, [d]not applicable

task *grppha*. The resulting spectra were rebinned with 250 counts per channel with a oversample upper limit of 3 for good intrinsic energy resolution.

There are some negative consequences that arise from removing the central source region from the piled-up observations. Pile-up corrections may cause loss of spectral flux and distortion of the spectra at their high energy ends. Thus a high energy break appears near or above 8 keV in those pile-up corrected spectra. To correct for the flux loss and energy distortion caused by the pile-up of photons we use the task *rmfgen* which can only be applied for EPIC-PN observations taken in imaging mode. This is done by generating a response file (rmf) from the raw events file which includes the pile-up correction. Later this rmf was used to generate the grouped spectra. Even after applying this correction, the break remains to some degree and can be seen from the residual plots. Even using only single event spectra we cannot completely eliminate the pile-up problem and both the flux loss problem and the high energy break remain regardless. So, without compromising the sensitivity, we chose to take both single and double events for spectra generation.

2.3 Comparison of *XMM-Newton* with other X-ray Satellites

Most of the astronomical objects either galactic of extragalactic emit in X-ray bands, thus elevating the need to study these sources and their high energy emission mechanisms in X-ray regime. X-ray astronomy is one of the most fascinating and sophisticated research field as the emission processes involved with it are poorly understood. Considering the high-end instrument specifications, *XMM-Newton* is one of the best X-ray satellite to perform X-ray astronomy. The detectors sensitivity of *XMM-Newton* is very high, which have the highest effective area of a focusing telescope to date. Each X-ray telescope have a mirror geometric effective area of 1550 cm^2 at energy 1.5 keV which gives a total effective area of 4650 cm^2. Moreover the the angular resolution of the telescopes is high with a point-spread-function (PSF) having FWHM of $\sim 6''$.

In comparison, *Chandra* is a high resolution X-ray mission, however, its mirror effective area is much smaller than that of *XMM-Newton*. In addition to that the *XMM-Newton* instruments can operate independently and simultaneously in favorable conditions (i.e., if the target is not extremely luminous), but this facility is not available in *Chandra* observatory. The broader energy bandpass (0.15–12 keV) of *XMM-Newton* is another plus point. The satellite can observe a target continuously for 36.7 hours, which is the exact requirement to study source variability. The comparison of specifications between *XMM-Newton* and other X-ray satellites is shown in Table 2.1

Chapter 3

Multi-wavelength Variability in the Blazar 3C 273

3.1 Introduction

Blazars show flux variations in all bands of the EM spectrum on all possible timescales. Those fluctuations ranging from a few tens of minutes (and sometimes even more rapid) to less than a day in our observer's frame are often known as intra-day variability (IDV) (Wagner & Witzel, 1995). Variability with time scales of few days to weeks is commonly known as short term variability (STV), while variability on time scales ranging from months to the longest we have monitored (typically several years) is called long term variability (LTV) (Gupta et al., 2004). The IDV in blazars is the least well understood type of variations but it can provide an important tool for learning about structures on small spatial scales and it also provides us with better understanding of the different radiation mechanisms that are important in the emitting regions (e.g., Wagner & Witzel, 1995). Any characteristic time scale of variability can effectively provide us with information about the physical structure of the central region and complex phenomena such as hot spots on accretion discs (e.g., Mangalam & Wiita, 1993). In blazars, it is widely believed that most variability originates mainly from enhanced emission in a small region within the relativistic jets (Begelman et al., 2008). For example, excess emission could be triggered by dissipation inside a blob of material emerging from at the jet base, from

shocks propagating along the jet, or from instabilities within the jet itself.

3C 273 ($\alpha_{2000.0}$ = 12h29m06.7s, $\delta_{2000.0} = +02^{\circ}03^{'}09^{"}$, z =0.158339) was the first quasar discovered in the radio sky survey at 158 MHz that was included in the third Cambridge (3C) catalogue (Edge et al., 1959). In early 1963, it was classified as a FSRQ (Schmidt, 1963). Unsurprisingly, this relatively nearby blazar has been extensively studied on diverse time scales across the complete EM spectrum, with measurements made in single bands and often as well as in multi-bands (e.g., Abdo et al., 2010c; Attridge et al., 2005; Collmar et al., 2000; Courvoisier et al., 2003; Dai et al., 2009; Fan et al., 2014, 2009; Greve et al., 2002; Jester et al., 2005; Kataoka et al., 2002; Mantovani et al., 2000; McHardy et al., 2007; Pacciani et al., 2009; Sambruna et al., 2001; Savolainen et al., 2006; Soldi et al., 2008, and references therein).

This source has been studied in optical bands since its discovery. Optical (V, R and I band) studies show the variable flux in the source changes with different amplitudes on different timescales revealing the nonlinear variability characteristic of blazars. It was also noticed that, at higher frequencies, the strength of the flux variations in 3C 273 are higher than in the lower frequencies (Fan et al., 2009). This type of frequency dependent variability is also valid for near-infrared bands (Wen et al., 2002). While monitoring the source in optical bands from 1998 to 2008, (Fan et al., 2014) found that during this period the source did not show very significant IDV but it showed strong LTV. Imaging data from *Hubble Space Telescope* in the UV show compatibility of far-UV with extrapolated 0.5−8 keV X-ray flux, thereby supporting a common origin of UV and X-ray emissions in the relativistic jet (Jester et al., 2007). Long-term optical observations in BVRI bands from 2003 to 2005 with the Yunnan National Astronomical Observatory (YNAO) 102 cm telescope and Shanghai Astronomical Observatory (SHAO) 156 cm telescope show that the source was in a rather steady flux state during this campaign (Dai et al., 2009). The same study shows strong inter-band correlations of color index and magnitude in the optical regime, where the spectrum becomes flatter when the source brightens and softer when the source brightness decreases for both IDV and LTV, which is similar to spectral evolution of most BL Lacs.

Soldi et al. (2008) used various ground and space based telescope data to study the variability in the source over almost the entire EM spectrum (i.e., radio to $\gamma-$rays) for about a decade. Their study revealed energy dependent variability time scales and variability amplitudes of 3C 273. The variability in X-ray bands indicate the presence of two different components, one of them which can be considered Seyfert-like while the other is blazar-like. A contemporary study of the source with *BeppoSAX* and *XMM-Newton* interprets the Seyfert-like component and soft excess as the result of a non-thermal flare-like coronal model (Pietrini & Torricelli-Ciamponi, 2008). The hard X-ray variability correlated with long term optical variability but not to radio variability, which indicates that the emission mechanism for hard X-rays ($\geq$ 20 keV) is not due to electrons accelerated by the shock waves in the jet but probably arises from inverse Compton scattering of synchrotron optical photons emitted from a region near the base of the jet by the same electron population (Soldi et al., 2008).

A soft X-ray study of 3C 273 by *ROSAT* showed short term variability of about 20 per cent over $\sim$ 2 days (Leach et al., 1995). *RXTE* observations of the source at hard X-ray bands found similarly modest variations over several days but variability up to a factor of four over four years (Kataoka et al., 2002). The high correlation between X-ray ($3-20$ keV) and IR fluxes provides evidence for the origin of X-ray emission in 3C 273 being a result of the Compton scattering of low-energy seed photons (McHardy et al., 1999). However, the X-ray emission from 3C 273 shows different timing properties for variability below and above $\sim$ 20 keV and this produces uncertainty about the origin of the hard X-ray emission, which was previously considered to be part of the jet emission (Soldi et al., 2008). They have studied fractional variability amplitude and characteristic time scale with structure function (SF) analysis using *XMM-Newton* data from $2000-2005$. This analysis technique to study variability has been used frequently by the community. Vagnetti et al. (2011) performed SF to study the X-ray variability for this source with *XMM-Newton* data and found that the variability is anti-correlated with X-ray luminosity. During the period 2000-2009, Liu & Zhang (2011) studied STV in soft and hard X-ray bands with the help of *XMM-Newton* satellite, and they reported that soft and hard X-rays come from different origins. Brightman & Nandra (2012) used clas-

sical hardness ratio to find an effective colour−colour selection for obscured AGN from X-ray data using a sample of heavily absorbed AGN (including 3C 273).

A recent study has indicated that the physical process initiating variability in the X-ray domain of 3C 273 is similar to that in Seyfert galaxies (McHardy, 2013). 3C 273 has long been known to have a soft excess in the X-ray band at ≤ 1 keV (Turner et al., 1985). Many studies have shown a soft excess at energies ranging from 0.1−2 keV (e.g., Chernyakova et al., 2007; Courvoisier et al., 1987; Page et al., 2004; Pietrini & Torricelli-Ciamponi, 2008; Türler et al., 2006, and references therein). It was also detected as one of the first extragalactic γ−ray sources by the COS-B satellite (Swanenburg et al., 1978).

A wavelet analysis of X-ray time series data of 3C 273 taken by *XMM-Newton* indicated a candidate 3.3 ks quasi-periodic oscillation (QPO; Espaillat et al. (2008)). With the assumption that the QPO is generated near the last stable orbit in the accretion disk the central black hole mass is constrained to lie between $7.3 \times 10^6\ M_\odot$ if it is a Schwarzschild BH and $8.1 \times 10^7\ M_\odot$ for a maximally rotating Kerr black hole. However, previous reverberation-mapping estimates gave much higher masses of $2.35 \times 10^8 M_\odot$ (Kaspi et al., 2000) and $6.59 \times 10^9 M_\odot$ (Paltani & Türler, 2005) which would imply that this QPO is not due to the dynamical motion in the inner accretion disk, but perhaps due to oscillation modes in the accretion disc (Espaillat et al., 2008). Subsequent studies have, however, called into question the presence of a QPO in 3C 273 (González-Martín & Vaughan, 2012; Mohan et al., 2011).

Although the emission mechanism for blazars is not yet completely understood, it is clear that the lower energy photons arise from synchrotron emission and in many cases this emission extends into the soft part of the X-ray band. Contributions from synchrotron self-Compton (SSC) and external Compton (EC) are the two main candidate mechanisms to dominate the harder part of X-ray emission and produce the γ-ray emission. The harder X-ray emission also can have a contribution from the Compton scattering of disc photons by the hot corona sandwiching the disc (Ghisellini & Tavecchio, 2008; Sikora et al., 1994). Studies have also shown strong correlation between IR and X-ray emission from time to time, in the sense that the

IR leads the X-ray emission, supporting the SSC model (McHardy et al., 2007).

Multi-wavelength (optical, UV and X-ray) LTV and interband correlation of this source with *XMM-Newton* data available till date (2012) is done for the first time by us in the present work. LTV of 3C 273 in X-ray bands was studied previously in different time period by different groups, but here we study LTV of this source for the longest period ever done in X-ray bands, both soft and hard bands using *XMM-Newton* data. We also study the LTV in optical and UV bands in the same period with Optical Monitor (OM) data, which has not done before. IDV studies on a few occasions are done in past but we have studied here IDV in X-rays with all the time series data available for the source till 2012.

In this work, we study IDV and LTV of the FSRQ 3C 273. In the next section, we discuss *XMM−Newton* archival data. In Section 3.3, we report our results and in Section 3.4, we present a discussion and the conclusions of the work.

3.2 Data Selection & Analysis Techniques

3.2.1 X-ray Data

3C 273 has been frequently observed with different telescopes over different frequency ranges. The *XMM−Newton* is one of the rare instruments that is capable of observing a particular source in multiple bands simultaneously, in this case in the Optical, UV and X-ray bands (see Chapter 2 for details). *XMM−Newton* has observed 3C 273 for over a decade in time in X-ray, optical and UV making it possible for us to study variability on different time scales.

In this work we have used *XMM−Newton* satellite data to study the behaviour of the source in all three bands. Observation data files (ODFs) were downloaded from the on-line *XMM-Newton* science archive. For reduction of these data we have used *XMM-Newton* Science Analysis Software (SAS) version 12.0.1. As discussed in Chapter 2, the on board system of *XMM−Newton* contains the EPIC, which consists of two CCD arrays, MOS and pn. Here we have used EPIC/pn camera obser-

vations for our purpose, since the sensitivity of EPIC/pn is much higher than that of the MOS camera (Strüder et al., 2001). *XMM−Newton* has data for the source 3C 273 from June 13, 2000 to July 16, 2012 which is comprised of a total of 34 observations in *XMM-Newton* science archive. However, out of these 34 observations two observation IDs do not contain any data, and pn data was not available for four other observation IDs. Three more observations were excluded because of their bad image quality. So here we have studied 25 observations for the source 3C 273. The 3C 273 public data over the 12 year span is given in Table 3.1. In addition to general information of the observations, the good time interval available for science analysis, presence or absence of pile-up and mean count rate of the extracted time series are presented in column no. 5, 6 and 8 of Table 3.1, respectively for each pointings.

3.2.2 Optical/UV Data

The Optical/UV Monitor Telescope (OM hereafter) on board *XMM-Newton* provides the facility to observe simultaneously a particular source in optical and UV bands along with the X-ray bands, with a very high imaging sensitivity (Mason et al., 2001) (see Chapter 2). This makes possible the study of the relationship between the emission mechanisms corresponding to these bands. 3C 273 was observed with OM for differing numbers of exposures for different observing periods (see Table 3.1 for details). The source was simultaneously observed with both X-ray and Optical/UV telescopes for a total of 16 observation IDs.

3.2.3 Excess Variance

Blazars show very rapid flux variability in all wave bands from radio to $\gamma-$rays. To measure the strength of variability, the commonly used parameters are excess variance, σ_{XS}^2 and fractional rms variability amplitude, F_{var}, (Edelson et al., 2002). Each light curve obtained from different exposures contains information on flux measurements (count rates) with its uncertainties caused by measurement errors for different time intervals. Excess variance gives the intrinsic variance of the source by removing the variance due to measurement errors in each individual flux measurement. When the light curve consist of total number n of flux measurements x_i, at

Table 3.1: Summary of *XMM-Newton* data for 3C 273 during 2000−2012

Date of Obs. dd.mm.yyyy	Obs.ID	Revolution	Window Mode	GTI (ks)	Pile up	Filter	μ (counts s^{-1})	OM filter[1]	Exposures[2]
13.06.2000	0126700101	94	Full Frame	Nil	Nil	MEDIUM	Nil	6	5
13.06.2000	0126700201	94	Full Frame	Nil	Nil	MEDIUM	Nil	6	5
13.06.2000	0126700301	94	Small	64.9	No	MEDIUM	47.04±0.81	1,2,3,4,5,6	29
15.06.2000	0126700401	95	Full Frame	Nil	Nil	MEDIUM	Nil	6	5
16.06.2000	0126700501	95	Full Frame	Nil	Nil	MEDIUM	Nil	6	5
15.06.2000	0126700601	95	Small	29.6	No	MEDIUM	45.41±0.80	4,5,6	15
15.06.2000	0126700701	95	Small	29.9	No	MEDIUM	44.16±0.80	1,2,3	15
17.06.2000	0126700801	96	Small	60.1	No	MEDIUM	44.26±0.79	1,2,3,4,5,6	30
13.06.2001	0136550101	277	Small	88.5	Yes	MEDIUM	21.58±0.58	1,2,3,4,5,6	12
16.12.2001	0112770101	370	Small	4.9	No	THIN1	71.95±1.00	Nil	Nil
22.12.2001	0112770201	373	Small	4.9	No	THIN1	69.50±0.99	Nil	Nil
09.01.2002	0137551001	382	Burst	Nil	Nil	MEDIUM	Nil	6	1
07.07.2002	0112770601	472	Small	4.9	No	THIN1	53.93±0.87	Nil	Nil
17.12.2002	0112770801	554	Small	4.9	No	THIN1	77.54±1.04	Nil	Nil
05.01.2003	0112770701	563	Small	4.9	No	THIN1	65.32±0.96	Nil	Nil
05.01.2003	0136550501	563	Small	8.4	No	MEDIUM	63.22±0.94	2,3	2
18.06.2003	0112771001	645	Small	5.4	No	THIN1	80.24±1.09	Nil	Nil
07.07.2003	0159960101	655	Small	58.0	Yes	THIN1	26.05±0.57	1,3,4,5,6	5
08.07.2003	0112770501	655	Small	8.0	No	THIN1	70.66±1.04	Nil	Nil
14.12.2003	0112771101	735	Small	8.3	No	THIN1	53.34±0.87	Nil	Nil
30.06.2004	0136550801	835	Small	19.7	No	MEDIUM	45.27±0.81	1,2,3,4,5,6	6
10.07.2005	0136551001	1023	Small	27.5	No	MEDIUM	49.68±0.84	1,2,3,4,5,6	6
12.01.2007	0414190101	1299	Small	76.5	Yes	MEDIUM	21.42±0.52	1,2,3,4,5,6	9
25.06.2007	0414190301	1381	Small	31.9	No	MEDIUM	45.90±0.80	1,2,3,4,5,6	8
08.12.2007	0414190401	1465	Small	35.3	Yes	MEDIUM	38.16±0.69	1,2,3,4,5,6	6
09.12.2008	0414190501	1649	Small	40.4	Yes	THIN1	21.57±0.52	1,2,3,4,5,6	6
20.12.2009	0414190601	1837	Small	31.3	Yes	THIN1	24.36±0.57	Nil	Nil
10.12.2010	0414190701	2015	Small	35.8	Yes	THIN1	18.29±0.48	1,2,3,4,5,6	6
12.12.2011	0414190801	2199	Small	42.8	No	THIN1	47.48±0.82	1,2,3,4,5,6	6
16.07.2012	0414191001	2308	Small	25.5	No	THIN1	41.22±0.93	4,5,6	3

μ = mean count rate; GTI = Good Time Interval; [1] 1 = *UVW2*, 2 = *UVM2*, 3 = *UVW1*, 4 = *U*, 5 =*B*, 6 = *V*; [2] Total number of exposures combining all six filters

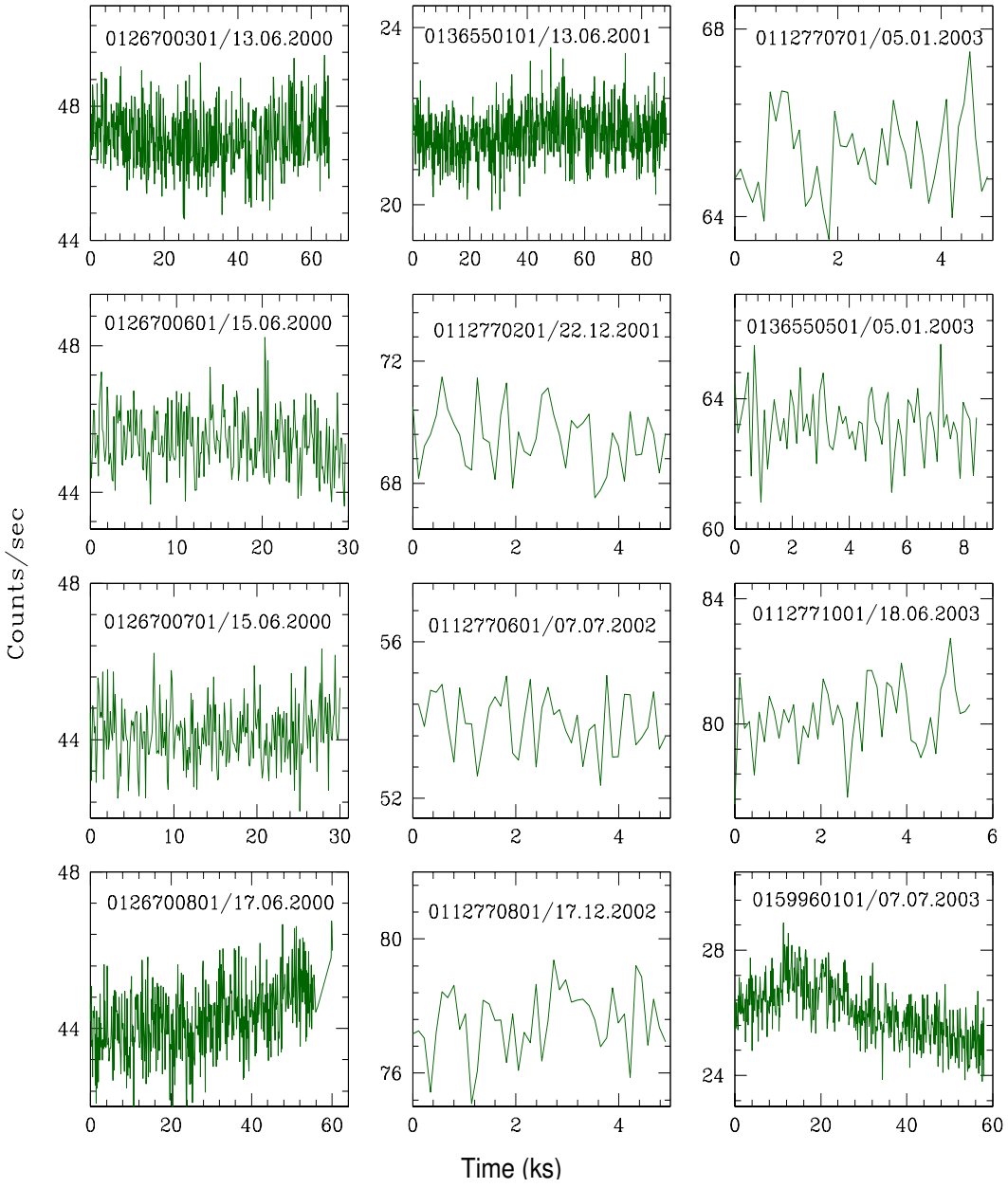

Figure 3.1: The variation of X-ray flux with time for 3C 273, for observations carried out at different times. The caption on each light curve represents observation ID and observing date, respectively. These light curves were extracted using 114 seconds time binning in the energy range, 0.3−10 keV.

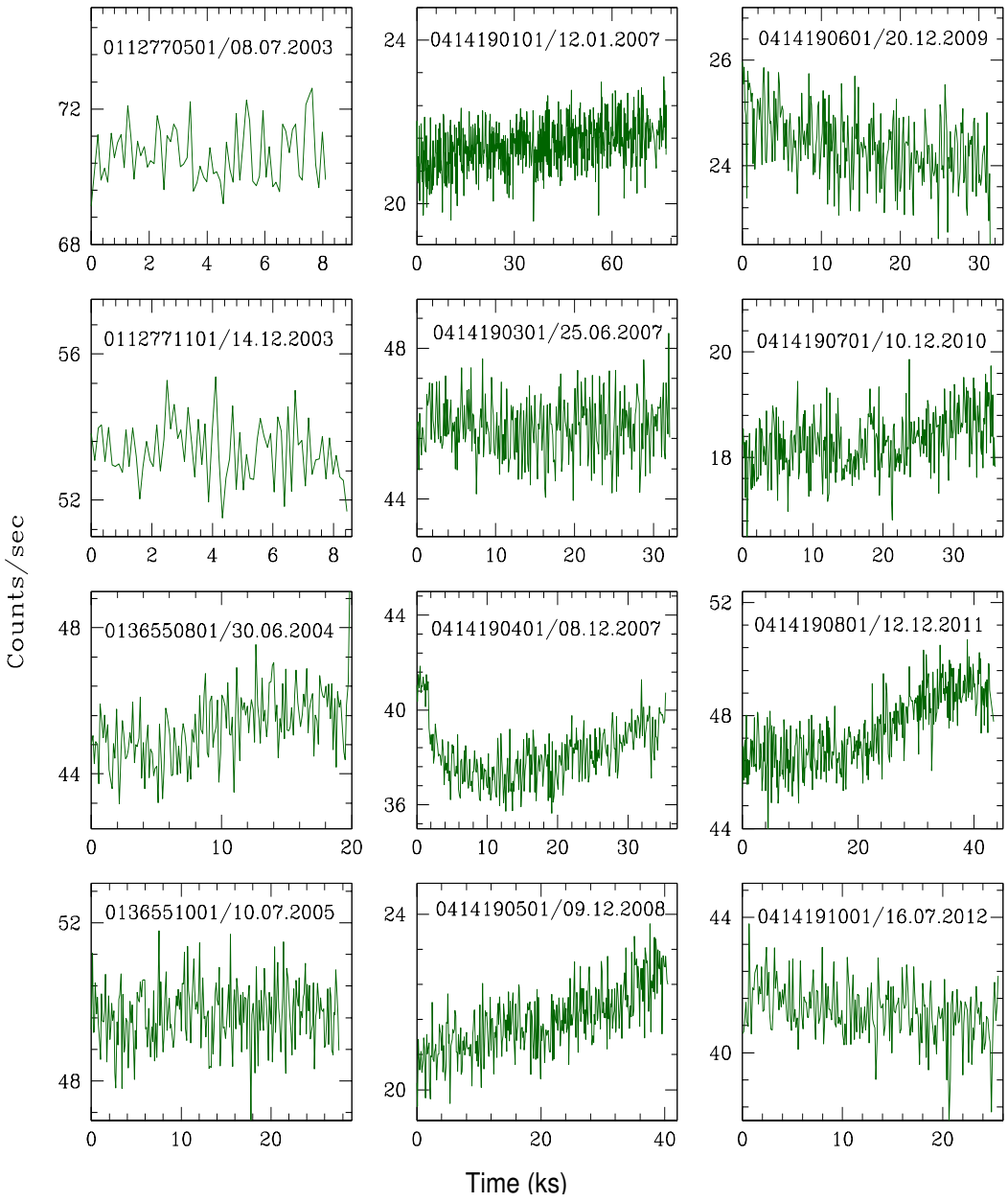

Figure 3.1: continued

times t_i, with corresponding errors in measurements $\sigma_{err,i}$, then the excess variance is calculated as

$$\sigma_{XS}^2 = S^2 - \overline{\sigma_{err}^2}, \tag{3.1}$$

where $\overline{\sigma_{err}^2}$ is the mean square error and S^2 is the sample variance of the light curve given by

$$S^2 = \frac{1}{n-1}\sum_{i=1}^{n}(x_i - \bar{x})^2 \tag{3.2}$$

and

$$\overline{\sigma_{err}^2} = \frac{1}{n}\sum_{i=1}^{n}\sigma_{err,i}^2. \tag{3.3}$$

The fractional rms variability gives the average variability amplitude with respect to the mean flux of a source, which is nothing but the square root of the normalized excess variance, σ_{NXS}^2, which is

$$\sigma_{NXS}^2 = \frac{\overline{\sigma_{XS}^2}}{\bar{x}^2} \tag{3.4}$$

so

$$F_{var} = \sqrt{\frac{S^2 - \overline{\sigma_{err}^2}}{\bar{x}^2}} \tag{3.5}$$

The uncertainty on F_{var} has been calculated using Monte Carlo method for n total events (Vaughan et al., 2003) and is given by

$$(F_{var})_{err} = \sqrt{\left\{\sqrt{\frac{1}{2n}}\frac{\overline{\sigma_{err}^2}}{\bar{x}^2 F_{var}}\right\}^2 + \left\{\sqrt{\frac{\overline{\sigma_{err}^2}}{n}}\frac{1}{\bar{x}}\right\}^2}. \tag{3.6}$$

3.3 Results

3.3.1 Intraday Variability in X-ray Light Curves

We have searched for IDV in X-ray light curves for those observations given in Table 3.1 that provided good data and those 24 light curves are plotted in Fig. 3.1. In Table 3.2, we have reported the IDV variability parameters which are calculated using excesses variance. It can be clearly seen that the IDV amplitude in the individual observations are low, usually less than 1 per cent and often consistent with 0, given the errors on F_{var}. The highest variability among all the observations taken during this time span is seen in the observation ID 0159960101 in 2003, and is 2.60 per cent, though the variabilities are essentially as large during two other observations (0414190401 and 0414190501). We note that the longer GTI observations produce higher probabilities of detecting clear variations.

In blazars, it is believed that the X-ray emission is a result of synchrotron radiation from highly energetic electrons moving with relativistic speeds in the jet. It can either be direct synchrotron radiation or results from inverse Compton scattering of lower energy photons off the synchrotron emitting electrons. In case of FSRQs X-ray emissions mainly come from inverse-Compton emission, but here in 3C 273, which is a exceptional case regarding the presence of both Seyfert like and blazar like components in its X-ray spectra, X-rays below 2 keV is due to coronal emission from the accretion disk and above 2 keV is dominated by contribution from jet emission (Haardt et al., 1998; Page et al., 2004; Pietrini & Torricelli-Ciamponi, 2008). Blazars show complex emission behaviour in X-ray flaring states. During these states the object can show both soft and hard lags depending on the time required for cooling and acceleration by radiating electrons. From the smallest variability timescale in X-ray band, the size of the central emitting regions of the blazar can be estimated. If IDV is found during the quiet state of the blazar, when the jet is weak or absent, then it may be attributed as result of changes occurring in the accretion disk, which can constrain the structure of the central engine on linear scales (Gupta et al., 2009). Intra-day X-ray variability may also be due to instabilities on or above the accretion disk, caused by its magnetic field that can also lead to generation of

oscillations in the disk.

3.3.2 Long Term Variation in Optical/UV & X-ray Bands

The source has been observed for more than a decade, which makes it possible for us to study its long term variability behaviour in X-rays as well as in Optical/UV bands. We examine long term behaviour of the source 3C 273 by combining the mean count rates for each observation. The temporal behaviour of the source in between 2000 and 2012, in 2 X-ray and 6 Optical/UV bands are plotted in different panels of Fig. 3.2. By visual inspection, variability is clearly seen in all of these bands.

We split the X-ray light curve into two light curves with the energy ranges being 0.3−2.0 keV for soft X-rays and 4.0−10 keV for hard X-rays. Previous studies (Haardt et al., 1998; Page et al., 2004; Pietrini & Torricelli-Ciamponi, 2008) have found that the disk emission is the origin of X-ray emission below 2 keV in 3C 273, where disk photons scattered off the hot corona above the disk, while emission above 2 keV comes from inverse-Compton scattering of seed photons by the relativistic jet. So we consider the energy range for soft X-ray band is 0.3−2 keV to be dominated by coronal emission but for the main contribution from the jet, we consider the hard band energy range 4−10 keV, in order to reduce contamination from the X-ray corona. Both the soft and hard X-ray light curves show very similar variability patterns. It seems that there was a small flaring in both the X-ray bands in June 2007 with almost no time lag. A similar kind of flare is seen in December 2007, in all the optical/UV bands when the X-ray fluxes are lower. Though we clearly do not have enough data points to formally calculate any time lag it is not unreasonable to estimate a time delay of the flare in Optical/UV bands with respect to the X-ray bands by visual inspection which give the delay of about six months. However, we cannot claim whether there was a correlation between these two emission peaks or if they originate from two independent emitting regions. We did not find any strong flares. But there are evidences of flares from the source on different occasions. Fan et al. (2014) studied the photometric observation of 3C 273 in optical bands from 1998 to 2008, where they reported detection of two peaks in

Table 3.2: X−ray variability parameters in the energy range 0.3−10 keV

Obs.IDs	Variance	$\sigma_{XS}^{2}{}^{a}$	$F_{var}{}^{b}$ (%)
0112770101	0.82	0.19	0.61±0.40
0112770201	1.04	0.06	0.34±0.66
0112770501	0.71	0.37	0.86±0.27
0112770601	0.56	0.20	0.83±0.42
0112770701	0.79	0.13	0.54±0.47
0112770801	0.95	0.13	0.47±0.46
0112771001	1.16	0.02	0.19±1.00
0112771101	0.69	0.08	0.51±0.46
0126700301	0.76	0.11	0.69±0.15
0126700601	0.63	0.01	0.16±0.85
0126700701	0.55	0.09	0.67±0.24
0126700801	0.77	0.15	0.88±0.14
0136550101	0.30	0.03	0.80±0.21
0136550501	0.90	0.01	0.12±1.47
0136550801	0.85	0.20	0.99±0.22
0136551001	0.60	0.10	0.65±0.23
0159960101	0.79	0.46	2.60±0.11
0414190101	0.33	0.06	1.15±0.17
0414190301	0.62	0.03	0.36±0.37
0414190401	1.44	0.96	2.57±0.12
0414190501	0.56	0.28	2.47±0.16
0414190601	0.48	0.15	1.61±0.20
0414190701	0.30	0.07	1.48±0.23
0414190801	1.58	0.91	2.01±0.10
0414191001	0.69	0.18	1.02±0.28

[a]excess variance;
[a]fractional rms variability amplitude

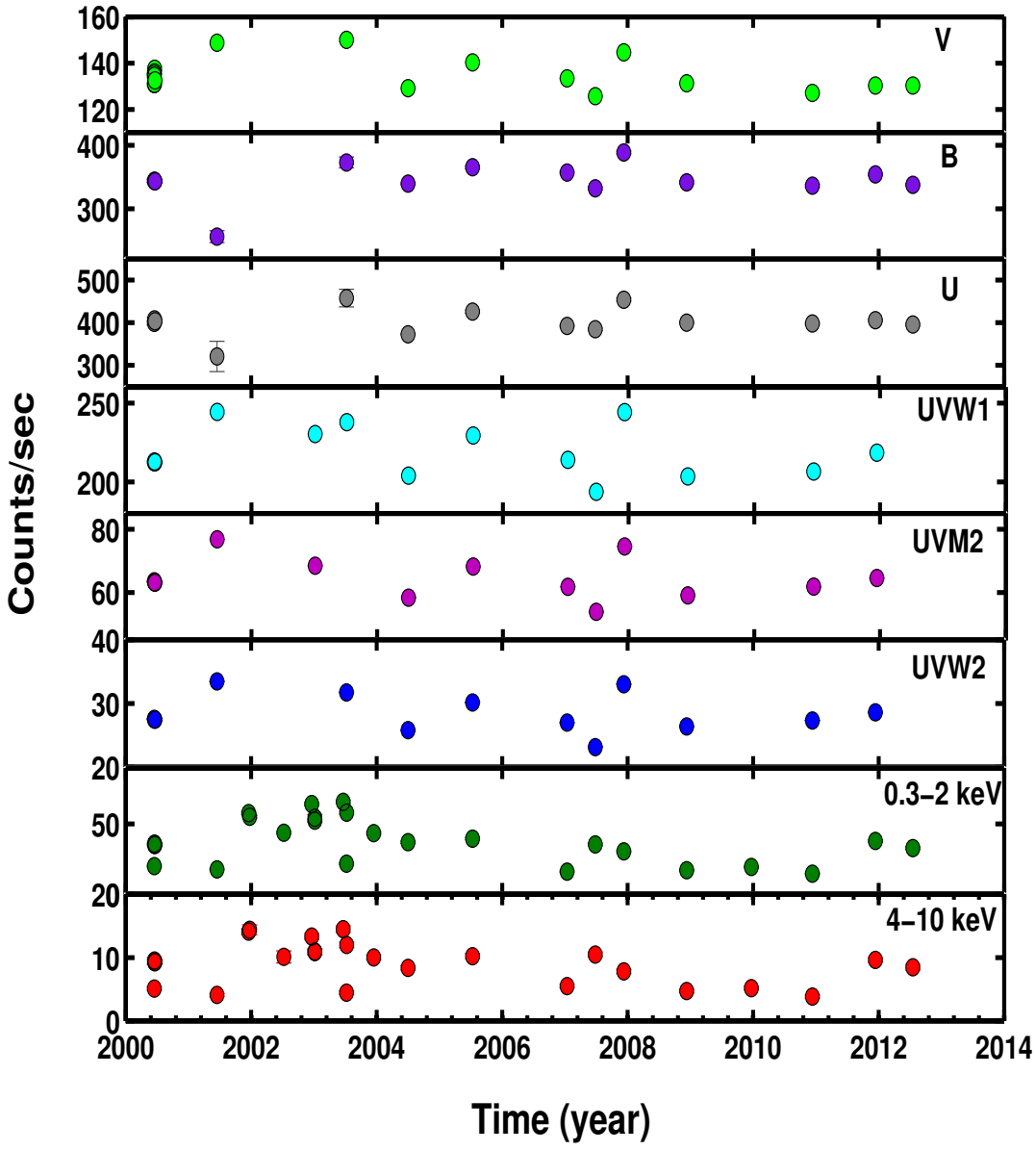

Figure 3.2: Optical/UV and X-ray long term variability (2000−2012). The lower panel shows two X-ray bands, hard and soft, respectively from the bottom. Three UV bands with increasing wavelength are plotted just above X-ray bands and in the upper panel, optical U, B and V bands are shown (error bars are smaller than the symbol size).

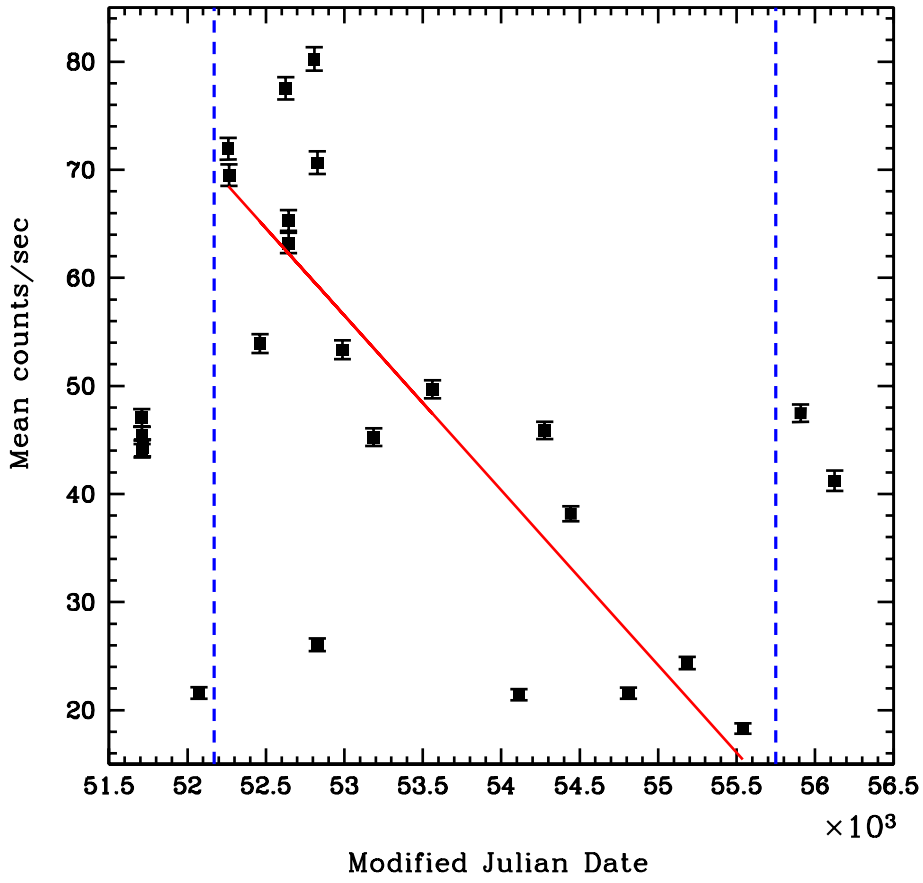

Figure 3.3: Long term X-ray variability in the energy range 0.3−10 keV of 3C 273 (2000−2012)

February 2006 and March 2008 in R band. Beaklini & Abraham (2014) reported a flare at 7 mm wavelength with Itapetinga Radio-telescope, in Brazil in 2010, which they claim as counterpart of gamma-ray flare detected in September, 2009 by the *Fermi / Large Area Telescope (LAT)* with a delay of 170 days. Frequent flares were detected by *Fermi/LAT* in gamma-ray bands in the period September 2009 to April 2010 (Rani et al., 2013).

Over the long term, 3C 273 showed large RMS variability amplitudes. The RMS variability amplitude for *UVW2, UVM2, UVW1, U, B, V* bands and soft and hard X-ray bands are, in per cent $\sim$ 76, 76, 68, 68, 68, 35, 42, and 36, respectively, with

respective percentage errors in variability amplitude of 0.016, 0.0104, 0.0867, 0.76, 0.30, 0.086, 0.475 and 0.983. Thus we conclude that the source is highly variable in both the optical/UV and X-ray domains during the above mentioned time period.

The overall change in the total X-ray flux with time during this observing period of 3C 273 is shown in Fig. 3.3. On visual inspection, if we exclude small portions of the starting and ending period of this observation there is indication of a linearly decreasing flux profile with time from December 2001 to December 2010. This data is fitted with least squares fitting method and the correlation coefficient for the fit calculated with MATLAB, is -0.8076 and its corresponding null-hypothesis is 0.001. In Fig. 3.3, the excluded parts of these observations are separated by vertical dotted lines.

3.3.3 Possible connections between Optical/UV and X-ray bands

From Fig. 3.2, visually it appears that the optical and UV bands follow the same variability pattern as do the soft and hard X-ray bands. To further examine the variability relations between these optical, UV and X-ray bands, we plotted these bands against each other as shown in Fig. 3.4. The upper left panel of Fig. 3.4 explicitly shows that soft and hard X-ray bands are well correlated. In the same manner, to check the correlation in flux variation within broad bands, we plot the optical V band against the B band and in similar way plot the UWV2 band against the UVW1 (shortest wavelength UV filter for the OM telescope). Clearly good correlations are found for all three intra-bands cases.

Similarly, Optical/UV and X-ray flux variabilities are checked by plotting soft X-ray vs V, and soft X-ray vs UVW1 which are shown in the left and middle panels of the bottom row of Fig.3.4. These plots do not show any correlations, but there is good correlation between the V and UVW1 counts. From this analysis, we conclude that the variability within the X-ray, optical & UV bands are closed related to each other and further that the optical emission follows the same trend as UV emission. But there is no obvious correlation between the variability trends for the X-ray and the Optical/UV emissions. We also calculated correlation coefficients; they and

Table 3.3: Variability Correlations between Optical, UV and X-ray bands

Bands	Correlation coefficient	Null hypothesis
Soft−Hard X-ray	0.9207	0.0
B-V	0.8845	0.0001
UVW1−UVW2	0.9862	0.00
Soft X-ray−V	-0.2308	0.4272
Soft X-ray−UVW1	-0.0012	0.9968
UVW1−V	0.9376	0.0

their corresponding null hypothesis tests for each pair of combinations are given in Table 3.3.

3.3.4 X-ray Hardness Ratio

The hardness ratio is evaluated by dividing hard band (4−10 keV) count rates by soft band (0.3−2 keV) count rates. To study the spectral evolution of the source, we examined patterns in the hardness ratio as a function of 0.3−10 keV count rates in the X-ray domain for different time spans. During this period of 12 years for which *XMM−Newton* observed 3C 273, the source has continuously evolved through spectral variations that are plotted in Fig. 3.5. These are best understood in terms of changes in the relative strength of particle acceleration and synchrotron cooling processes in X-ray emitting regions in 3C 273.

The results of this analysis provides a model independent spectral variability study of the source. Any loop occurring in the spectral hardness-flux representation, whether it is clockwise or anti-clockwise gives information about the leading emission mechanism during that period by considering the corresponding flux emitted at that time. So we plotted the hardness ratio points against the total X-ray count rates to see if any any loops appeared in the plot. Once a loop was visible in the plot, we terminated the plotting and marked that time span as an epoch and began a search for subsequent loops. In this process, we sometimes had to consider a single hardness ratio point as marking both the end of one loop plot and the beginning of another to best indicate the complete loops.

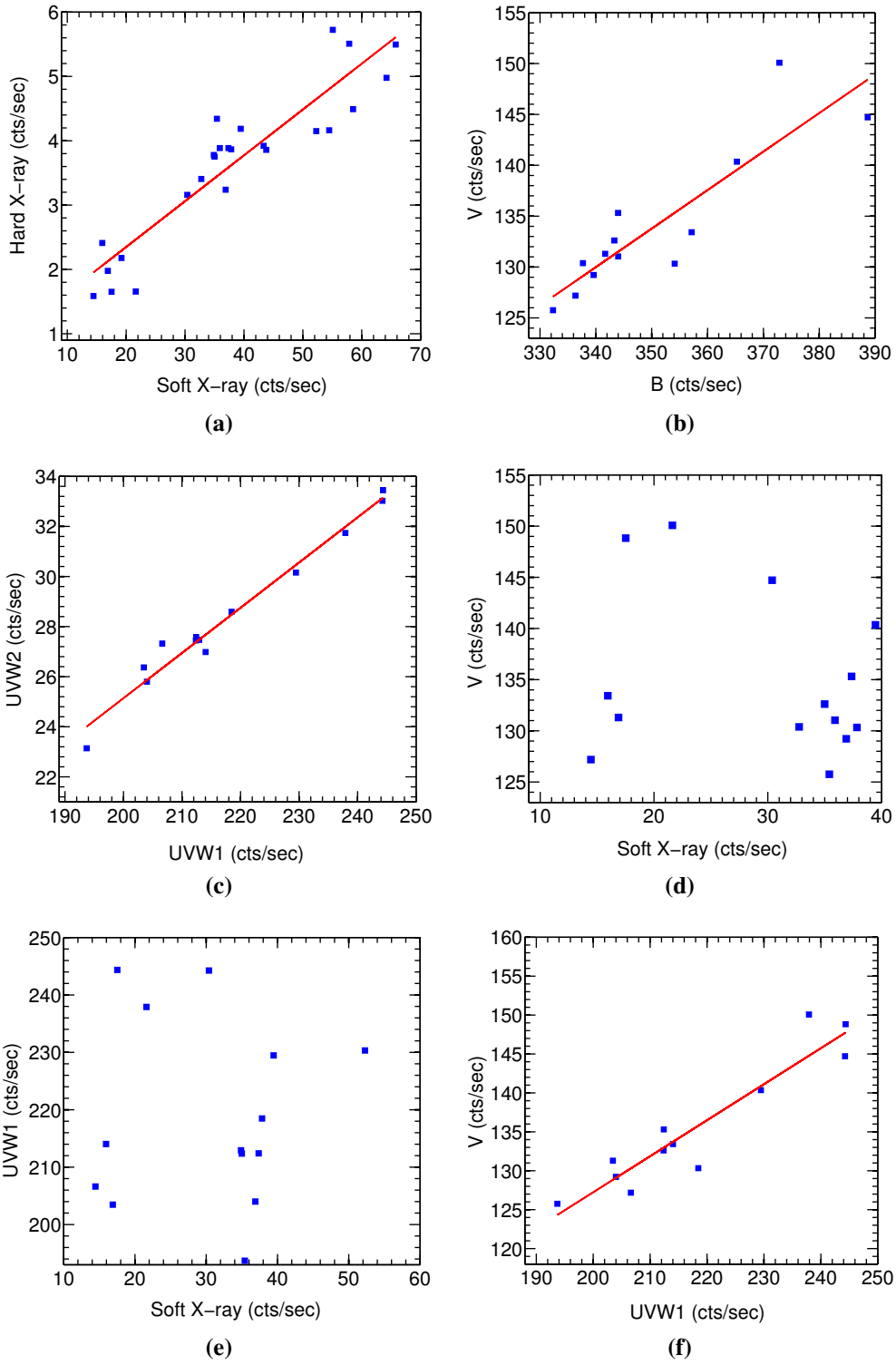

Figure 3.4: Correlations in variability between different optical, UV and X-ray bands.

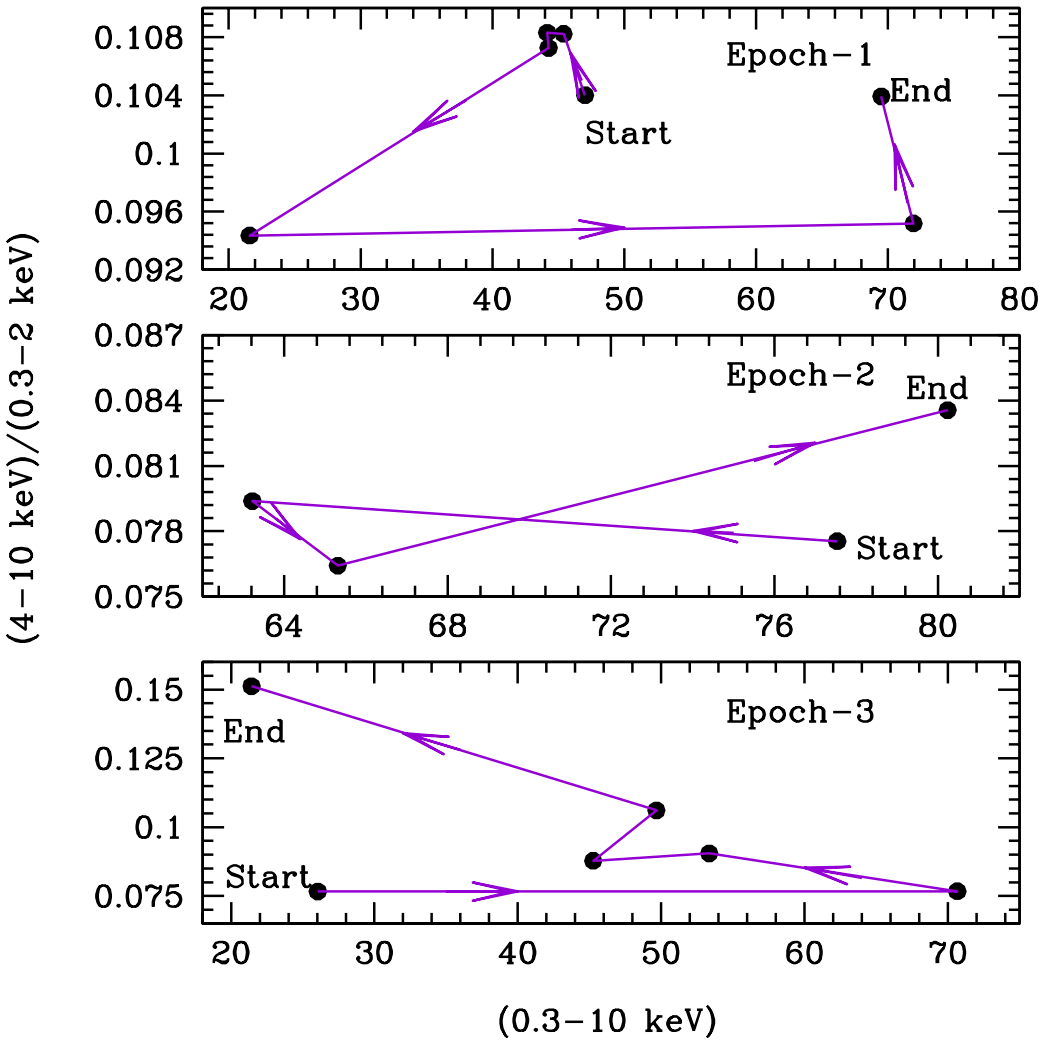

Figure 3.5: Spectral evolution of 3C 273 in different epochs. Arrows indicate the directions of the loops. Here the term epoch in the plots represent different time intervals during which the data were acquired for each corresponding loop: epoch−1 =13.06.2000−22.12.2001; epoch−2 =17.12.2002−18.06.2003; epoch−3 =07.07.2003−12.01.2007; epoch−4 =12.01.2007− 09.12.2008; epoch−5 = 06.12.2007−16.07.2012. The clockwise and anticlockwise loops are distinct and closed or nearly so, presenting a clear evidence of alternate acceleration and cooling mechanisms.

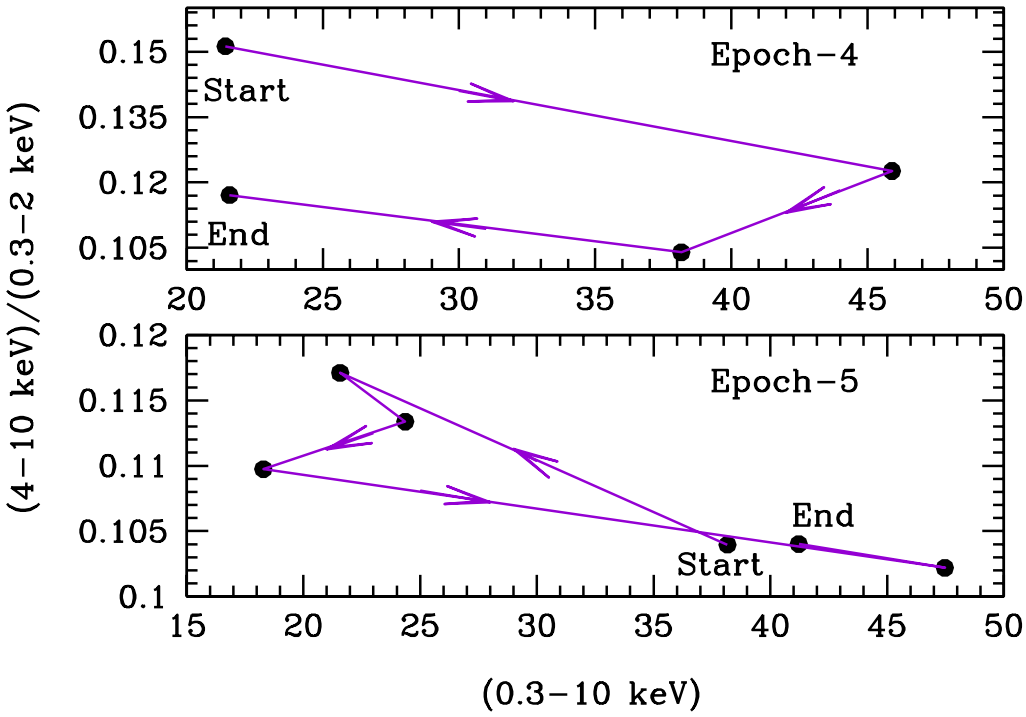

Figure 3.5: continued

The widely accepted picture for the X-ray emission is that shock propagation in the relativistic jet is responsible for accelerating particles to extremely high energies, and when these highly relativistic particles encounter an inhomogeneous, twisted magnetic field in the jet, significant synchrotron emission occurs into the X-ray band, which dominates the cooling process. In Fig. 3.5, it is seen that in Epoch-1, the time span of June 2000 to December 2001, we observed an anticlockwise loop (or hard-lag). This indicates that during that period particles were being accelerated to their highest speeds. We again have indications of the particles being accelerated in the internal shock outflow within the jet from epoch-2 (December 2002 to June 2003) and Epoch-3 (July 2003 to January 2007). Excluding Epoch-4 (January 2007 to December 2008), in Epoch-5, which spans over (6 December 2007$-$16 July 2012) too we found an anticlockwise loop in the spectral$-$flux representation indicating dominance of the particle acceleration mechanism. Only Epoch-4 shows a soft-lag and clockwise loop, which provides evidence of the synchrotron cooling mechanism being dominant during that particular period.

3.4 Discussion and Conclusions

In blazars, it is widely believed that variability is dominated by jet emission, which is significantly amplified by relativistic beaming. It has been believed most X-ray variability originates in a small region of the jet close to the SMBH of the blazar. The propagation of shock waves due to the fluctuations in hydromagnetically turbulent plasma in the relativistic jets can explain well the IDV and short term variability in blazars (Marscher, 1996, 2014), though some intra-day variability may be also explained by instabilities due to magnetic fields or hot spots on or above the accretion disk (Wiita, 1996).

We have performed a time series analysis of the extensively studied blazar 3C 273 in X-ray and optical/UV bands for the data taken from *XMM−Newton* over a time period of more than a decade. For our analysis, we first plotted the $0.3-10$ keV light curves of the source, shown in Fig. 3.1. The blazar pointed observation

period varied from 4.9ks for the shortest stare to 88.5ks for the longest. To study the IDV of the source in this period we have estimated the variability amplitude for all these observations and gave the results in Table 3.2. Only a few of these light curves showed even moderate flux variability, which only attained a maximum fractional rms variability of 2.6 per cent. Unsurprisingly, those observations, which were carried out for a longer period of times ($>$ 25 ks) gave more detectable variations, with $F_{var} > 1$ per cent, while that lasted lees than 25 ks showed values of F_{var} below 1 per cent with errors large enough to make them indistinguishable from null variations.

Over longer times we saw that 3C 273 is highly variable in all bands that *XMM-Newton* measured in the X-ray, UV and optical. In the Optical/UV bands, the variability amplitude decreases from UV to optical and was minimum for the V band, which is the lowest frequency measured. This can be understood simply in terms of the expectation that for synchrotron emission the more highly energetic particles cool more rapidly via the synchrotron and inverse Compton processes than do the less energetic ones. However, in the case of X-ray emission, variability in the soft band is higher than that in the hard band.

From our study of the variability relations between different bands, we see that soft and hard X-ray bands follow each other tightly, as shown in Fig. 3.4(a), indicating that their emission originates from same electron population. This doesn't answer the question as to whether the soft band follows the hard band of vice versa. The answer could in principle be found by computing the discrete correlation function (DCF) between these two bands as it would give the time difference as positive or negative lag between these emissions of corresponding bands. Unfortunately, we could not do a DCF analysis for this 3C 273 data, as they are quite poorly and irregularly sampled, so any computed DCF would be only too likely to indicate spurious correlations. The optical and UV bands too show correlation between their emissions, again indicating that these two bands are emitted from same region, but they are not correlated with X-ray band. Although for most blazars there is evidence that the X-ray emission is from the high energy tail of the synchrotron emission, which just extends the UV band to the X-ray (Jester et al., 2007), but apparently

during the period, 2000−2012 this FSRQ apparently did not follow that scenario. In the local environment of 3C 273, there might be two electron populations with two different upper limits to their Lorentz factors such that the one with higher energetic particles is emitting in both the soft and hard X-ray bands while the other one with comparatively lower energetic particles is responsible for optical/UV emission.

Anticlockwise loops in the hardness ratio vs 0.3−10 keV flux representation, which may also be referred to as the spectral index−flux representation, usually reveals a hard lag between the two emissions indicating that the soft band leads the hard band, yields that the source's hard flux increases more than soft flux with increasing total flux. This implies that during those periods particle acceleration mechanism was dominating over synchrotron mechanism for the emission observed in X-ray band.

To check the variation of flux over the observing time span we plotted the mean count rate of individual observations against modified Julian date. If one discounts some observations at the start and end of the totality of the measurements, the source shows a trend of flux decreasing (Fig. 3.3).

In this work we have studied X-ray and optical/UV variability properties of the blazar 3C 273 with observations taken by the *XMM−Newton* satellite since its launch through the year 2012. We made use of all available data in the Public *XMM−Newton* data archive. We use the Epic/pn detector data for our X-ray study and the simultaneous OM data to study the source in different optical and UV bands for learn more about the physical processes producing the radiation. Our study of this fascinating source regarding its behaviour in different energy bands over this extended period shows high flux variation in long term in all the bands, but the Optical/UV flux variability is much higher than that in X-ray bands. Optical and UV variability depends on frequency, and increases with increasing frequency, as found in previous studies. But at the same time, the source follows the opposite frequency dependency of variability in the case X-ray emissions. During this observed 12 year interval the source shows evidence of both synchrotron cooling and particle acceleration mechanisms dominating the emission during different periods. No relation

between X-ray and optical/UV emissions is found, supporting the scenario where two independent particle populations are present in its local emitting regions.

Chapter 4

Synchrotron Peak of SED & Intra-day Variability of Blazars

4.1 Introduction

Blazars emit radiation in the complete EM spectrum hence, these are among ideal objects to study their multi-wavelength spectral energy distribution (SED). The SED of blazars show two well defined broad spectral components (Mukherjee et al., 1997). Based on the location of these SED peaks, blazars are further classified into low energy peaked blazars (LBLs) and high energy peaked blazars (HBLs). In LBLs the first SED component peaks in radio to optical while the second component peaks at GeV energies, and in HBLs the first component peaks in UV/X-rays while the second component peaks at TeV energies (Padovani & Giommi, 1995). Recently blazars classification is made on synchrotron peak frequency and divided into three sub-classes i.e low synchrotron peaked (LSPs), intermediate synchrotron peaked (ISPs) and high energy peaked blazars (HSPs) (Abdo et al., 2010a). Basically LSPs and ISPs collectively belong to LBLs class.

The most puzzling flux variation in blazars are those which are happening on IDV timescales. The variability mechanisms in the blazars on IDV timescales are widely accepted that it is associated with the instabilities and irregularities in the jet flow. Hence, in order to understand IDV, it is very important to understand the fine

details of jet formation. Astronomers seeks to image jet formation using *very long baseline radio interferometry (VLBI)* but it suffers severe lack of sufficient angular resolution. An alternative method to measure fine structure of jets i.e. to search for IDV with the fastest possible time sampled light curves (LCs).

The first genuine optical IDV in blazar was reported by Miller et al. (1989). Since then extensive search for optical IDV in large number of blazars were done (e.g., Agarwal et al., 2015; Gaur et al., 2015; Gupta et al., 2008, 2012; Heidt & Wagner, 1996; Montagni et al., 2006, and references therein). In a detailed statistical analysis of optical IDV of blazars, (Gupta & Joshi, 2005) reported that if a blazar continuously observed for less than 6 hours and more than 6 hours, the chances of detecting IDV is $\sim 60-65\%$ and 80–85%, respectively. Till 2005, most of the known blazars belong to LSPs and ISPs class and so the report by Gupta & Joshi (2005) was true only for LSPs and ISPs. Till 2005, there were only 6 HBLs or HSPs (Mrk 421, Mrk 501, 1ES 1426+428, 1ES 1959+658, PKS 2155−304, 1ES 2344+514) were known, and their studies were mainly focused in X-ray and $\gamma-$ray bands (e.g., Aharonian et al., 2002, 2005; Daniel et al., 2005; Edelson et al., 2001; Giebels et al., 2002; Konopelko et al., 2003; Krawczynski et al., 2002; Massaro et al., 2004; Zhang et al., 2002, and references therein). Thanks to the revolution in $\gamma-$ray astronomy due to *HESS, MAGIC, Fermi, VERITAS,* etc. which lead to a very rapid increase in detection of new HSPs (e.g., Abdo et al., 2010b; Acero et al., 2015; Nolan et al., 2012).

The sample of newly discovered HSPs provided the opportunity to see the optical IDVs of HSPs and compare its properties with optical IDVs of LSPs. Study of optical IDV in HSPs with 62 nights of IDV observations of five HSPs (Mrk 421, 1ES 1426+428, 1ES 1553+113, 1ES 1959+650, and 1ES 2344+514) with total 144 LCs (41 in B band, 62 in R band, and 41 in B−R color) was carried out by Gaur et al. (2012a,b,c). Interestingly, they found that, 4 HSPs did not show any IDV, but only one HSP 1ES 1426+428 which had the least observations showed IDV in 6 LCs out of 8 LCs (Gaur et al., 2012b). And this result; 6 IDV LCs out of 144 LCs searched for IDV i.e $\sim 4\%$ LCs have shown IDV, explained by density inhomogeneities and bends in the bases of the jets by Kelvin–Helmholtz instabilities

(Romero et al., 1999). An alternative explanation for the observed results was also provided by the authors. As they interpreted; since in HSPs, the optical band lies below the SED peak, hence, we should see changes in the efficiency of acceleration of, and/or in the rates at which energy is radiated by, the highest energy electrons available for synchrotron emission would have a more retarded effect on optical variability in HSPs (Gaur et al., 2012c).

In LSPs, the optical band is dominated by highest energy electrons emitting synchrotron radiation and probably the X-ray emission is dominated by the comparatively lower energy electrons emitting the inverse Compton radiation, hence their X-ray variability is less pronounced than optical variability. If SED peak is really responsible for IDV properties, then we suspected that X–ray IDV LCs in LSPs should not show any IDV at all or show on rare occasions. With this motivation, in this chapter we present the X-ray IDV study of almost complete sample of 10 LSPs and 2 ISPs observed by *XMM-Newton* since its launch and we found that the LSPs show very less IDV 2 out of 50 LC i.e. 4% in X-ray bands. Our results were in total agreement with the previous finding for HSPs in optical bands.

The chapter is structured as follows: in Section 4.2 we discuss the source sample, *XMM–Newton* observations of these sources and their data analysis. Section 4.3 reports results and section 4.4 gives a discussion and conclusion on above results.

4.2 Sample Selection & Data Analysis

4.2.1 Observations and Data Reduction

XMM–Newton satellite is one of the most efficient X-ray observatory on board pointing X-ray sources, since 2000, from its day of launch (see Chapter 2 for details). Since then, the satellite's contribution in scientific community (X-ray astronomy) is enormous, and this is not different for blazar studies. *XMM-Newton* gives one of the best time resolution, and the longest pointing of any AGN. Such data are extremely useful for studying IDV of blazars.

Table 4.1: Observation log of *XMM-Newton* X-ray data for low energy peaked blazars*

Blazar Name	$\alpha_{2000.0}$	$\delta_{2000.0}$	redshift z	Blazar Class	Date of Obs. yyyy.mm.dd	Obs. ID	Window Mode[a]	GTI[b](s)
TXS 0106+612	01h09m46.3s	$+61^0 33' 30''$	0.783	LSP	2010.02.09	0652410201	FF	12034
PKS 0235+164	02h38m38.9s	$+16^0 36' 59''$	0.94	LSP	2002.02.10	0110990101	FF	16847
					2004.01.18	0206740101	SW	29671
					2004.08.02	0206740501	SW	11471
					2005.01.28	0206740701	SW	16270
PKS 0426−380	04h28m40.4s	$-37^0 56' 20''$	1.11	LSP	2012.02.11	0674330201	EFF	20745
PKS 0528+134	05h30m56.4s	$+13^0 31' 55''$	2.06	LSP	2009.09.11	0600121601	FF	25672
PKS 0537−286	05h39m54.3s	$-28^0 39' 56''$	3.104	LSP	2000.03.19	0114090101	FF	18852
					2005.03.20	0206350101	FF	80138
S5 0716+714	07h21m53.4s	$+71^0 20' 36''$	0.31	ISP	2007.09.24	0502271401	SW	71624
4C 71.07	08h41m24.3s	$+70^0 53' 42''$	2.172	LSP	2001.04.12	0112620101	FF	33480
OJ 287	08h54m48.9s	$+20^0 06' 31''$	0.3056	ISP	2005.04.12	0300480201	LW	13192
					2005.11.03	0300480301	LW	39074
					2006.11.17	0401060201	LW	44972
					2008.04.22	0502630201	LW	53568
					2011.10.15	0679380701	LW	21669
3C 279	12h56m11.1s	$-05^0 47' 22''$	0.5362	LSP	2009.01.21	0556030101	FF	25235
					2011.01.18	0651610101	SW	125487
BL Lac	22h02m43.3s	$+42^0 16' 40''$	0.0686	ISP	2007.07.10	0501660201	SW	18478
					2007.12.05	0501660301	SW	19272
					2008.01.08	0501660401	SW	22371
3C 454.3	22h53m57.7s	$+16^0 08' 54''$	0.859	LSP	2006.07.02	0401700201	SW	15972
					2007.05.23	0401700401	SW	2995
					2006.12.18	0401700501	SW	15021
					2007.05.31	0401700601	SW	28971

* Observation log for the LSP 3C 273 is given in Table 1 of our paper Kalita et al. (2015).

[a] Extended Full Frame = EFF, Full Frame = FF, Large Window = LW, Small Window = SW

[b] GTI = Good Time Interval

Our sample contains all total 12 blazars (10 LSPs and 2 ISPs). Most of the sources in the sample are well known blazars and are extensively studied with different ground and space based telescopes. But a few of them are recently come into focus of studies. *XMM–Newton* has observed all of these sources at least once in its on board period. In our study we use the EPIC/pn observations due to its higher reliability over EPIC/mos for very bright objects (Strüder et al., 2001). More details on EPIC/pn observations are discussed in Chapter 2. We excluded few observations, due to their high background brightness and few are excluded due to bad image quality. The observations we use in our analysis are listed in Table 4.1, with all important and necessary information. In the Table 4.1 we have listed as a whole, total 25 EPIC/pn observations excluding for the blazar 3C 273. For 3C 273 the observation log is given in Table 3.1 of Chapter 3.

For data reduction we followed the standard method used for *XMM–Newton* data (see Chapter 2), using the *SCIENCE ANALYSIS SOFTWARE (SAS)* version 12.0.1. Here we take the data within the energy range 0.3 keV to 10 keV (Kalita et al., 2015). Though we restrict the high energy range of data train up to 10 keV, to avoid the flaring effect (mainly coming from Sun), still we found a few light curves get affected by this. The highly affected light curves by flaring are corrected by removing the affected portion from the light curves. Pile up was found for only one source, 3C 273. We tackle this problem following the method discussed in section 2.2.3 of Chapter 2. Few observations excluding 3C 273 are slightly affected by pile up, by considering the single and double event ratios, though the data curve almost exactly follows the model curve. For these observations removing the central region of the source did not improve the ratios. Hence, we ignore pile up for those observations.

4.2.2 Excess Variance

The excess variance, σ_{XS} and fractional rms variability amplitude, F_{var}, (e.g., Edelson et al., 2002) are commonly used parameters to quantify variability. Excess variance gives the intrinsic variance of the source by removing the variance due to measurement errors in each individual flux measurement. The fractional rms vari-

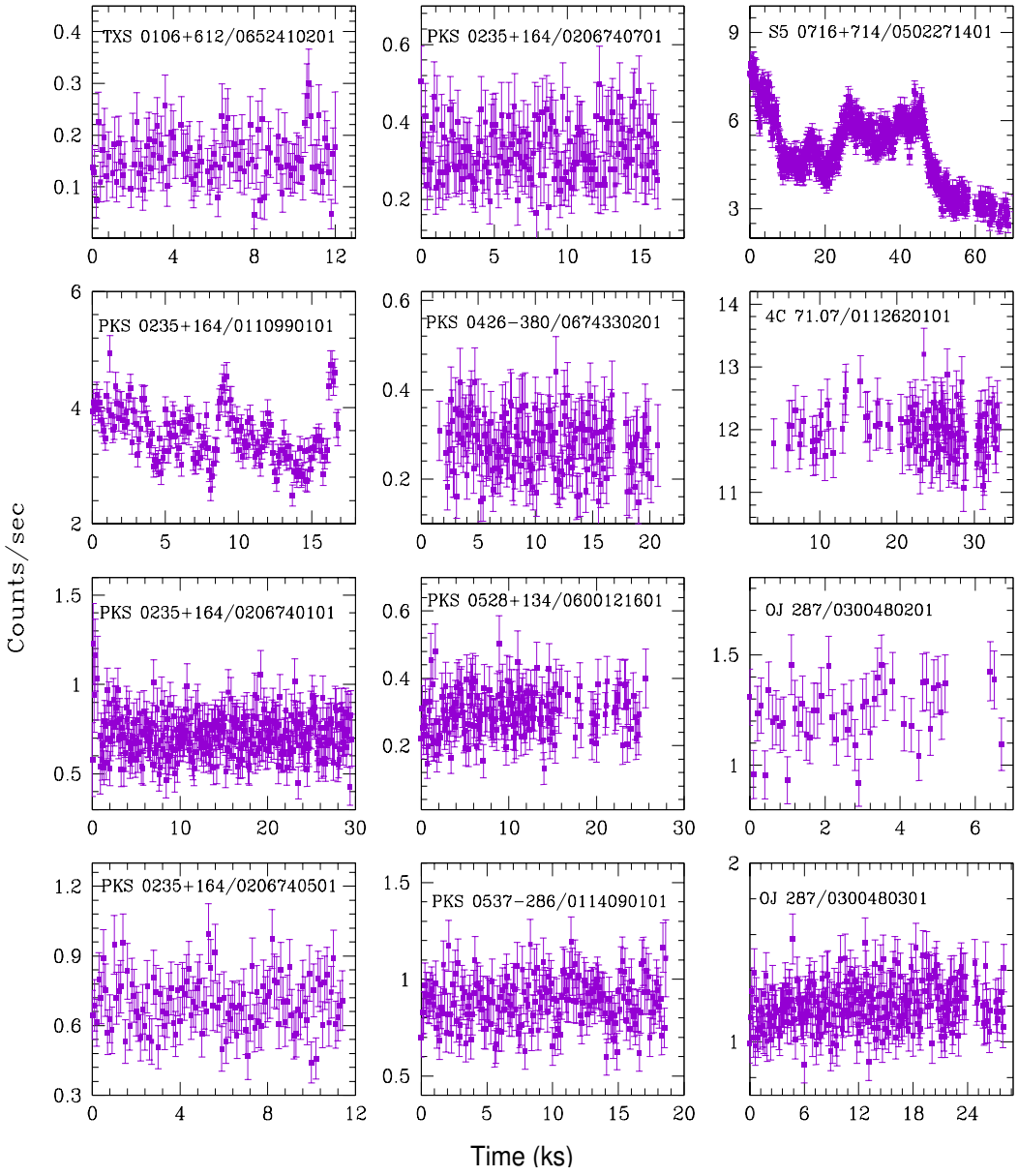

Figure 4.1: X−ray light curves of the low energy peaked blazars. In each panel blazar name / observation ID is given. Light curves are generated with 100s binning. For light curves of 3C 273 see Fig. 3.1 of Chapter 3.

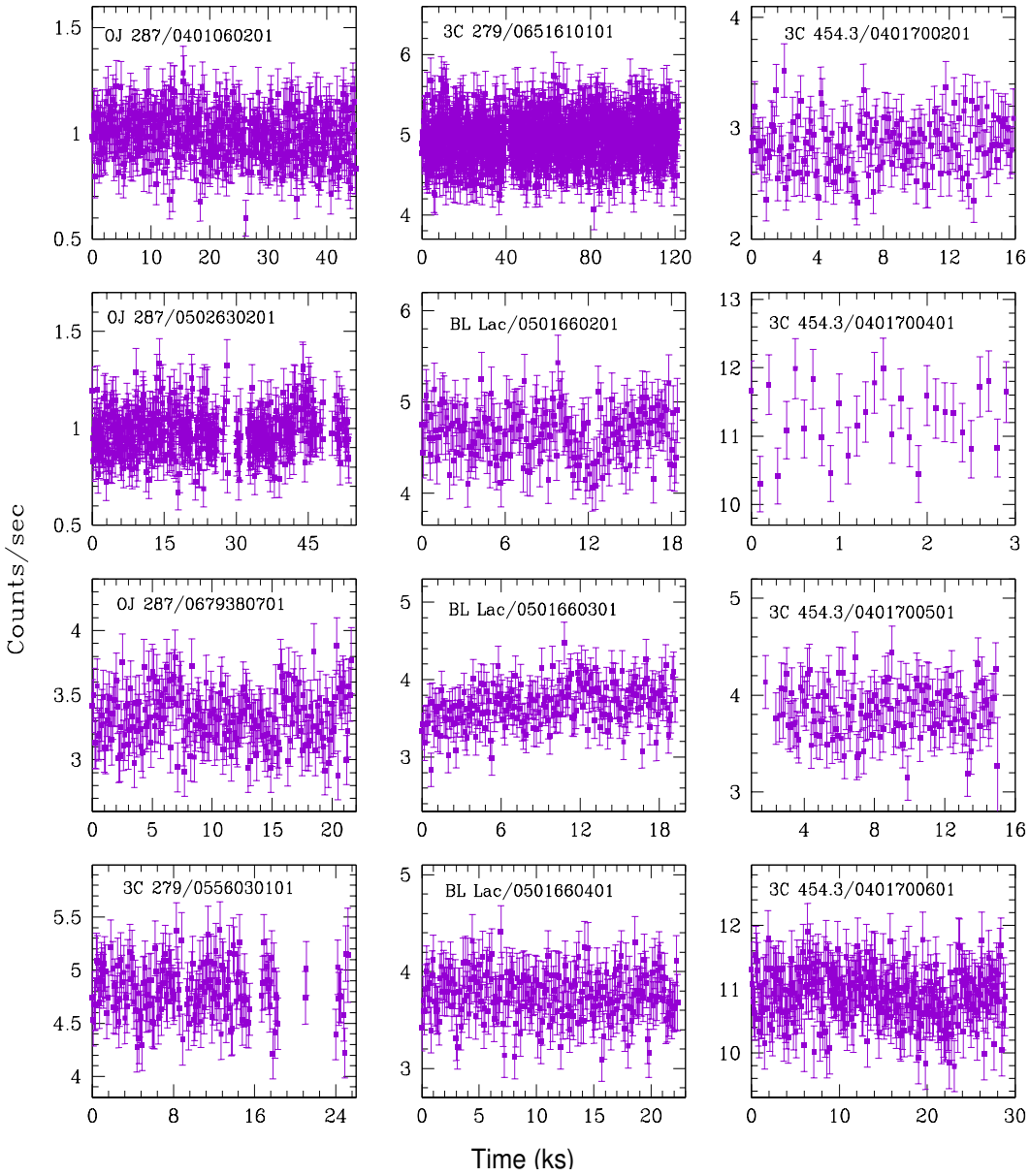

Figure 4.1: continued

ability gives the average variability amplitude with respect to the mean flux of a source. The uncertainty on F_{var} has been calculated using Vaughan et al. (2003). The detailed description of the method is discussed in section 3.2.3 of Chapter 3.

The excess variance of n number of flux measurements x_i, at times t_i, with measurement errors $\sigma_{err,i}$, is calculated as

$$\sigma_{XS}^2 = S^2 - \overline{\sigma_{err}^2}, \tag{4.1}$$

where $\overline{\sigma_{err}^2}$ is the mean square error and S^2 is sample variance

then fractional rms variability can be calculated as follows,

$$F_{var} = \sqrt{\frac{S^2 - \overline{\sigma_{err}^2}}{\bar{x}^2}} \tag{4.2}$$

Here, $\bar{x}$, represents mean count of the source.

The uncertainty on F_{var} has been calculated here, using the equation (B2) in Vaughan et al. (2003) for n number of events, which is given by

$$(F_{var})_{err} = \sqrt{\left\{\sqrt{\frac{1}{2n}}\frac{\overline{\sigma_{err}^2}}{\bar{x}^2 F_{var}}\right\}^2 + \left\{\sqrt{\frac{\overline{\sigma_{err}^2}}{n}}\frac{1}{\bar{x}}\right\}^2} \tag{4.3}$$

4.3 Results

In Table 4.2, we report the detailed analysis result of all the 50 LCs of 10 LSPs and 2 ISPs. The sample of LSPs studied here is the collection of archival observations of all LSPs with *XMM-Newton* since its launch. To avoid any type of observational bias, we have taken all the observations of LSPs inspite of their flux states which can be low-state, pre-outburst, post-outburst or outburst. The quality of detection of each observation by *XMM-Newton* is represented by its signal-to-noise ratio (SNR), listed in the last column of the Table 4.2. Different values of SNR represents different detection limit. If for particular pointing, SNR ≥ 5 is called strong detection, $3 <$ SNR < 5, is called border line detection, and < 3 is considered as not significant detection. Below we report the results of IDV detection in individual LSPs and ISPs.

4.3.1 TXS 0106+612

In *SIMBAD* this source is tagged as "possible blazar". But *MOJAVE* collaboration classified it as LSP. This source is also known as Fermi J0109+6133 (J0109+6134), or GT 0106+613. The source was first discovered by Gregory & Taylor (1981) in a radio survey of the Galactic plane. During the *XMM–Newton*'s pointing in 2010 February, the source was in flaring state detected by *Fermi Large Area Telescope (LAT)* (Vandenbroucke et al., 2010). *AGILE* and *Swift* satellites also partly covered this event in gamma-ray and X-rays bands, respectively. No significant variation was detected with *Swift* satellite in X-ray band (Vandenbroucke et al., 2010).

The single observation studied here show $F_{var} \sim 11$ % with SNR ~ 1.19 which is below detection limit. Hence, we can not claim that the source has shown genuine IDV.

4.3.2 PKS 0235+164

PKS 0235+164 is a BL Lac object and well studied in the entire EM spectrum. In optical band, the source was found to be very active and has shown IDV (Gupta et al., 2008; Romero et al., 2000). Using 25 years (1975–2000) of radio and optical data, Raiteri et al. (2001) predicted that the blazar should show a possible correlated radio and optical outburst in 2004. But the source did not show radio/optical outburst in 2004 as predicted, and significant variation in X-ray band was also not found by the help of contemporary observations carried out by VLBI, ground based optical telescopes and *XMM–Newton* (Raiteri et al., 2005). In the observing period of 2000–2005 (with *Chandra* and *XMM–Newton*), the source was found in X-ray bright state in 2002. Except in 2002, the source was in its faint state, with hard spectrum (Raiteri et al., 2006). Flaring in the source in different EM bands from radio to gamma-ray including X-ray is reported by Agudo et al. (2011), and have shown correlation in X-ray, optical, millimeter and centimeter bands.

We analyzed four pointings of *XMM-Newton* of PKS 0235+164 and found significant IDV in one in 2002 when the source was in outburst state. Other observations were done in year 2004, 2005 when the source was in faint state with SNR

less than 5 i.e. below the genuine detection limit. Hence, no significant IDV can be claimed.

4.3.3 PKS 0426-380

The blazar shows high variation in GeV band on long time scales (Neronov et al., 2015) and the source flux enhanced by a factor of 2–3 during its flaring activity. This is the most distant HE gamma-ray emitting source so far which is reported in Tanaka et al. (2013) detected by *Fermi LAT* instrument in January 2013. During this period the source was in flaring state in gamma-ray.

This source has single observation with *XMM–Newton* taken in 2010. The observation has SNR < 2 i.e. the source was below the detection limit and no genuine IDV can be reported.

4.3.4 PKS 0528+134

PKS 0528+134 is one of the most distant (z = 2.07) and bright gamma-ray blazar. The 2009 *XMM-Newton* observation of the source was part of a multi-wavelength campaign during its quiescent state (Palma et al., 2011). They reported absence of flux and spectral variability in the gamma-ray, X-ray and radio bands on IDV timescales, but found significant flux variation on IDV timescales in optical bands. They have also reported STV of moderate strength in the X-ray and radio regime on 1-2 week timescales. The simultaneous multi-wavelength SED shows that the bolometric luminosity is dominated by gamma-ray emission. As usual the low-energy SED peak lies within infrared/optical bands, and the high-energy SED hump peaks at MeV – GeV energies.

We analyzed single *XMM–Newton* observation of the blazar taken in 2009 when it was in low state and we did not find any significant detection of IDV in this particular pointing.

4.3.5 PKS 0537-286

PKS 0537-286, the high redshift (z = 3.104) FSRQ was studied by Reeves et al. (2001) with *XMM-Newton*. They reported that the source is extremely luminous in X-ray band. In their spectral study, they found that in contrast with typical AGNs, the radio to X-ray SED of the source shows dominance of X-ray power over other energy bands, which is explained by inverse Compton (IC) emission. Optical variability with different instruments and marginal X-ray variability on IDV timescale with *Swift/XRT* was reported by Bottacini et al. (2010). Sambruna et al. (2007) reported that there were no soft and hard X-ray flux variability in the source with different XRT and BAT pointings within the period 2005-2007.

We analyzed two observations for the blazar taken with *XMM-Newton* in 2000 and 2005. We did not find any significant IDV on both the occasions. No earlier information about the source flux based on other EM bands at the time of *XMM-Newton* observations is available.

4.3.6 S5 0716+714

The BL Lac S5 0716+714 is classified as ISP blazar (e.g., Giommi et al., 2008, 1999, and references therein). It has been prime interest of IDV study in optical bands and variability on other time scales has been reported frequently for the blazar (e.g., Gupta et al., 2008; Heidt & Wagner, 1996). During the *XMM-Newton* observation, the blazar S5 0716+714 was in high state with multiple flares (Zhang, 2010). The temporal and spectral variability study of the source was done in detail by Zhang (2010), where they reported that within the 74 ks exposure, the soft X-ray (0.5–0.75 keV) flux varies by a factor of ~ 4, which is much stronger as compared to the hard X-ray (3–10 keV) variations with F_{var} values 32.03$\pm$2.12 % and 7.62$\pm$1.5 %, respectively. *XMM-Newton* observations of S5 0716+714 have shown variation by more than a factor of 3 on timescale of hours (Ferrero et al., 2006). They reported that the variability amplitude in soft (0.5–0.75 keV) and hard bands (3–10 keV) are 0.40$\pm$0.03 and 0.27$\pm$0.01, respectively and synchrotron emission was dominated during the flaring activity. This is an IBL in which first hump peaks at NIR/optical region, and X-ray will fall below the peak in which hard X-ray will

have comparatively retarded effect than soft X-ray. It will cause here high amplitude variation in soft X-ray compare to hard X-ray.

We analyzed only one observation of the source with *XMM-Newton* which was taken during its high state and found strong IDV in it.

4.3.7 4C 71.07

S5 0836+710 (4C 71.07) is a high redshift FSRQ ($z = 2.172$). With *Swift* observations, X-ray variability was found on a time scale of one month in the energy range 15-150 keV (Sambruna et al., 2007). The source has shown the most luminous gamma-ray flare from any blazar till date (during Oct-Dec in 2011) in 0.1–300 GeV during its outburst state (Paliya, 2015), where IDV is also reported. Multiple X-ray and gamma-ray flares are reported by the author and it was noticed that the optical-UV flux do not show any significant variation since these bands are dominated by accretion disk emission. Different satellite's (including *NuSTAR, SWIFT*) observations of the source reported that IDV in X-ray band is absent but significant STV in different X-ray energy ranges (Akyuz et al., 2013; Ghisellini et al., 2010; Tagliaferri et al., 2015). Synchrotron hump of SED lies in sub-millimeter range (Paliya, 2015). The *XMM-Newton* observation of the source was reported by Foschini et al. (2006) for the first time to study spectral behaviour of gamma-ray loud AGN sample. The spectra of the source gives best fit with simple power law with galactic absorption.

We analyzed one observation of this source taken by *XMM-Newton* in 2001 and did not find any significant detection of IDV during this pointing.

4.3.8 OJ 287

OJ 287 is one of the most studied BL Lac object in the complete EM spectrum. It is claimed that there is binary super massive black hole (SMBH) system (Sillanpaa et al., 1988). *XMM-Newton* pointings of the source in 2005 are organized in correspondence with detected optical flare and expected optical outburst (Ciprini, 2005; Ciprini et al., 2007). The source was studied in X-ray bands during its optical bright states by Massaro et al. (2003), where they have found low X-ray flux and the SED

synchrotron peak falls in IR band. In 2005 November the source was in outburst state in optical band reported by Valtonen et al. (2006). Again an optical outburst occurred in September 2007 (Valtonen et al., 2009). The source was reported as in pre/post outburst state in optical band during October 2006 to January 2007 by Gupta et al. (2008). Another optical outburst in the object occurred during October 2007 to January 2008 (Dai et al., 2011) and During *XMM-Newton*'s pointing in 2008 the object was in post-outburst state (Villforth et al., 2010). A major optical outburst in the blazar is reported in 2012–2013 (Carnerero et al., 2015).

Here, we have analyzed 5 *XMM-Newton* pointings of the source and none of them show genuine IDV.

4.3.9 3C 273

3C 273 is the first quasar discovered (Schmidt, 1963). The source has been studied extensively in the entire EM bands. In X-ray bands the source show soft excess below $\sim$ 1-2 keV (Chernyakova et al., 2007; Page et al., 2004; Turner et al., 1985), which has been interpreted as result of combination of Seyfert and blazar like emission in this band (e.g., Pietrini & Torricelli-Ciamponi, 2008; Soldi et al., 2008). 3C 273 is very bright and nearby FSRQ, but IDV study for the source is rare in X-rays. We have searched for IDV with *XMM-Newton* pointings from 2000–2012, but no significant IDV has been found (Kalita et al., 2015). The source was in low state during the June 2003 *XMM-Newton* observation, and it reached a historically softest state in X-ray band (Chernyakova et al., 2007). *RXTE-PCA* observed the source from March 2005 to December 2011, during which several consecutive X-ray flares were observed corresponding high and low state (Esposito et al., 2015).

Since the launch of *XMM-Newton* in 2000, most extensively this blazar is pointed by *XMM-Newton*. In total we have 25 pointing of the blazar for IDV study and genuine IDV is not detected in any pointing (Kalita et al., 2015).

4.3.10 3C 279

3C 279 is one of the most studied FSRQ and classified as a LSP (Ackermann et al., 2012). A gamma-ray flare was reported by Hayashida et al. (2012), which has a optical counterpart with 10 days delay, and they reported two X-ray flares with a 90 days separation, which was not related with the gamma-ray/optical flares. The LSP shows weak variability in X-ray flux on IDV time scales with *NuSTAR* observations and shows significant spectral variation in the *Swift* satellite data reported in Hayashida et al. (2015). Chatterjee et al. (2008) studied the source in optical, X-ray, radio band and found that the variability amplitude increases with timescales and the variations in X-ray and optical band are well correlated. The source was in optical outburst state in 2007 in optical (Gupta et al., 2008), with absent of IDV but STV was reported. The source has been studied less frequently in X-ray bands. The source have shown rapid flare in X-ray bands with a duration of 20 days in April 2009 and a second X-ray flare was observed after 3 months of the first flare (Abdo et al., 2010c).

We analyzed two pointings of this source taken with *XMM-Newton* in 2009 and 2011 but did not detect any significant IDV in these observations.

4.3.11 BL Lac

The prototype of its class, BL Lac is one of the most extensively studied blazar in the entire EM spectrum. Flux variability on diverse time scales in the optical bands have been reported (Clements & Carini, 2001; Gaur et al., 2015; Massaro et al., 1998; Villata et al., 2002; Zhai & Wei, 2012). Several multi-wavelength campaigns were triggered in the past to study in detail the properties and behaviour of the object (e.g., Jorstad et al., 2010; Marscher et al., 2010; Papadakis et al., 2007; Raiteri et al., 2009, 2013; Villata et al., 2002). Using *BeppoSAX* observations genuine X-ray IDV detection in the blazar is reported (Böttcher et al., 2003; Ravasio et al., 2002, 2003). Raiteri et al. (2009) analyzed three *XMM-Newton* observations during 2007–2008 in comparatively low state and found that the SED synchrotron peak falls in the near IR region. In the low state of the blazar, the multi-frequency campaign during second half of 2008, was reported by Abdo et al. (2011). Moder-

ate IDV flux variation ($\sim$ 4–7%) was reported on hour time scales in X-ray bands with *XMM-Newton* observations during 2008 (Raiteri et al., 2010) but fast STV was detected in *Swift* X-ray data by Raiteri et al. (2010).

We analyzed three observations of this source in 2007–2008 and in any of these observations, we did not find significant IDV in any of the observation.

4.3.12 3C 454.3

3C 454.3 is a well studied FSRQ in the entire EM spectrum. The source has been flaring and showing outburst from radio to gamma-ray at different epochs (Bachev et al., 2011; Foschini et al., 2010; Fuhrmann et al., 2006; Ghisellini et al., 2007; Giommi et al., 2006; Jorstad et al., 2013; Kohler & Nalewajko, 2015; Pacciani et al., 2014; Pian et al., 2006; Sasada et al., 2014; Vercellone et al., 2008; Villata et al., 2006). In a multi-wavelength monitoring campaign of 3C 454.3 in 2008, Bonning et al. (2009) found that the source was highly variable in NIR, optical, UV and gamma-rays, but in X-ray band it was not variable. Multi-peak outburst in optical band was observed in July - August 2007 and November 2007 - February 2008, where IDV was detected in several episodes, with correlated X-ray and optical flux (Raiteri et al., 2008). Even in outburst states the SED synchrotron peak lies within the IR region (Fuhrmann et al., 2006; Giommi et al., 2006) The source was observed by *XMM-Newton* during 2006 in the post outburst phase (Raiteri et al., 2007).

We analyzed four observations of this source taken in 2006 and 2007 in the post outburst state. We did not detect any significant IDV during these observations.

4.4 Discussion and Conclusion

In this chapter we searched for X–ray IDV in the LCs of almost all the LSPs observed by *XMM–Newton* since its launch. The details of the observation log is given in Table 4.1 which gives the data of 9 LSPs and 2 ISPs with total 25 LCs. All the LCs are plotted in Fig. 4.1. There were 25 LCs of LSP 3C 273 which are already presented in Table 3.1 and Fig. 3.1 of Chapter 3. In Table 4.2, we report the results

Table 4.2: X−ray variability parameters of Low Energy Peaked Blazars

Blazar Name	Obs. Date	Obs.ID	Variance	σ_{XS}^2	F_{var} (percent)	SNR[a]	F^b ergs $cm^{-2}s^{-1}$
TXS 0106+612	2010.02.09	0652410201	0.002	0.001	11.394±6.539	1.194 *	-12.097
PKS 0235+164	2002.02.10	0110990101	0.214	0.169	11.600±0.495	24.322	-10.842
	2004.01.18	0206740101	0.012	0.001	3.173±5.321	2.752*	-11.549
	2004.08.02	0206740501	0.014	0.001	5.187±2.204	4.254**	-11.534
	2005.01.28	0206740701	0.005	0.001	9.025±3.836	1.924*	-11.880
PKS 0426−380	2012.02.11	0674330201	0.004	0.001	2.606±11.145	1.927*	-12.131
PKS 0528+134	2009.09.11	0600121601	0.004	0.001	2.952±8.832	1.973*	-11.838
PKS 0537−286	2000.03.19	0114090101	0.014	0.002	4.723±1.994	6.402	-11.622
	2005.03.20	0206350101	0.036	0.005	4.771±2.038	9.603	-11.413
S5 0716+714	2007.09.24	0502271401	1.423	1.338	23.007±0.236	12.414	-10.856
4C 71.07	2001.04.12	0112620101	0.130	0.026	1.345±0.602	60.105	-10.313
OJ 287	2005.04.12	0300480201	0.018	0.002	4.036±2.861	8.941	-11.466
	2005.11.03	0300480301	0.016	0.001	2.097±2.300	7.825	-11.477
	2006.11.17	0401060201	0.012	0.001	1.889±2.289	6.940	-11.563
	2008.04.22	0502630201	0.013	0.001	2.327±1.990	5.346	-11.566
	2011.10.15	0679380701	0.040	0.001	0.949±1.908	23.025	-11.035
3C 273	2000.06.13	0126700301	0.764	0.105	0.689±0.148	221.728	-9.899
	2000.06.15	0126700601	0.633	0.005	0.162±0.847	213.119	-9.914
	2000.06.15	0126700701	0.545	0.087	0.666±0.238	183.692	-9.926
	2000.06.17	0126700801	0.774	0.152	0.881±0.140	162.498	-9.925
	2001.06.13	0136550101	0.303	0.029	0.795±0.206	77.883	-10.237
	2001.12.16	0112770101	0.816	0.193	0.610±0.400	199.081	-9.718
	2001.12.22	0112770201	1.041	0.057	0.345±0.665	210.513	-9.733
	2002.07.07	0112770601	0.563	0.202	0.833±0.421	106.273	-9.843
	2002.12.17	0112770801	0.952	0.132	0.467±0.457	169.196	-9.686
	2003.01.05	0112770701	0.787	0.126	0.545±0.474	223.767	-9.760
	2003.01.05	0136550501	0.895	0.006	0.124±1.475	225.361	-9.770
	2003.06.18	0112771001	1.156	0.023	0.187±1.007	285.664	-9.671
	2003.07.07	0159960101	0.786	0.456	2.593±0.114	109.873	-10.159
	2003.07.08	0112770501	0.711	0.373	0.865±0.272	219.411	-9.726
	2003.12.14	0112771101	0.689	0.076	0.518±0.462	193.369	-9.848
	2004.06.30	0136550801	0.848	0.201	0.992±0.221	119.784	-9.915
	2005.07.10	0136551001	0.601	0.103	0.651±0.223	242.392	-9.875
	2007.01.12	0414190101	0.332	0.061	1.151±0.172	90.373	-10.240
	2007.06.25	0414190301	0.624	0.031	0.361±0.372	201.652	-9.909
	2007.12.08	0414190401	1.444	0.963	2.571±0.121	108.421	-9.989
	2008.12.09	0414190501	0.562	0.281	2.467±0.162	62.124	-10.241
	2009.12.20	0414190601	0.476	0.154	1.612±0.202	80.801	-10.189
	2010.12.10	0414190701	0.304	0.073	1.481±0.237	65.194	-10.313
	2011.12.12	0414190801	1.582	0.911	2.009±0.101	194.326	-9.899
	2012.07.16	0414191001	0.693	0.178	1.023±0.280	207.683	-9.960

Table 4.2 continued ...

Blazar Name	Obs. Date	Obs.ID	Variance	σ^2_{XS}	F_{var} (percent)	SNR[a]	F^b ergs $cm^{-2}s^{-1}$
3C 279	2009.01.21	0556030101	0.056	0.007	1.740±0.943	29.397	-10.888
	2011.01.18	0651610101	0.070	0.001	0.640±1.011	16.678	-10.876
BL Lac	2007.07.10	0501660201	0.069	0.008	1.931±1.055	16.703	-10.699
	2007.12.05	0501660301	0.070	0.010	2.750±0.948	21.135	-10.803
	2008.01.08	0501660401	0.057	0.005	1.939±1.156	21.436	-10.792
3C 454.3	2006.07.02	0401700201	0.054	0.007	3.001±1.226	19.269	-11.069
	2007.05.23	0401700401	0.240	0.055	2.090±1.138	27.748	-10.472
	2006.12.18	0401700501	0.062	0.003	1.437±2.003	17.443	-10.939
	2007.05.31	0401700601	0.158	0.022	1.370±0.513	34.568	-10.486

[a] Signal to noise ratio of the data, * not significant detection, ** border line detection,

[b] Log of flux in the energy range 0.3–10 keV, calculated using the tool "WebPIMMS" provided by NASA's HEASARC considering a power law spectra with galactic absorption.

of variability parameters of all 50 LCs which are calculated using excess variance. It is clear from column no. 6 of Table 4.2 that in only two pointings, one of the ISP S5 0716+714 and another one of LSP PKS 0235+164, we found significant IDV with variability amplitude of 23 and 11.6%, respectively. Since, S5 0716+714 is observed in outburst state and is an ISP, it could be expected that the synchrotron peak of this blazar reaches up to soft X-ray regime. Similarly, PKS 0235+164 is also found to shift its peak up to soft X-ray region in its outburst state (Madejski et al., 1996). Hence, in these two occasions, we expect to get the variability in X-ray band. In other pointings, we did not find any significant variability. Most of the sources listed in Table 4.1 are well known LSPs and are extensively monitored in optical bands and they have shown high duty cycles in optical bands up to $\sim$ 70–80% (Agarwal et al., 2015; Gaur et al., 2015; Goyal et al., 2012; Gupta et al., 2008, 2012).

Similarly, IDV of HSPs in X-ray band is well studied and are highly variable in these bands (e.g., Gaur et al., 2010; Kalita et al., 2015; Lachowicz et al., 2009) but not very extensively studied in optical bands. Till now, we put an extensive effort to observe the optical IDV of HSPs and found these sources to be less variable in these bands.

The difference in the multi-frequency spectral properties of HSPs and LSPs requires a systematic change of intrinsic physical parameters such as magnetic field,

jet size, maximum electron energy and it is investigated by Sambruna et al. (1996) that the change is in the sense that HSPs have higher magnetic fields/electron energies and smaller sizes as compared to LSPs. All the above factors lead to the difference in the cut off energies of LSPs and HSPs and hence have a more retarded effect on the X-ray variability of LSPs. ISPs lies in between these two classes and is difficult to mark the exact boundaries as it depends on the state of the source i.e whether it is in quiescent/outburst state. The variations in the acceleration efficiency of the relativistic electrons near the synchrotron hump could arise from the changes in the local number density of the most energetic electrons or the strength of the localized magnetic fields. Near the peak of the SED, acceleration processes dominates and produces the higher energy electrons while the lower energy electrons are available for the emission below the SED peaks. Below the SED peak, probably cooling processes dominate which involve mainly inverse Compton for LSPs in general (Joshi et al., 2014). Since, the most excepted model for the intra-day variability involves magneto-hydrodynamic instabilities, presence of turbulence behind or in the vicinity of the shock (Marscher et al., 1992) hence one can expect that the X-ray variability would be more pronounced for HSPs as compared to LSPs which is confirmed from our observations. These differences can lead to the apparent dichotomy between these two classes of blazars however we need statistically more observations to firmly conclude our findings.

Chapter 5

Origin of X-rays in Low State of 3C 273: Evidence of Inverse Compton Emission

5.1 Introduction

The first discovered quasar, 3C 273 (Schmidt 1963), is classified as a Flat Spectrum Radio Quasar (FSRQ) and thus belongs to the violently variable AGN class of blazars. This quasar is nearby ($z = 0.158339$) and luminous in all frequencies. It shows most of the common properties of blazars, including high polarization and large flux variability at optical wavebands, strong radio emission, and a relativistically out-flowing nonthermal radio jet oriented close to our line of sight. Radio through infrared/optical emissions are dominated by synchrotron emission from the jet (Robson et al., 1993; Türler et al., 2000). Moreover, the object contains a radio core which has been found to show superluminal motions (Jorstad et al., 2005, 2001).

X-ray emission of 3C 273 possesses some peculiar features, which are generally not common in blazars. A variable soft component below 2 keV is found in the source in almost all satellite observations (e.g. Chernyakova et al., 2007; Courvoisier et al., 1987; Leach et al., 1995; Page et al., 2004; Pietrini & Torricelli-

Ciamponi, 2008; Türler et al., 2006; Turner et al., 1985, and references therein) which is generally fitted with multiple black body component or comptonization model (Page et al., 2004) or even with a steep power law. The presence of a Fe K_α emission line near 6.4 keV has been detected from time to time by several authors (Page et al., 2004; Turner et al., 1990; Yaqoob & Serlemitsos, 2000). A large optical/ultraviolet bump (Big Blue Bump – BBB), which can be explained as result of accretion disk emission (Paltani et al., 1998), is another interesting feature generally found in this source. Surprisingly, all these features are found in Seyfert galaxies, which are closer and weaker AGN as compared to blazars; moreover, the angle between the jet direction (when present) and our line of sight is much larger for Seyferts than for blazars (Urry & Padovani, 1995). The presence of both a BBB and soft excess in the source indicates a possible link between these two emission phenomena. Regarding all these characteristics it can be said that X-ray emission from 3C 273 is a combination of blazar-like and Seyfert-like components. To explore these questions and for a better understanding of the physics, we need to study the X-ray spectra of 3C 273 in different states.

3C 273 was first detected in the 1–10 keV X-ray band by Bowyer et al. (1970) and since then it has been observed and studied extensively with all the major X-ray satellites. During bright states, the 2–10 keV spectra were fit by a power-law with spectral index of around 1.5, while the 10–25 keV band could be fit with a power-law of spectral index 0.91 using *EXOSAT* observations (Turner et al., 1985). This confirms that the high energy X-ray spectrum of 3C 273 has a hard tail when the source is bright (Turner et al., 1985). With 5 years of *EXOSAT* and *Ginga* observations, Turner et al. (1990) reported that the X-ray spectrum is well described by a power law with Galactic absorption and that the power-law spectral index is not correlated to the 2–10 keV flux. The absence of correlation between photon index and flux was also reported by Page et al. (2004). It was also discovered that this power-law spectrum may extend up to 200 keV (0.1–200 keV) using *BeppoSAX* data (Haardt et al., 1998), with a spectral index of $\Gamma = 1.53 - 1.6$. The occasional appearance of a weak iron line, either narrow or broad, has been found at a energy of nearly 6.4 keV (Haardt et al., 1998; Page et al., 2004; Yaqoob & Serlemitsos, 2000). In a few cases, a more complicated model, involving a cold reflector in addition to

power-law and black body components, such as *PEXRAV*, seemed to be required, as when a deviation from power law spectra below 1 keV and above 10 keV was reported with *BeppoSAX* observations during 1996–2001 (Grandi & Palumbo, 2004). Kataoka et al. (2002) found that the source flux varies by a factor of 4 over a period of four years and the hard power-law spectrum is not due to the contribution of Seyfert-like beamed emission but likely arose from inverse Compton scattering emitted by the jet. So, generally it can be said that the harder continuum in the energy range 2–10 keV of 3C 273 is well described by an absorbed power law with a differential spectral index.

Specific features in the X-ray spectra of 3C 273, i.e., the fluorescent Fe K_α transition line, the absorption edge and the soft excess, are found to be variable in different observations taken at different times (Haardt et al., 1998), and so these variations were interpreted as being related to the state of the source. During the source low state the contributions from thermal and non-thermal emission become comparable, hence the X-ray features become prominent. At higher luminosity states, emission from the relativistic jet dominates any thermal and/or reprocessed emission related to the disc, and those features are diluted. Clearly the X-ray spectra of 3C 273 are not as simple as those of other blazars. Several emission components contribute to the X-ray spectra, resulting in appearance of distinct features which depend on the different states of the source.

Unlike lower frequency emissions, the X-rays cannot be fully explained by the synchrotron emission mechanism, but there is debate as to whether the excess predominantly results from inverse Compton scattering of low energy seed photons by the relativistic electrons in the jet or by the hot corona above the accretion disc (Haardt & Maraschi, 1991). There are no strong results that fully support either explanation. A common origin of the UV and X-ray emissions was argued for by Walter & Courvoisier (1992). However, later observations were unable to detect a connection between these two bands (Chernyakova et al., 2007; Soldi et al., 2008), which makes the contributions of different X-ray emission mechanisms to the flux quite uncertain.

5.1 Introduction

Observations made by *XMM-Newton* have been used to study the spectral behaviour of 3C 273 in different epochs. The observations made during 2000–2003 were studied by Page et al. (2004) who found that the spectra below 2 keV was dominated by a strong soft excess which can be adequately fitted by either multiple blackbodies or a Comptonization model and the 3–10 keV spectra were well fitted by a power law model with an occasional weak broad Fe emission line (EW $\sim$ 56 eV). Spectral study of the source during 2000–2004 with *XMM–Newton* revealed an increase of the thermal component as compared to the synchrotron component (producing a softening of the hard spectral index) where the 0.4–10 keV spectra were described by broken power-law model (Foschini et al., 2006). Courvoisier et al. (2003) used only the spectra above 3 keV, avoiding the soft excess, to study the cross calibration between different satellite's instruments, where all the spectra were fitted with a simple power-law model. The presence of a quasi-periodicity (QPO) of period 3.3 ks in 3C 273 (during Obs ID 1267003013 in 2000) was claimed (Espaillat et al., 2008) but this was later deemed to be not significant by González-Martín & Vaughan (2012).

The broadband spectrum (0.2–100 keV) of the object during 2003 to 2005 with quasi-simultaneous *INTEGRAL* and *XMM–Newton* observations were well described by a soft cut-off power law plus a hard power law (Chernyakova et al., 2007). They found that replacement of the soft cut-off power law with either a black body model or by a disk reflection model did not improve the fit. They also reported the source was evolving toward softer X-ray emission over the last 30 years. Energy dependent variability of 3C 273 was reported by Soldi et al. (2008) in their multi-wavelength study of the source. They proposed the presence of two X-ray emitting components, where they argued that the hard X-ray emission is not related to the acceleration of electrons by the shocks in the jet, but rather is associated with the long term optical variation and emitted through inverse Compton emission (synchrotron self Compton – SSC and/or external Compton – EC). Multi-wavelength variability study of the source using 12 years of *XMM-Newton* observations (2000–2012), found that the source was highly variable in all bands from optical to X-rays on long time scales but that there was no evidence for intraday variability in the individual light curves in X-rays (Kalita et al., 2015). We also noticed that the amount

of X-ray variability disagreed with the frequency dependent variability that is generally found in blazars. The presence of both long term variability and the lack of frequency dependent variability in the X-ray bands of 3C 273 leads us to expect interesting spectral evolution of the source during the observational period.

The quasi-continuous observations during 2005–2012 made by *RXTE-PCA* provide us with the necessary information about the emission state of the source in X-ray band during that period (Esposito et al., 2015). Gathering all this information we can say that all the *XMM-Newton* pointings included in this study were taken during low states of 3C 273 except for the observation taken in December 2007, when an X-ray flare was detected (Esposito et al., 2015).

Only the observations taken during 2000 to 2005 by *XMM-Newton* (discussed above) were extensively used in spectral study of the source. The observations made after 2005 have not been used to provide a more complete sample for spectral studies. Moreover, most of the previous X-ray spectral studies of 3C 273 were carried out for relatively short periods (a few years). In this work we have undertaken analyses of 15 years of observations, which makes this the longest data set available from *XMM-Newton* employed to study the spectral evolution of the source. We have analyzed a total 20 X-ray epochs from 2000 to 2015, with 17 of those accompanied by truly simultaneous UV/optical observations. The observations made during 2013 to 2015 are presented for the first time in this work and all of the data has benefited from being analyzed in a uniform fashion with updated pipelines.

An important finding of this work, that the origins of X-ray and UV/optical emissions from 3C 273 are closely related, which we interpret through inverse Compton process (see Section 5.4.2 and 5.5 for details), follows previous research by Walter & Courvoisier (1992) and Chernyakova et al. (2007). In the former paper, the authors found an correlation between X-ray and UV bands, using 5 years of quasi-simultaneous UV and X-ray observations (with *EXOSAT* and *Ginga*) and this supported the Comptonization model. However, the latter work could not find the presence of any relation between these bands with simultaneous *XMM-Newton* observations in the period 2003–2005. This produced a puzzle for our understand-

Table 5.1: Log of *XMM-Newton* on-axis observations of 3C 273 having data length $\geq$ 8 ks

Date of Obs. dd.mm.yyyy	Obs.ID	Revolution	Window Mode	GTI (ks)	Pile up	Filter	μ (counts s^{-1})	OM filter[1]	Exposures[2]
13.06.2000	0126700301	94	Small	64.9	No	MEDIUM	47.04±0.81	1,2,3,4,5,6	29
15.06.2000	0126700601	95	Small	29.6	No	MEDIUM	45.41±0.80	4,5,6	15
15.06.2000	0126700701	95	Small	29.9	No	MEDIUM	44.16±0.80	1,2,3	15
17.06.2000	0126700801	96	Small	60.1	No	MEDIUM	44.26±0.79	1,2,3,4,5,6	30
13.06.2001	0136550101	277	Small	88.5	Moderate	MEDIUM	21.58±0.58	1,2,3,4,5,6	12
05.01.2003	0136550501	563	Small	8.4	No	MEDIUM	63.22±0.94	2,3	2
07.07.2003	0159960101	655	Small	58.0	Weak	THIN1	26.05±0.57	1,3,4,5,6	5
08.07.2003	0112770501	655	Small	8.0	No	THIN1	70.66±1.04	Nil	Nil
14.12.2003	0112771101	735	Small	8.3	No	THIN1	53.34±0.87	Nil	Nil
30.06.2004	0136550801	835	Small	19.7	No	MEDIUM	45.27±0.81	1,2,3,4,5,6	6
10.07.2005	0136551001	1023	Small	27.5	No	MEDIUM	49.68±0.84	1,2,3,4,5,6	6
12.01.2007	0414190101	1299	Small	76.5	Moderate	MEDIUM	21.42±0.52	1,2,3,4,5,6	9
25.06.2007	0414190301	1381	Small	31.9	No	MEDIUM	45.90±0.80	1,2,3,4,5,6	8
08.12.2007	0414190401	1465	Small	35.3	Weak	MEDIUM	38.16±0.69	1,2,3,4,5,6	6
09.12.2008	0414190501	1649	Small	40.4	Weak	THIN1	21.57±0.52	1,2,3,4,5,6	6
20.12.2009	0414190601	1837	Small	31.3	Weak	THIN1	24.36±0.57	Nil	Nil
10.12.2010	0414190701	2015	Small	35.8	Weak	THIN1	18.29±0.48	1,2,3,4,5,6	6
12.12.2011	0414190801	2199	Small	42.8	No	THIN1	47.48±0.82	1,2,3,4,5,6	6
16.07.2012	0414191001	2308	Small	25.5	No	THIN1	41.22±0.93	4,5,6	3
13.07.2015	0414191101	2856	Small	70.8	Moderate	THIN1	21.92±0.56	1,2,3,4,5,6	6

μ = mean count rate in the energy range 0.3–10 keV; GTI = Good Time Interval,

[1] 1 = *UVW2*, 2 = *UVM2*, 3 = *UVW1*, 4 = *U*, 5 =*B*, 6 = *V*,

[2] Total number of exposures combining all six filters

ing about the physical mechanisms responsible for X-ray emission in the FSRQ and led us to investigate how the UV-X-ray connection varies in the source on different timescales. We obtain an excellent correlation between these bands, which is presented in Section 5.4 and discussed in the following section. Crucially, this correlation seems to be present only when 3C 273 was in low state. During a flaring state the X-ray and UV/optical emissions behave differently and do not follow the relation found in low states. How these bands are connected in high states is still an open question, and will require further observations to answer.

In this chapter we present all the simultaneous observations of 3C 273 with the EPIC-pn and Optical Monitor (OM) instruments on board the *XMM–Newton* satellite. Considering the large number and high quality EPIC-pn spectra over a very long time span (mid-2000 through mid-2015) we can productively study the spectral evolution over these years. Flux variations of the hard component of 3C 273 (here "hard" is defined as 2.5–10 keV, following Pietrini & Torricelli-Ciamponi (2008) allow us to investigate correlations between different spectral parameters. We have also studied the relation of this hard continuum with UV emission using simultaneous UV and X-ray observations for a better understanding of the long term behaviour of the object. The chapter is organized as follows: *XMM-Newton* observations of 3C 273 taken with EPIC-pn and OM are discussed in section 5.2. Since the details about our spectral analysis procedure are described in chapter 2, here we will only discuss the individual observation related issues. In section 5.3 the spectral fitting techniques with the package *XSPEC* and the model used to fit all the spectra are discussed. In section 5.4 we give our results on spectral evolution of the source, a discussion follows in section 5.5, and finally the chapter is concluded in section 5.6.

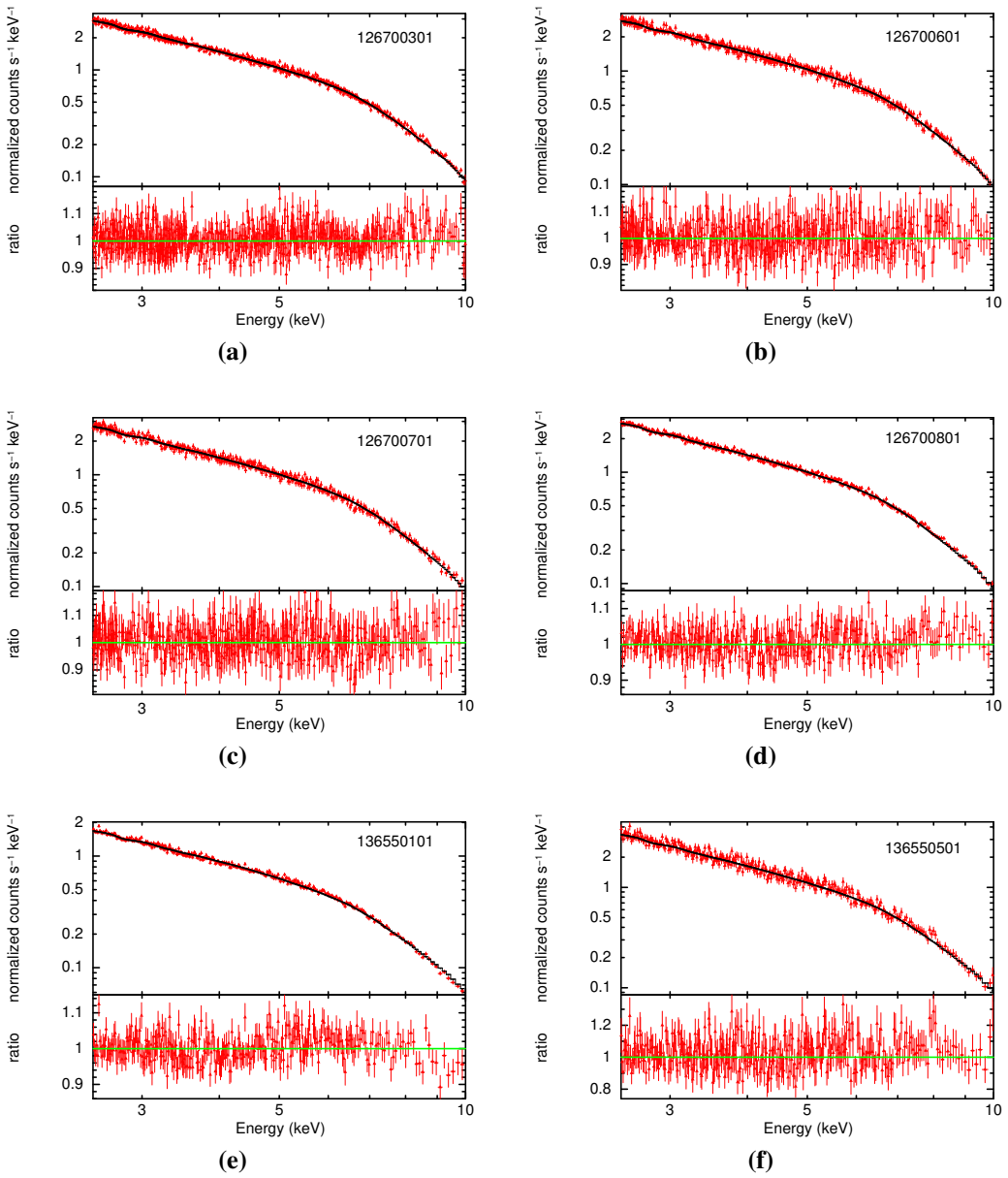

Figure 5.1: The 2.5–10 keV X-ray spectra of 3C 273 as observed by the EPIC-pn camera on board *XMM-Newton* from 2000–2015. The fits are to absorbed power-laws using a Galactic neutral hydrogen column density fixed at $N_H = 1.8 \times 10^{-20}$ cm^{-2}, with the lower panels showing the data-to-model ratios. The relevant parameters are given in Table 5.1

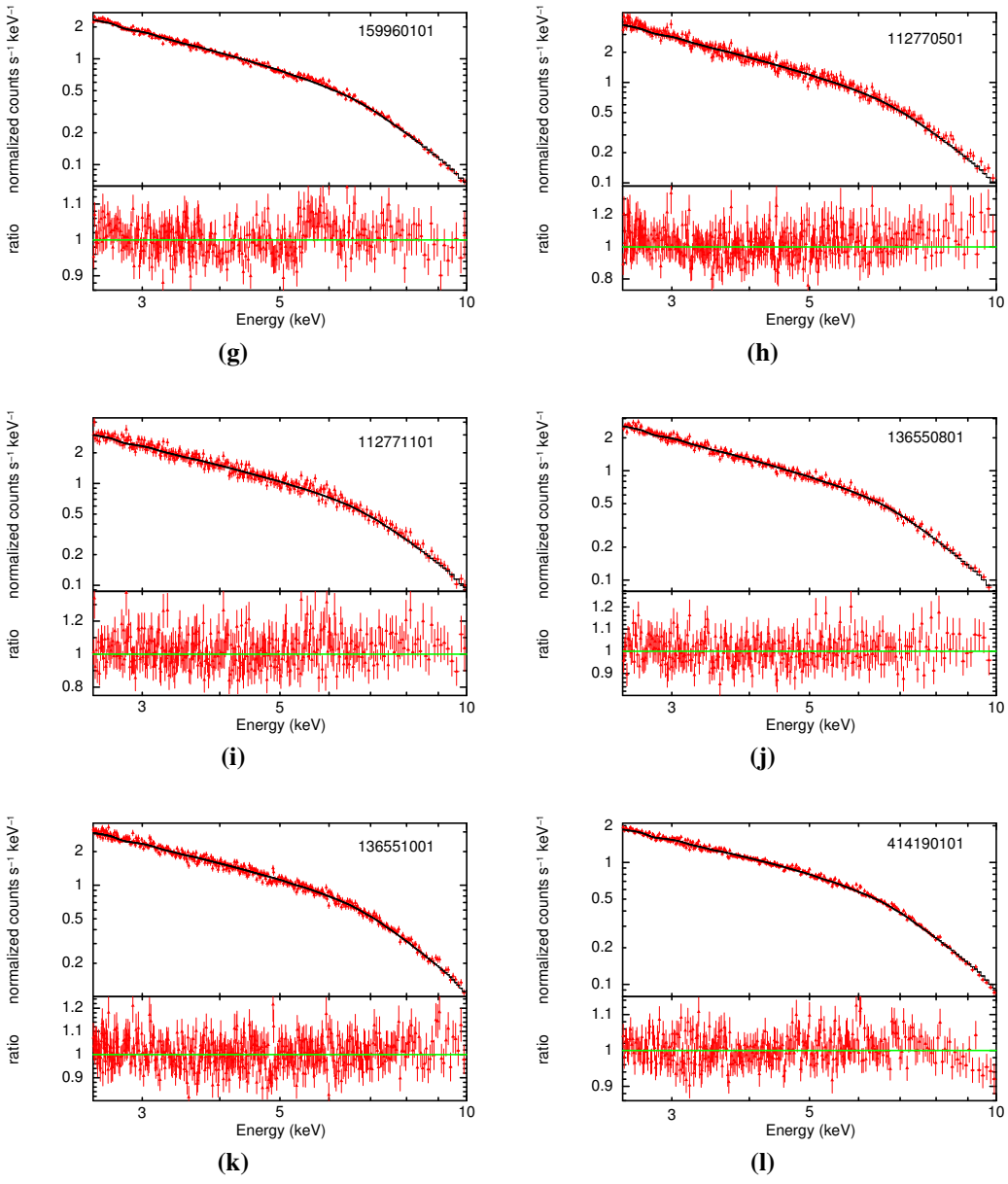

Figure 5.1: continued

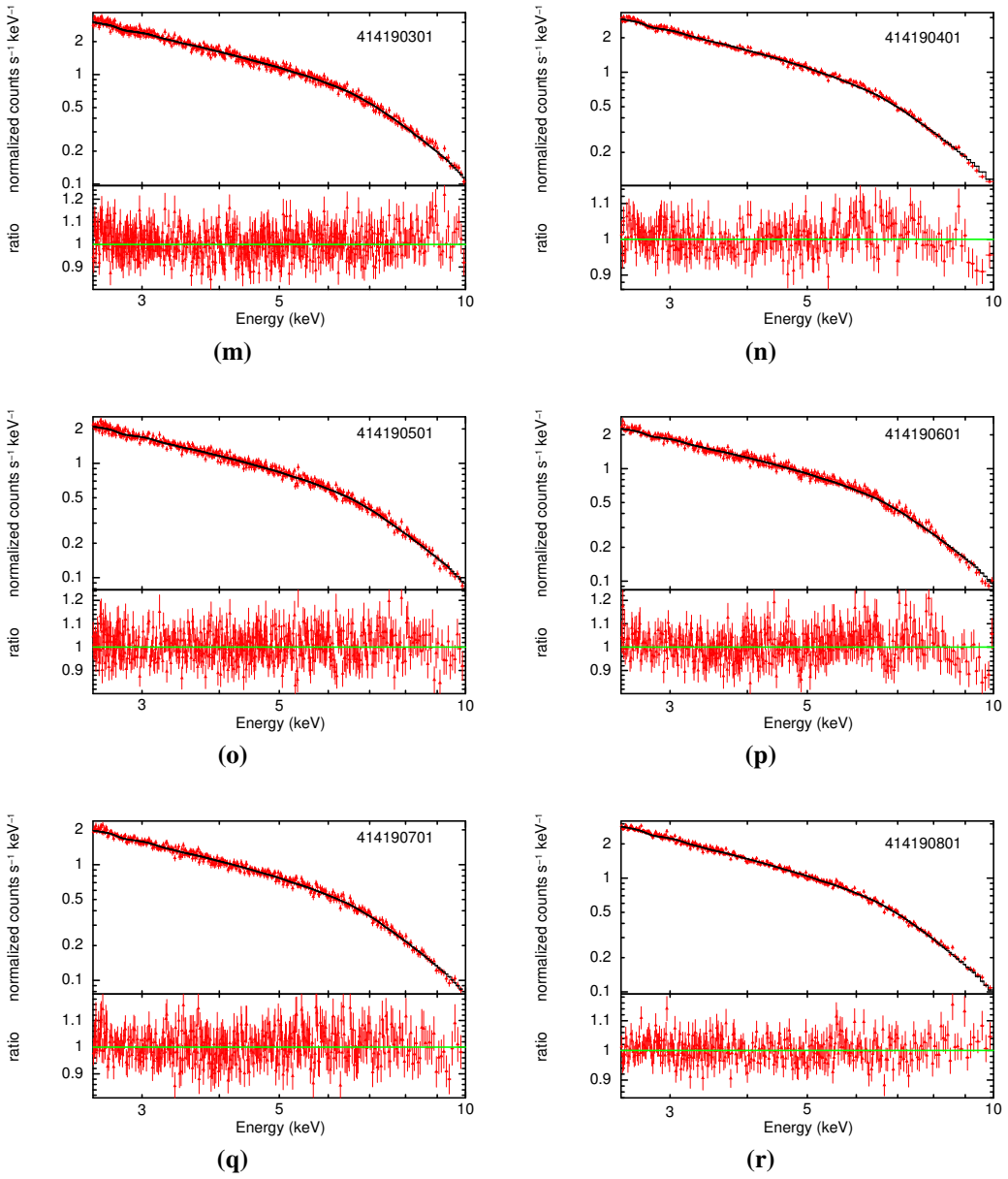

(m) (n) (o) (p) (q) (r)

Figure 5.1: continued

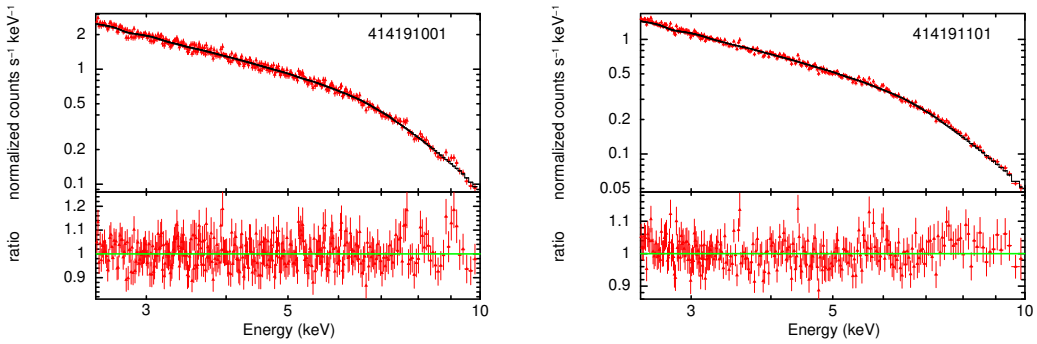

(s) (t)

Figure 5.1: continued

5.2 XMM–Newton Observations

5.2.1 EPIC-pn Data and X-ray Spectral Analysis

3C 273 is one of the sources used to calibrate *XMM-Newton* and has been frequently observed by the satellite from the beginning of the observatory to till date. Hence, *XMM-Newton*'s data archive is one of the richest X-ray data sets available for this source. Here, we have undertaken the spectral study of 15 years of observations from June 2000 to July 2015, listed in Table 5.1, for which the photometry was already discussed in Chapter 2 and (Kalita et al., 2015).

The Observational Data Files (ODFs) are collected from the online *XMM-Newton* Science Archive. As mentioned in Chapter 2 we applied two constrains on the data for spectral study: 1) The data lengths should be $\geq$ 8 ks (to produce statistically significant results) and 2) only on-axis observations will be included in this study. The first constraint excludes a total 6 observations from the list and the second constraint excludes the observations made during 2013 which were taken at an offset angle of 8.38′. Moreover, the 2013 observations are highly affected by proton flaring. These constraints leave us with total number of 20 observations for our study. These observations give a signal-to-noise ratio value of $\sim$146 on average, with lower and upper limits of 62 and 242, respectively. All these on-axis observations are taken with the THIN and MEDIUM filters. Eight observations out of 20 are weakly/moderately

affected by pile-up problems as noted here in Table 5.1. Pile-up from these observations are removed following the method discussed in Chapter 2.

5.2.2 Optical Monitor (OM) Data

As mentioned earlier, the OM provides coverage between 170 to 650 nm in the optical/UV range. Out of a total of 20 observations we use in this work, 17 contain simultaneous optical data (see Table 5.1). The detail about the OM telescope and data processing of OM Optical/UV filters are discussed in Chapter 2. The count rate for respective filters are collected from the final source list result files. If we assume that the X-ray power law emission is an extrapolation of low energy photons (optical/UV) via Comptonization processes then the high energy power law cutoff will represent the maximum energy range of the emitted X-ray photons. For study of correlations between bands we consider the highest frequency UV filter, UVW2 (6.2 eV), through which simultaneous X-ray/UV observations were taken 14 times by *XMM-Newton*. Then the count rates are converted to flux based on white dwarf standard star observations (using method 1 as instructed on the SAS watchout page[1]). The resulting fluxes for this filter are provided in Table 5.2.

5.3 Spectral Fitting with *XSPEC*

For the spectral analysis we have used the X-ray spectral fitting package *XSPEC* version 12.8.2 provided by *HEASARC, NASA/GSFC*. The goodness of fit for the spectral fitting process is determined by the reduced χ^2 value, since the number of data points in each spectra are large enough to satisfy the condition for use of χ^2 statistics. We have performed spectral fitting for all the spectra in the energy range 2.5–10 keV, since our aim is to study the harder continuum of the source. The lower limit of 2.5 keV is employed to avoid any contribution from the complicated soft excess emission which is influenced by galactic and other soft X-ray emissions found in the object. In all our fitting analyses we have considered X-ray absorption due to Galactic neutral hydrogen towards the observer. Unless stated otherwise, all the errors quoted are 2σ (90 %). We report only those fits with reduced χ^2_r less than

[1] http://www.cosmos.esa.int/web/xmm-newton/sas-watchout-uvflux

Table 5.2: Optical Monitor UVW2 filter log.

Date of obs. (yyyy.mm.dd)	Obs. ID	F^1_{uvw2} (ergs cm^{-2} s^{-1})	F^2_{err} (ergs cm^{-2} s^{-1})
13.06.2000	126700301	3.3387364e-10	1.2408036e-13
15.06.2000	126700601	—	—
15.06.2000	126700701	3.3251290e-10	1.3254516e-13
17.06.2000	126700801	3.3222661e-10	1.2548698e-13
13.06.2001	136550101	4.0486519e-10	1.4448513e-13
07.07.2003	159960101	3.8417051e-10	1.7985725e-13
30.06.2004	136550801	3.1228535e-10	2.1105259e-13
10.07.2005	136551001	3.6505119e-10	2.9180965e-13
12.01.2007	414190101	3.2662444e-10	1.6241971e-13
25.06.2007	414190301	2.8009823e-10	1.9517117e-13
08.12.2007	414190401	3.9972460e-10	2.9177285e-13
09.12.2008	414190501	3.1919197e-10	2.6378211e-13
20.12.2009	414190601	—	—
10.12.2010	414190701	3.3076551e-10	2.4767070e-13
12.12.2011	414190801	3.4609663e-10	2.4635401e-13
16.07.2012	414191001	—	—
13.07.2015	414191101	2.2965041e-10	1.0593299e-12

[1] UV flux of UVW2 filter, [2] Corresponding error in flux
* — indicates that either there were no OM observations or the UVW2 exposure is absent.)

1.5. For any added spectral component, the improvement of the fit is determined by both the change in the reduced χ^2_r value, $\Delta\chi^2$ value and the F-test value. We use the in-built tool in the XSPEC package to compute $\Delta\chi^2$ which gives the improvement of the spectral fitting after adding an new model component to the first model used for fitting the spectra. It calculates the F-statistic and its probability from the two χ^2 values computed from those two different fits.

5.3.1 X-ray Spectra: Single Power-law Model

We first fit the spectra with a simple power-law absorbed by the Galactic hydrogen column along the line of sight to 3C 273. For all the fits we fixed the neutral H column density value at $N_H = 1.8 \times 10^{-20}$ cm^{-2} (Dickey & Lockman, 1990). Out of 20 spectra, 13 are nicely fit by power-laws alone, with statistically excellent reduced χ^2 values. Also, the deviation of the data/model ratio from unity lies within a 20% error limit for those fits. Figures 5.1 contain all the spectra fitted with an absorbed power law. The power-law spectral indices, Γ, have a minimum slope of 1.35 in January 2007 and a maximum slope 1.79 in July 2003 and thus show a range of $\Delta\Gamma = 0.44$. For those observations affected by the pile-up problem, a break appears in the spectra at or above 8 keV, which can be seen most easily from the data/model ratio plots. These "breaks" occur due to the exclusion of the central source region to remove the pile-up effect from the light curves. Though we have taken care of the flux loss and energy distortion caused by the pile-up correction by regenerating the redistribution matrix as mentioned earlier, it seems the distortion at the high energy end of the spectrum cannot be overcome fully. Despite the breaks near the tails of these spectra, power-laws still give statistically acceptable fits, albeit typically with slightly higher χ^2_r value as compared to the rest (see Table 5.3) with totally reasonable parameters. The X-ray fluxes are calculated within the energy range 2.5–10 keV using a simple power law model.

5.3.2 Fe K$_\alpha$ Emission Line

The presence of a fluorescence Fe Kα line near its rest energy of 6.4 keV has been detected in 3C 273 from time to time with different X-ray observations. The iron

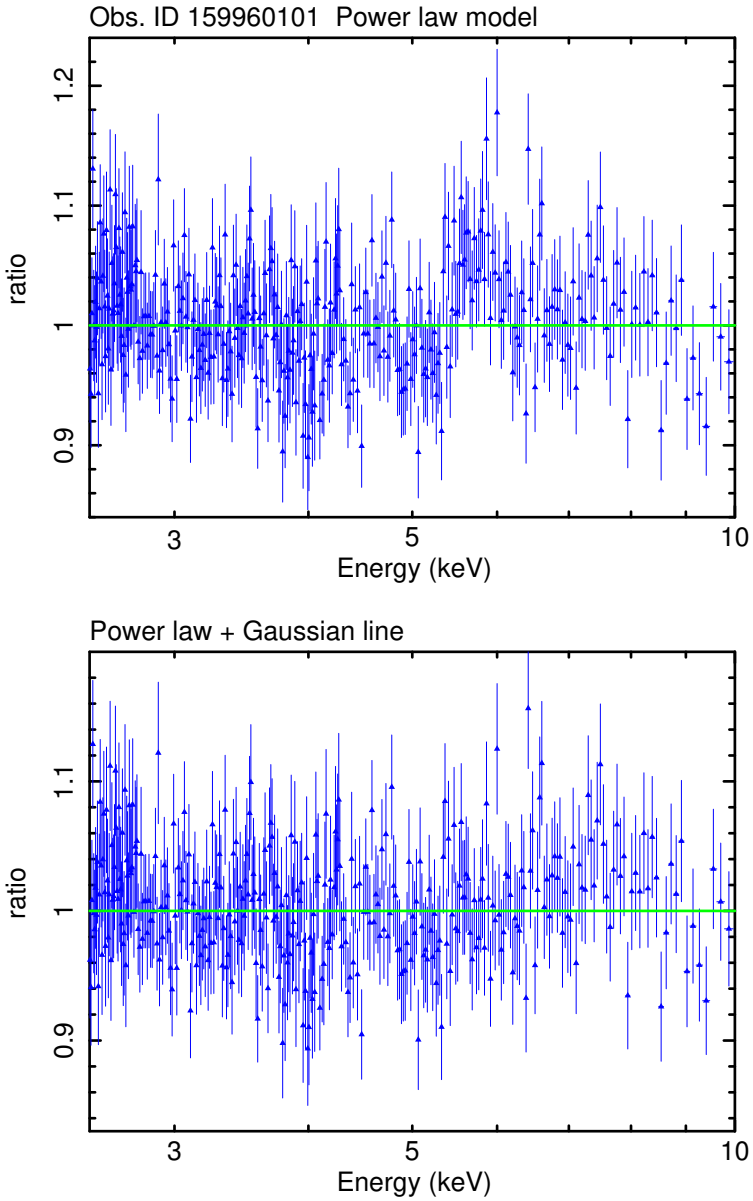

Figure 5.2: Data to model ratios of the Observation 0159960101. **Top:** A simple power law fit to the spectrum with galactic absorption. At near 6 keV the residual shows a bump indicating the presence of an iron line. **Bottom:** The bump disappears from the residuals after adding a Gaussian line to the power law spectra; addition of a Gaussian line improves the fit by changing χ^2_r value from 1.13 to 1.05 ($\Delta\ \chi^2$ = 48/3 degrees of freedom).

Table 5.3: The parameters of 2.5–10 keV X-ray continuum extracted by fitting simple power-laws with fixed galactic absorption, $N_H = 1.8 \times 10^{-20}$ cm^{-2}

Date of obs. (yyyy.mm.dd)	Obs. ID	Γ^a	N^b ($\times 10^{-02}$)	χ^2/DOF	χ^2_r	Null--hypothesis	F^c (erg cm^{-2} s^{-1})
13.06.2000	126700301*	$1.64^{+0.01}_{-0.01}$	$1.75^{+0.02}_{-0.02}$	482.81/469	1.03	3.20e-01	7.06e-11
15.06.2000	126700601	$1.59^{+0.01}_{-0.01}$	$1.61^{+0.03}_{-0.03}$	451.04/425	1.06	1.84e-01	7.03e-11
15.06.2000	126700701	$1.60^{+0.01}_{-0.01}$	$1.58^{+0.03}_{-0.03}$	444.78/421	1.06	2.04e-01	6.83e-11
17.06.2000	126700801	$1.61^{+0.01}_{-0.01}$	$1.63^{+0.02}_{-0.02}$	696.55/693	1.01	2.26e-02	6.81e-11
13.06.2001	136550101*	$1.54^{+0.01}_{-0.01}$	$2.10^{+0.03}_{-0.03}$	709.14/693	1.02	2.26e-02	9.84e-11
05.01.2003	136550501	$1.77^{+0.02}_{-0.02}$	$2.29^{+0.07}_{-0.07}$	932.05/917	1.02	3.57e-01	7.45e-11
07.07.2003	159960101	$1.72^{+0.01}_{-0.01}$	$2.54^{+0.05}_{-0.05}$	677.44/600	1.13	1.52e-02	8.98e-11
08.07.2003	112770501	$1.79^{+0.02}_{-0.02}$	$2.62^{+0.09}_{-0.09}$	150.75/159	0.95	6.67e-01	8.23e-11
14.12.2003	112771101	$1.66^{+0.02}_{-0.02}$	$1.85^{+0.07}_{-0.07}$	143.59/145	0.99	5.18e-01	7.14e-11
30.06.2004	136550801	$1.70^{+0.02}_{-0.02}$	$1.65^{+0.04}_{-0.04}$	262.88/267	0.98	5.60e-01	5.89e-11
10.07.2005	136551001	$1.57^{+0.01}_{-0.01}$	$1.69^{+0.03}_{-0.03}$	508.42/430	1.18	5.40e-03	7.57e-11
12.01.2007	414190101	$1.35^{+0.01}_{-0.01}$	$2.21^{+0.03}_{-0.03}$	777.89/734	1.06	7.50e-02	1.44e-10
25.06.2007	414190301	$1.55^{+0.01}_{-0.01}$	$1.69^{+0.03}_{-0.03}$	580.01/504	1.15	1.06e-02	7.84e-11
08.12.2007	414190401*	$1.55^{+0.01}_{-0.01}$	$4.04^{+0.08}_{-0.07}$	517.90/523	0.99	4.44e-01	1.93e-10
09.12.2008	414190501	$1.44^{+0.02}_{-0.02}$	$2.08^{+0.05}_{-0.05}$	523.67/459	1.14	3.41e-01	1.16e-10
20.12.2009	414190601*	$1.44^{+0.02}_{-0.02}$	$2.33^{+0.05}_{-0.05}$	421.90/388	1.09	8.97e-03	1.24e-10
10.12.2010	414190701	$1.48^{+0.02}_{-0.02}$	$1.81^{+0.05}_{-0.05}$	355.36/382	0.93	8.70e-02	9.43e-11
12.12.2011	414190801	$1.61^{+0.01}_{-0.01}$	$1.65^{+0.03}_{-0.03}$	593.87/597	0.99	5.28e-01	7.00e-11
16.07.2012	414191001	$1.60^{+0.02}_{-0.02}$	$1.42^{+0.03}_{-0.03}$	333.80/331	1.01	4.47e-01	6.16e-11
13.07.2015	414191101	$1.61^{+0.01}_{-0.01}$	$1.18^{+0.00}_{-0.01}$	533.68/505	1.06	1.82e-01	4.98e-11

[a] Power-law spectral index, [b] Power-law normalization, [c] Spectral flux in the range 2.5–10 keV.

Note: A very broad line feature is likely present in the observations marked with a *.

line can be neutral (e.g. Grandi & Palumbo, 2004; Page et al., 2004; Turner et al., 1990) but at other times it can be ionized (Kataoka et al., 2002; Yaqoob & Serlemitsos, 2000). The detailed properties of this line are governed by the intense gravity and Doppler velocity of the emitting circumnuclear material in the vicinity of the supermassive black hole, but there is no clear understanding of the origin of this line. In our analysis we have detected a broad Fe line in the observation 0159960101 on 2003 July 7. The ratio plot of this spectra with an absorbed power law is shown in Figure 5.2 and the peak-like deviation in the residual from the constant reference line near 6 keV is clearly visible from the first plot. As mentioned earlier, a high energy break is also visible as result of pile-up correction.

To most simply model this emission features we added a Gaussian component to the power law spectrum and allowed the parameters to vary. This gives a similar spectral slope ($\Gamma = 1.73$) as found with a single power-law without adding the Gaussian line. The peak energy of the line lies at $5.79^{+0.08}_{-0.07}$ keV, which corresponds to a line width of $\sigma = 0.220$ keV and equivalent width, EW = 47.39^{+13}_{-16} eV. The line energy estimated here, indicates that the material emitting the Fe Kα line in 3C 273 is neutral or mildly ionized. The width of the Gaussian line found here is similar to those of Seyfert 1 galaxies (Nandra et al., 1997). The line flux is calculated with *cflux* command in *XSPEC*, which gives a flux value $\approx 5.44 \times 10^{-13}$ ergs cm^{-2} s^{-1}, where the overall spectral flux remains exactly the same as the previous value of 8.98×10^{-11} ergs cm^{-2} s^{-1} (see Table 5.3). The addition of the line improves the fit by $\Delta\,\chi^2 = 48$ at the expense of 3 degrees of freedom and the χ^2_r value improves to 1.05 from 1.13. This improvement is 99.99% significant (with rejection probability of 2.0072×10^{-9}) given by the F-test with a F-statistic value of ≈ 15. A Gaussian line follows the relation, FWHM/$\sigma_{line} \approx 2.355$, which yields a FWHM $>$ 20,000 km s^{-1} ($\sim 0.08c$) for this line. Such a broad line width is unlikely to originate from broad line region clouds or be due to the irradiation of high energy photons on to the cold dusty torus (Nandra, 2006) but more probably originates from a Seyfert like component: the inner accretion disc (Reynolds, 2001).

Apart from this quite clear observation of an emission line, four other observations apparently show excess emission at energies between 5–7 keV in the ob-

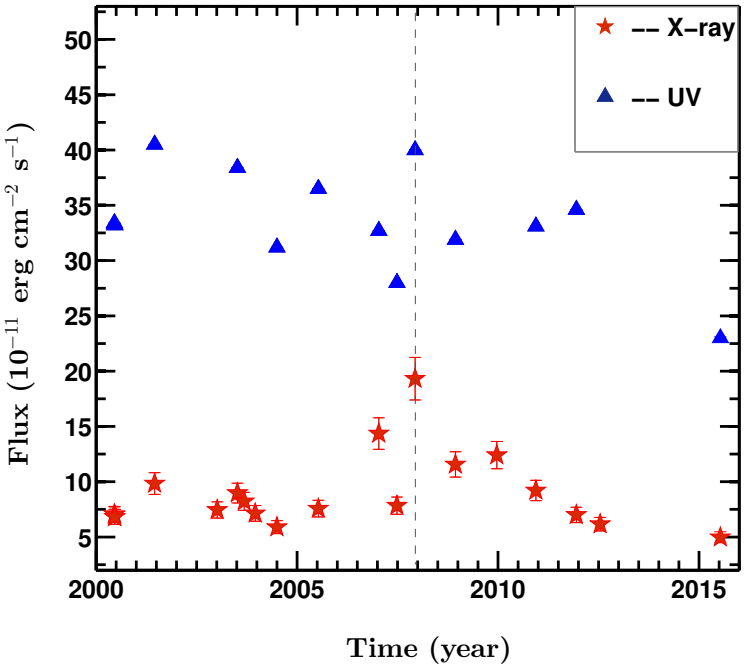

Figure 5.3: Temporal variation of the X-ray and UV fluxes. The vertical dotted line emphasizes the flaring period.

servers' frame, but these lines are too weak to be considered as significant detection. However, broad Gaussian line fits to these spectra give modest improvements to the χ^2_r values and as well as the residual plots. These observations are marked with a star symbol in Table 5.3. Although we tried to fit these putative broad lines with accretion disc models for both Schwarzschild geometry (Fabian et al., 1989) and Kerr geometry (Laor, 1991) the statistics are too poor to allow quoting any results for these fits.

5.4 Spectral Evolution and Correlations

5.4.1 Variation of the Power-law Continuum

Before studying the evolution of the spectra, we investigate the emission states of the source at the time of these *XMM-Newton* observations. Multi-wavelength moni-

toring of the source in June 2004 revealed a historic minimum in the sub-millimeter, infrared and X-ray bands (Türler et al., 2006). During the June 2003 XMM observation, the source reached a historically softest state in the X-ray band as reported in Chernyakova et al. (2007); they also mentioned that the source evolved towards a softer X-ray state. The source was in a high state in the hard X-ray band (18–60 keV) detected by the AGILE satellite during December 2007 and January 2008 (Pacciani et al., 2009). Several consecutive X-ray flares were observed in the source between 2005 to 2012 with sequential high and low states with *RXTE-PCA* (Esposito et al., 2015), but only one *XMM-Newton* observation taken (in December 2007) within this period coincides with the occurrence of a small flare in the source.

From the literature (Chernyakova et al., 2007; Esposito et al., 2015; Page et al., 2004) we find that, except for the flaring period mentioned above, all the *XMM-Newton* observations we are analyzing were carried out during a low/quiescent state of 3C 273. This gives us an excellent opportunity to study the long term spectral behaviour of this FSRQ in the low state.

In Figure 5.3, we have plotted the temporal variation of X-ray fluxes extracted from individual spectral fits along with the ultraviolet fluxes from simultaneous OM observations. Between mid-2000 and mid-2015 the 2.5–10 keV flux changes by a factor of three, being 4.98×10^{-11} ergs cm^{-2} s^{-1} as the lowest flux (July 2015) and 1.9×10^{-10} ergs cm^{-2} s^{-1} during the flaring period. The 2.5–10 keV X-ray flux in 2015 calculated here has a smaller value than the flux, 5.89×10^{-11} ergs cm^{-2} s^{-1}, found at the historically faintest period (June 2004). It can be seen from the figure that during 2015 the UV band flux is also the lowest as compared to other epochs. Thus we can say that 3C 273 reached a new minimum flux state in 2015 which is even fainter than the historically low flux state during 2003–2004. From the figure we can also see that the flaring period indicates the highest flux state in both X-ray and UV bands (1.9×10^{-10} ergs cm^{-2} s^{-1} and 4.0×10^{-10} ergs cm^{-2} s^{-1}, respectively).

The overall shape of the X-ray spectra manifests the X-ray emission mechanisms and variation of the spectral slope can indicate changes in the geometry of

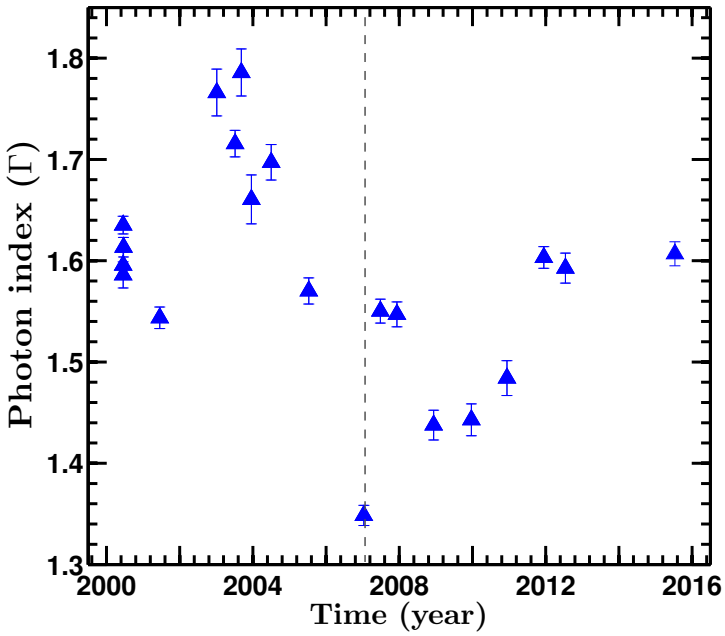

Figure 5.4: Evolution of the spectral index from June 2000 to July 2015, showing a significant variation of $\Delta\Gamma = 0.44$. The dotted line emphasizes the flaring period.

X-ray producing region. We will discuss this in some detail in section 5.5. The temporal spectral variation of the source from 2000 to 2015 is shown in Figure 5.4. During this period the spectral slope varies significantly, with Γ ranging between 1.35 and 1.79. In the energy band 2.5–10 keV, we found a strong anti-correlation between the spectral slope and the flux, i.e., a "harder-when-brighter trend", in the sense that the spectra get harder with increasing flux (Figure 5.5, top). Excluding the data point taken during the flare, the Pearson correlation between these two parameters is $R = 0.72$ with 0.9999 probability of correlation. We also checked if there was any relation between the X-ray spectral slope and the UV flux but find that these quantities are not related (Figure 5.5, bottom). In addition, the normalization to the power spectra, N, is not related to the photon index but is unsurprisingly connected to the flux, with a correlation coefficient of 0.85 (including the flaring point), as depicted in bottom panel of Figure 5.6. In these plots the flaring point is usually an outlier, and to make that clear, it is shown inside a small rectangular box.

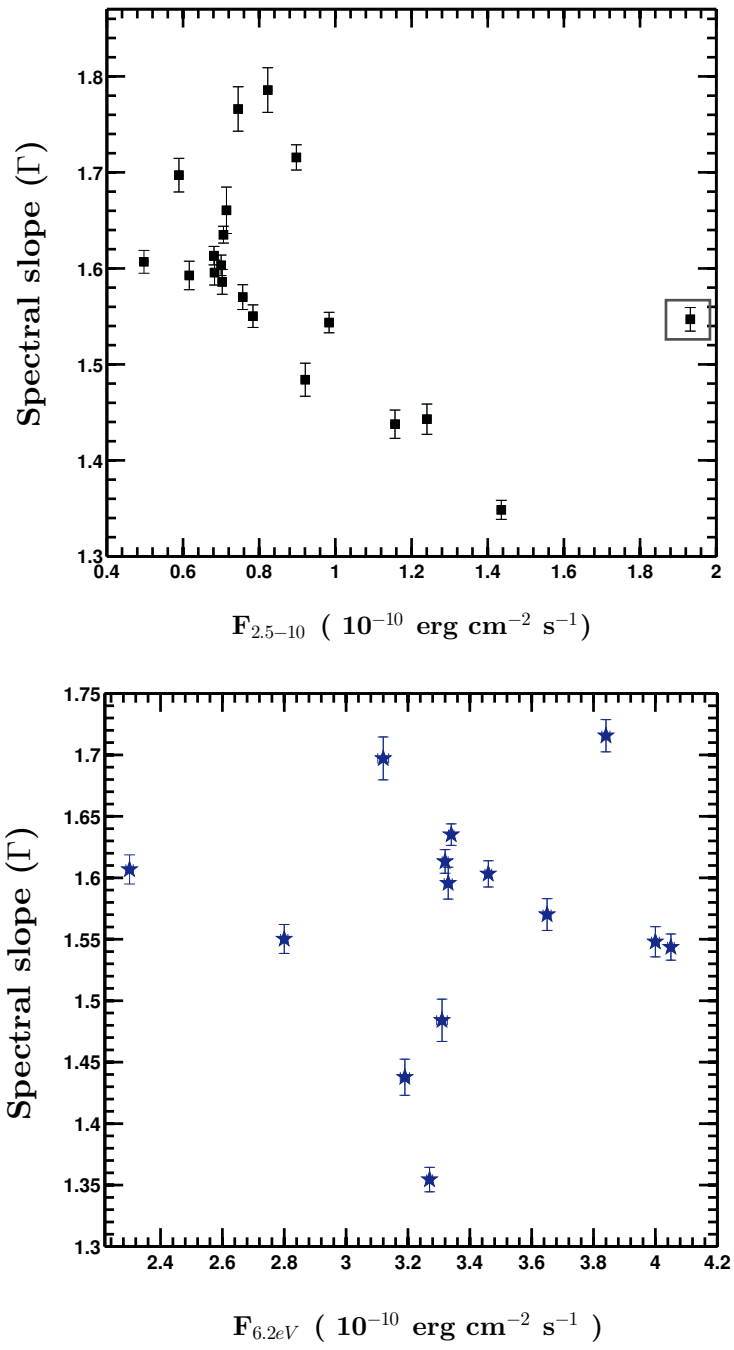

Figure 5.5: Top: A strong anti-correlation between the 2.5–10 keV flux and X-ray spectral slope over that band is present, except for the rightmost point inside the small box that corresponds to the 2007 X-ray flare. **Bottom:** X-ray spectral slope vs. ultraviolet flux in the 6.2 eV band.

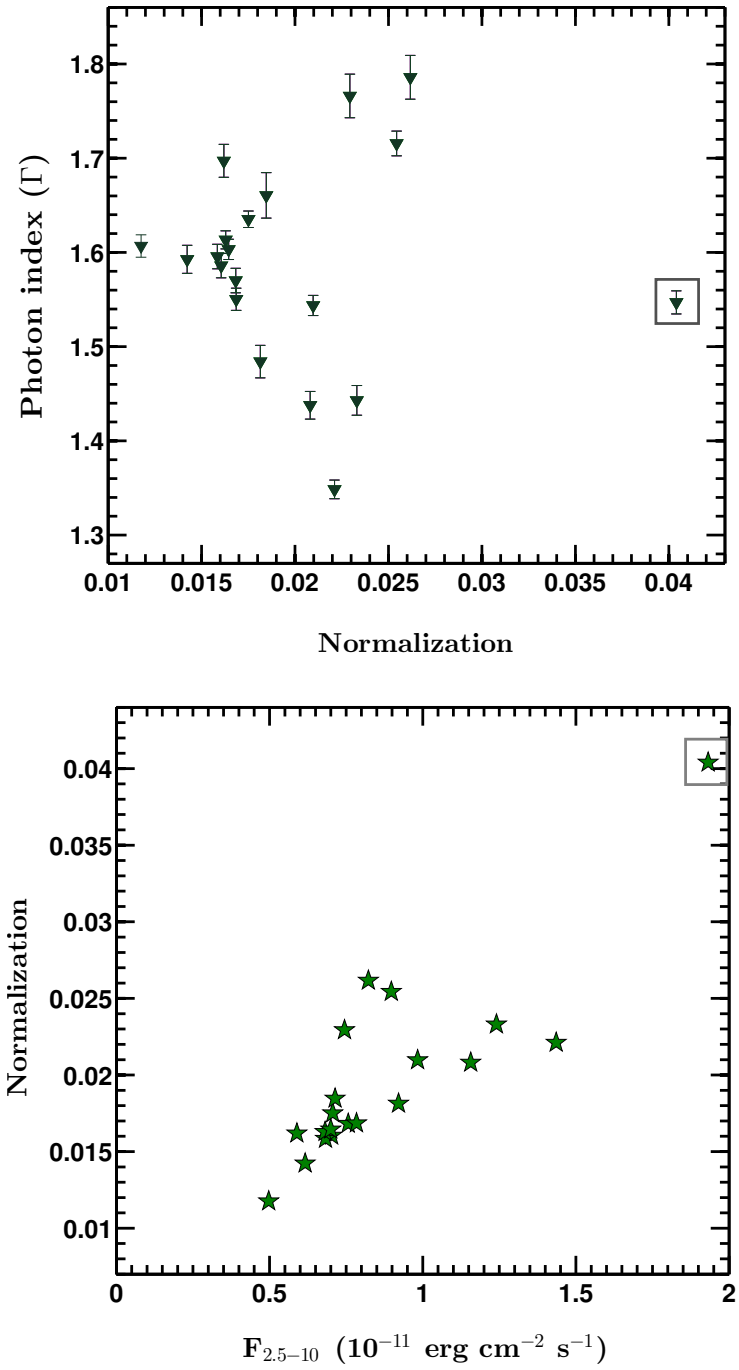

Figure 5.6: Top: X-ray spectral index as function of the normalization used for the fitted power law. **Bottom:** Normalization vs. spectral flux. X-axis error bars in both figures are smaller than the point size. Normalization is in units of photons $\mathrm{keV}^{-1}\mathrm{cm}^{-2}\mathrm{s}^{-1}$.

5.4.2 Correlation between X-ray and UV Emission

A long standing question regarding the relevance of Compton scattering of UV photons to X-ray energy is still unresolved in 3C 273. The X-ray emission from AGNs can result either from a continuation of the synchrotron spectrum or from inverse Compton emission from low energy seed photons scattered off a thermally hot distribution of electrons (corona-like structure) situated above the accretion disc or from inverse Compton scattering off the relativistic electrons in the jet. Since 3C 273 is a borderline object and shows both Seyfert-like and blazar-like emission, an inverse Compton mechanism has been introduced to explain X-ray emission from time to time (Bezler et al., 1984; Grandi & Palumbo, 2004; Leach et al., 1995; Sunyaev & Titarchuk, 1980). Because of observational constraints and the lack of simultaneous observations in these bands, this thermal inverse Compton explanation requires additional evidence, as significant proof of this point may expand our understanding of AGN emission mechanisms. Fortunately, *XMM-Newton*, with its Optical Monitor (OM) attached to the X-ray telescope, can observe a source in both X-ray as well as in multiple optical/UV bands at the same time. Taking advantage of this facility, we can try to understand the origin of the X-ray emission for this source in the low state.

Walter & Courvoisier (1992) for the first time found a correlation between X-ray (2–10 keV) and UV (10 eV) emission in 3C 273 with *Ginga*, *EXOSAT* and *IUE* quasi-simultaneous X-ray and UV observations taken during 1984 to 1988. They studied the 2–10 keV spectral energy index vs. logarithm of the ratio of the 2–10 keV to UV count rates and found an linear anti-correlation between them. This strongly supports the thermal inverse Comptonization model as being responsible for this portion of the X-ray emission in the source. But later, Chernyakova et al. (2007) did a similar analysis with some early *XMM-Newton* observations (2003–2005) where they did not find any correlation.

Following their work, we have reexamined this relation with 15 years of *XMM-Newton* data, obtained simultaneously for both X-ray and UV bands. In the top panel of Figure 5.7 we plot the X-ray flux against the UV flux and note that though

there is a great deal of scatter there also is a weak linear relation between them with correlation coefficient of 0.50 (if the flaring point is included). In the bottom panel of Figure 5.7 we have plotted the 2.5–10 keV spectral index as a function of logarithm of the ratio of the 2.5–10 keV to UV flux, as extracted from UVW2 filter. There we clearly see a significant anti-correlation, as was found in Walter & Courvoisier (1992). Recall that nearly all of these observations were taken during the low state of the 3C 273. The solitary exceptional point at the extreme right corresponds to the 2007 X-ray flare. Excluding this point, a least square fitting to the rest of the points gives a correlation coefficient of 0.88 with a slope of -0.346.

We further extended this study to different optical/UV bands extracted from *XMM-Newton*. Significant anti-correlations, similar to that found between X-ray and UVW2 bands, are present between X-ray photon index and logarithm of the ratio of the 2.5–10 keV to the flux in each of the other optical/UV bands. The correlation coefficients of these relations are 0.89, 0.84, 0.80, 0.76, 0.87, for the UVM2, UVW1, U, B, V bands, respectively.

5.5 Discussion

We have showed in section 5.3 that almost all the spectra of 3C 273 between 2.5–10 keV energy range, observed during 2000 to 2015 by *XMM-Newton* are well described by a simple power law model. As is typical for AGNs where sufficient data is available, spectral variation can be seen in 3C 273. In section 5.4, we presented the temporal variation of X-ray spectral slope of 3C 273 and its relation with several spectral parameters.

In this work we have found a very clear anti-correlation between the slope of the X-ray spectra and the flux of 3C 273, which means the spectra flatten with increasing flux, as is clearly visible from Figure 5.5. Surprisingly, this is totally opposite what reported in Kataoka et al. (2002), where the spectra became steeper when the source is brighter, similar to that typically observed in Seyfert galaxies. The critical point is that nearly all the observations used for our study were taken when the

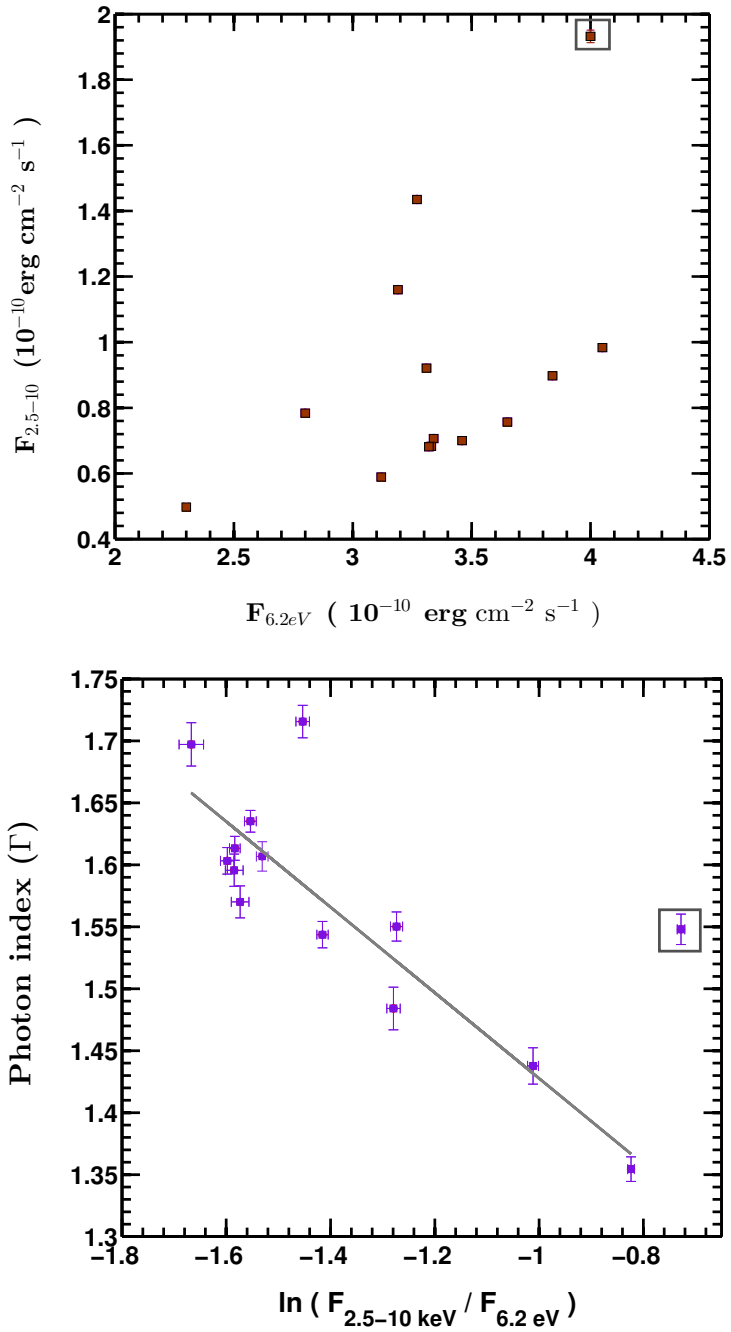

Figure 5.7: Top: X-ray flux in the energy range 2.5–10 keV vs. ultraviolet flux at energy 6.2 eV. **Bottom:** The 2.5–10 keV spectral index as a function of the logarithm of the ratio of the 2.5–10 keV to 6.2 eV UV flux shows a significant anti-correlation.

source is in a low or quiescent period. The exception to this relation occurs during the December 2007 X-ray flare reported in Esposito et al. (2015).

In most of the previous studies of this source any relation between the slope and flux was absent (Chernyakova et al., 2007; Page et al., 2004; Soldi et al., 2008; Turner et al., 1990). However, a softer when brighter pattern of the 2–10 keV X-ray spectra was reported in Figure 6 of Kataoka et al. (2002) with *RXTE* observations made during 1999–2000, while this relation was absent with the 1996–1997 observations when the source was in a relatively lower flux state than in 1999–2000. The positive slope–flux relation reported by (Kataoka et al., 2002) was interpreted by them in the context of non-beamed, thermal emission from the accretion disc and reprocessed emission from the thermal corona. So the different circumstances under which the slope-flux correlation is present or not require further investigation in future observations. An anti-correlation between slope and flux was reported in Madsen et al. (2015) with 244 ks continuous *NuSTAR* exposure of 3C 273 made in July 2012 in the energy range 3–10 keV, where they have postulated that this type of variation is driven by the jet emission while the spectra harden with an increasing jet contribution to the flux. But our results do not concur with their interpretation since we have found the anti-correlation during the low states of the source when the emission from the jet is almost certainly at a minimum. Moreover, the existence of the connection between optical/UV and X-ray bands in our study, represent a different scenario where the X-ray photons are emitted through inverse Compton scattering of UV photons from a thermal corona (see section 5.4.2 and below). Hayashida et al. (2015) reported a similar spectral variability; harder-when-brighter (for soft spectra, 0.5–5 keV), in 3C 279 during a flaring state of the source with *SWIFT-XRT* data. It has been extensively reported and believed that the emission mechanisms and hidden physical scenario in 3C 279 and 3C 273 are similar and both belong to the same category (border line objects). But the presence of a slope-flux anti-correlation in different states of the sources make for a more complicated emission behaviour. In general, a harder-when-brighter trend is seen in the X-ray spectra of high frequency peaked blazars or in flaring blazars where the SSC emissions from the jet play dominant role (Emmanoulopoulos et al., 2012; Gliozzi et al., 2006; Krawczynski et al., 2004).

The X-ray emission of FSRQs is quite complex and interesting, where the physical mechanism responsible for the emission is still not understood very well. In radio quiet AGNs, particularly Seyfert galaxies, the slopes of the X-ray spectra are linearly correlated with the 2–10 keV X-ray flux i.e., the spectra steepen with increasing fluxes (Caballero-Garcia et al., 2012; Sobolewska & Papadakis, 2009, and reference therein). This softer-when-brighter behaviour in Seyfert galaxies in the 2–10 keV band is explained with different spectral variability models. Such spectral variability might be totally intrinsic and may arise from variation of accretion rate in the source, i.e., softer X-ray spectra correspond to higher accretion rates (Shemmer et al., 2006; Sobolewska & Papadakis, 2009). Moreover there could be a X-ray absorber with variable ionization state which is directly related to the intrinsic variation of the power law continuum or with a variable column density or covering fraction and thus with a variable opacity along the line of sight, which absorbs X-rays from an constant intrinsic continuum (Sobolewska & Papadakis, 2009; Turner et al., 2007). Another interpretation for softer-when-brighter spectra is that the spectral variation is a result of combined contributions from a power-law continuum which is highly variable in flux but with a constant spectral shape and a constant reflection component (Ponti et al., 2006; Taylor et al., 2003). Or this trend may occur due to superposition of a constant reflection component and a variable continuum which is variable in both flux and shape (Sobolewska & Papadakis, 2009).

It has been suggested that the observed softer-when-brighter or harder-when-brighter trend is related to the accretion rate of the system. The harder-when-brighter correlation was reported in Gu & Cao (2009) for a sample of low luminosity AGNs (LLAGNs) and interpreted in the context of advection-dominated accretion flows (ADAFs), where the X-ray photons are result of Comptonization of seed photons in the ADAF. A similar trend was observed in a sample of LINERs by Younes et al. (2011). Wu & Gu (2008) reported that in case of black hole X-ray binaries (BHXRBs) the harder-when-brighter trend is observed when the BH accretion rate is below a critical value. Above this critical accretion rate a softer-when-righter trend is observed. A similar behaviour has been observed in AGNs with different

studies (Connolly et al., 2016; Gu & Cao, 2009; Younes et al., 2011), supporting the accretion rate dependence of spectral trend as observed in the case of BHXRBs. Another explanation of this behaviour is an out flowing hot corona situated above an untruncated accretion disc, where the seed photons for Compton scattering come from the disc (Sobolewska et al., 2011).

The slope-flux correlations observed in 3C 273 in all previous studies are based on short term spectral studies of the source. From our result and earlier studies, we conclude that the short term positive slope-flux relation reported in Kataoka et al. (2002) is found only in high states of the source while the negative slope-flux relation is seen during low states of 3C 273. So the harder-when-brighter trend observed here, in 3C 273 during its low state might be result of smaller accretion rate.

The higher sensitivity of *XMM-Newton* EPIC-pn data, allowing for an excellent signal to noise ratio, gives us more precise spectral parameters than do all the previous studies. In addition to this, the ability of *XMM-Newton* to take simultaneous X-ray and optical observations of a target gives us more useful results. Considering the data as a whole, it seems fair to conclude that the appearance, or not, of a relation between the X-ray slope and flux depends on the source state. We can say that the spectral slope is related to the continuum flux during low state, when the contribution to the continuum from the jet emission is minimum. It is worth noting that the apparent absence of this relationship in some earlier work may also be due to the small number of spectra available or because of the poorer quality of data.

In section 5.4.2, we examined the relation between UV (6.2 keV) and X-ray emission through simultaneous observations in these bands. When the UV fluxes are plotted against X-ray flux (top panel, Fig. 5.7), a weak correlation between them was observed, but we saw a substantial correlation between X-ray spectral index and the ratio of the X-ray to UV fluxes during the generally low state (bottom panel, Fig. 5.7). The observations carried out during the historical low state of the source in 2003 (upper left points in that plot) show somewhat higher deviations from the line representing the correlation and their inclusion reduces the correlation coefficient value from 0.96 to 0.87 quoted above. Again, the observation taken in December

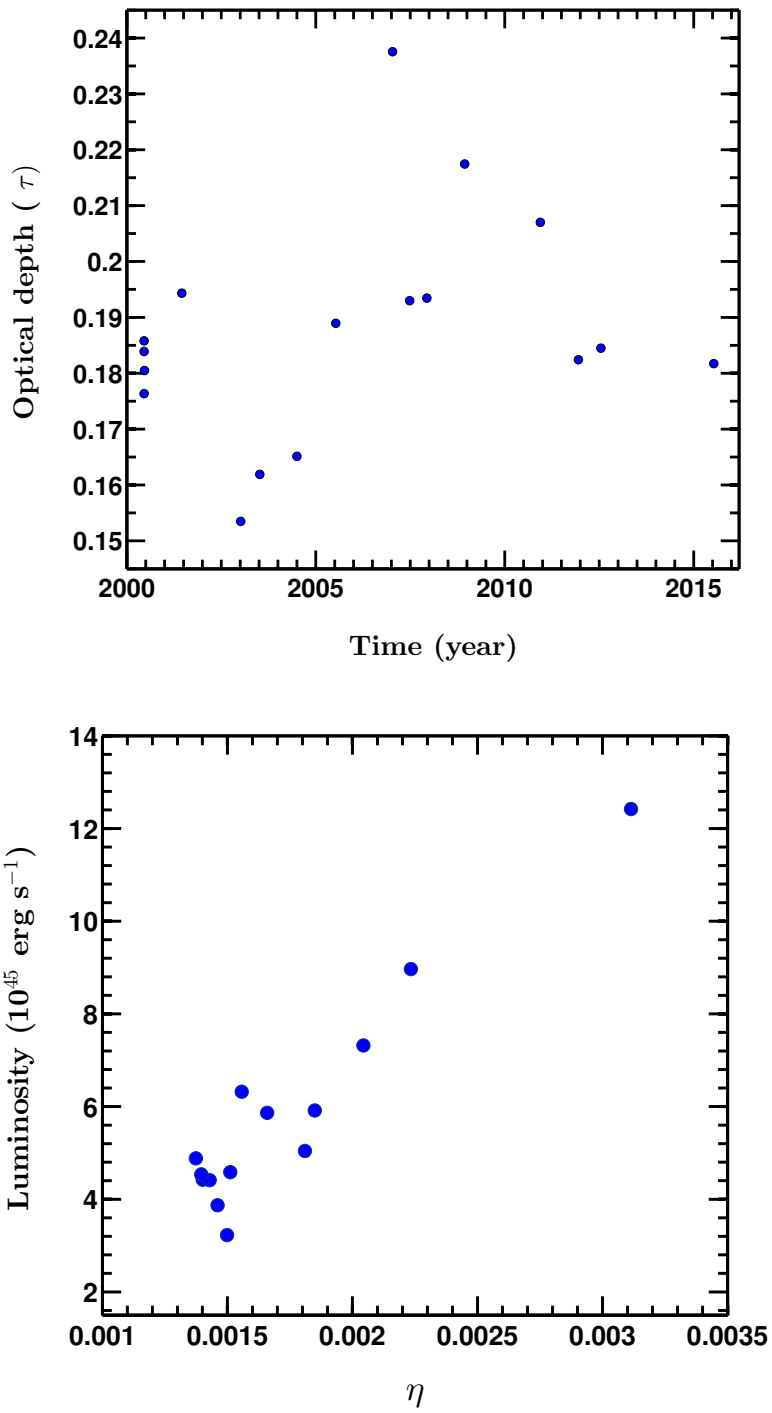

Figure 5.8: Top: Variation of optical depth of the comptonizing medium at different epochs. **Bottom:** X-ray luminosity of the source vs. covering factor of the Comptonizing medium.

2007 during flaring activity does not follow this pattern. In a previous study this type of X-ray flares were argued to be counterparts of infrared/optical flares with a lag of few months (Walter & Courvoisier, 1992) and VLBI radio observations found that times of X-ray flares coincided with the birth of new radio knots (Baath et al., 1991). Considering these observations, we checked the literature for such connections to the 2007 X-ray flare in the source. The mm flux reached its minimum in 2004, and since about 2006 this flux has shown high variability (Trippe et al., 2011). However, in this case no counterparts of this X-ray flare were noted in either radio or optical bands; moreover, we could find no report on the birth of any radio knot related to this 2007 "orphan" X-ray flare.

The significant anti-correlation between the hard X-ray spectral slope and the ratio between X-ray and UV fluxes can be interpreted in the context of coronal emission. The presence of a hot corona located in the inner region of the central engine of AGN is well accepted and widely used to interpret the hard X-ray emission in AGN through multiple up-scattering of soft seed photons by the thermal gas (Haardt & Maraschi, 1991; Nandra et al., 2000; Nandra & Papadakis, 2001).

The lack of clear flux correlations imply that the X-ray emission in 3C 273 can be disengaged from emission at lower frequencies dominated by the synchrotron mechanism. The possible explanation that the X-ray photons are coming from the SSC process is inadequate to explain accurately the observational results. Thus, a picture of thermal inverse Compton scattering from a corona has been applied to interpret X-ray emission process in 3C 273 (McHardy et al., 1999; Page et al., 2004; Walter & Courvoisier, 1992). If we consider that inverse Compton scattering is responsible for most of the X-ray emission in 3C 273 then the presence or absence of correlations between slope and flux must be dependent on the variations of the physical parameters of the Comptonizing medium. In particular, the variation of the X-ray spectral slope must be related to the variation of physical conditions in the medium scattering those X-rays. If the Comptonization is purely thermal then the slope will be governed by both the temperature and Thomson optical depth of the electron distribution in the medium. Since the number of incident soft seed photons to the number of emerging high energy photons ratio is directly proportional to the

optical depth of the scattering medium, this must be tightly tied to the slope of the power law describing the Compton emission.

For inverse Compton process in an optically thin electron gas, the rate of production of X-ray photons from UV photons is given by the relation (Walter & Courvoisier, 1990)

$$N_X = \eta(1 - e^{-\tau})N_{UV}, \tag{5.1}$$

where N_X and N_{UV} are the emission rates of inverse Compton processes and soft seed photons from the BBB, respectively; η is the covering factor of the thermal gas surrounding the source of UV seed photons; and τ is its optical depth of the scattering medium. The above equation can be simplified to

$$N_X \approx \eta\tau N_{UV}, \tag{5.2}$$

when τ is small.

The slope of the power law spectrum Γ triggered by inverse Compton emission is given by Rybicki & Lightman (1979), as

$$\Gamma = -ln(\tau)/ln(A), \tag{5.3}$$

where A is the fractional energy gain per scattering, or the amplification factor of the Compton scattering. For mildly relativistic electrons this is given by (Sunyaev & Titarchuk, 1980),

$$A = 16(kT/m_e c^2)^2. \tag{5.4}$$

If we consider that the X-ray spectrum is generated mainly by the inverse Compton emission from a relativistic hot electron gas triggered by the low energy ultraviolet seed photons, a relation between the photon index of the X-ray spectra and the ratio of X-ray flux to the UV flux can be established as (Walter & Courvoisier, 1990, 1992):

$$\Gamma = \frac{\ln(F_{2.5-10keV}/F_{6.2eV})}{\ln(A)} + f(\eta, A). \tag{5.5}$$

From the above equations we can find the gain factor, A, from the slope of the spectral index vs. flux ratio when the X-ray flux and spectral variability correlation is caused by variation of optical depth. Once A is known, then the temperature, T of the Comptonizing medium can be calculated from Eq. 5.4. The optical depth τ, and covering factor η, of the thermal gas can be estimated from Eq. 5.2 and Eq. 5.5, respectively. From the anti-correlation found in Fig. 5.7, which is nothing but $\Delta\Gamma/\Delta\ln(F_{2.5-10keV}/F_{6.2eV})$, the other parameters can be estimated. The estimated value of the temperature (kT) of the thermal gas is 5.4×10^2 keV, and, confirming our assumption of small optical depth, the τ values lie in the range 0.18–0.24. We next examine the variation of optical depth of X-ray emitting medium with time and display it in the left panel of Figure 5.8. The optical depth value is highest during the "flaring state" in 2007 and has its smallest value in a very low state in 2003. If we consider the the X-ray source as isotropic then the value of covering factor η is found to be in the range $\approx$ 0.0014–0.0031 which is substantially lower than the value of $\approx$ 0.02 estimated by Courvoisier & Camenzind (1989). The covering factor is apparently roughly linearly related to luminosity of the source, as shown in the right panel of Figure 5.8.

These results possibly can be explained in the context of accretion disc winds. Accretion discs are associated with intense and twisted magnetic fields and while the topology of the magnetic lines is still not understood properly, various simple models provide reasonable places to start. Much of the energy generated in the disc can be dissipated either as a wind or as a relativistic jet in the form of bulk outflow (e.g. Blandford & Payne, 1982). Livio et al. (2003) proposed a model for a disk-jet connection in X-ray transients and AGNs, wherein the inner accretion disc has two states. In one state, the energy emitted within the disc may dissipate locally in the form of a disc wind into the low-density regions above and below the disc to produce a corona-like structure. In the other state, a huge amount of energy emerges from the inner part of the disk as collimated relativistic jets propelled by large scale magnetic fields. In the first case of the inner disc state magnetic force cause generation of shocks in the wind fields, which thermalize both protons and electrons. The electrons are further energized as a result of interactions with the thermal protons. These highly energetic electrons are later cooled off by inverse Comptonization of

seed UV photons coming from the inner disc or from the jet. Within this framework, in the low state of 3C 273 the inner accretion disc is in the first state, which is insufficient to project the material and radiation in the form of collimated jet. Then the hot electron gas is carried out by disc winds to a region where they eventually up-scatter the UV seed photons into X-rays.

5.6 Conclusions

In this chapter, we have presented a new analysis of simultaneous X-ray and ultraviolet observations of 3C 273, taken with *XMM-Newton* during 2000–2015. The key conclusions of this work are:

— Almost all of the 20 quality X-ray spectra in the 2.5–10 keV energy range are well described by a single power-law model with Galactic absorption due to neutral hydrogen along the line of sight to 3C 273. All but one of these measurements were made while 3C 273 was in an overall low state.

— A new lowest X-ray flux state of 3C 273 was observed in July 2015. During this period the 2.5–10 keV flux (4.98×10^{-11} ergs cm^{-2} s^{-1}) is even lower than the flux observed (5.89×10^{-11} ergs cm^{-2} s^{-1}) at the historically faintest period (June 2004).

— A weak broad iron emission line was detected at 5.8 keV during a lowest state of the source in 2003. The line is well represented by a Gaussian profile of equivalent width 47 eV. The width of the line gives an equivalent FWHM value $>$20,000 km s^{-1}. Very broad emission line features at energies between 5–7 keV appeared to have been present in 4 other observations, but they were too weak to be well fit.

— The X-ray continuum of 3C 273 in the energy range 2.5–10 keV varies significantly even in the low state of the source. A “harder-when-brighter” trend of the X-ray spectra is observed, which can be explained either as a result of lower accre-

tion rate in the central engine or through an outflowing hot corona situated above an untruncated accretion disc.

— The presence of strong anti-correlations between X-ray spectral slope and different optical/ultraviolet emission fluxes indicates a nearly co-spatial origin of these bands. This supports the picture that the X-ray continuum arises from the comptonization of BBB photons in a medium of a partially relativistic thermal electron gas in the local environment of the AGN's central engine.

Chapter 6

Summary and Future work

This thesis explores the physical and statistical properties of blazars, by adopting a multi-wavelength approach. Study based on multi-band observations, specially simultaneous, is very important in putting meaningful constraints on different emitting regions and to investigate the broadband emission mechanisms that have been used to explain the observed radiation. In addition to that the origin of X-ray emission and its relation with other emission bands has always been a fascinating research area in AGN physics. In this thesis, taking the benefit of highly sensitive X-ray and optical/UV observing facility: *XMM-Newton*, we have investigated different variability properties in a sample of blazars and studied X-ray spectral evolution of the first discovered quasar, 3C 273.

In the following sections we summarize the main results, discuss their implications, our ongoing work and give a brief overview of future perspectives of the work presented in this thesis.

6.1 Variability in the FSRQ 3C 273

In Chapter 3, the multi-wavelength variability properties of the FSRQ, 3C 273 were studied along with correlated variability investigation between different emission bands as well as different emission mechanisms over a period of time $\sim$12 years. We have undertaken a nearly simultaneous optical/UV and X-ray data available

from the XMM−Newton satellite mission from June 2000 to July 2012. In this study, we focus on the multi-wavelength flux variability on both intra-day and long time scales of this very well known radio-loud source. To estimate the strength of variability, we used the parameters, excess variance and fractional variability amplitude (F_{var}). On intra-day time scales 3C 273 showed small amplitude variability in X-ray bands with highest F_{var} value of 2.6 %, but we found high flux variability over long time scales in all bands (6 optical/UV bands and 2 X-ray bands) for which observations were made. The optical/UV variability amplitude was more than twice than that in the X-ray bands. We have found a frequency dependence of the variability in optical/UV bands in the sense that the variability amplitude increases with increasing frequency; however, the X-ray emissions disagree with this trend as the variability amplitude decreases from soft to hard X-ray bands. A hardness ratio analysis in the X-ray regime indicates that the particle acceleration mechanism dominates the cooling mechanism during most of the $\sim$12 year span of these observations.

To summarize, the absence of IDV in the X-ray light curves can be attributed to weak accretion disc instabilities, because any flux variation triggered by jet is dominated by relativistic beaming effect (due to the close alignment of the jet axis) which would have highly amplified the observed flux variation and hence the F_{var}. This explanation is partially supported by the opposite trend of frequency dependent variability in the X-ray bands on longer timescales, however the positive trend observed in the optical/UV bands can be explained through jet emission.

6.2 SED Synchrotron Peak and X-ray IDV

In Chapter 4, a statistical analysis of a sample of blazar was done to understand the relation between IDV in X-ray bands and the synchrotron peak of blazar SED. As discussed earlier, blazars can be divided into two sub-classes namely high energy and low energy peaked blazars. In spectral energy distribution, the first synchrotron hump of the former class peaks in UV/X-rays and in IR/optical bands for the latter class. The peak of the spectral energy distribution seems to be responsible for variability properties of these classes of blazars in X-ray and optical bands. Since, in

low energy peaked blazars, the X-ray bands lies well below the synchrotron hump, one expects that the highest energy electrons available for the synchrotron emission would have slower effect of variability on X-ray intra-day timescale. In this study, by taking the advantage of a sample of 12 low energy peaked blazars with total 50 observations from XMMNewton since its launch, we confirm that this class is less variable in X-ray bands. We found that out of 50 observational light curves, genuine intra-day variability is present in only two of light curves i.e 4 % duty cycle. These two observations belong to outburst states of two sources, when the synchrotron peak found to shift up to x-ray bands. Similar results were obtained from earlier optical intra-day variability studies of high energy peaked blazars where out of 144 light curves, only genuine intra-day variability was detected in 6 light curves i.e $\sim$ 4 per cent (Gaur et al., 2012a,b,c).

An explanation can be provided in terms of position of the low energy peak of SED in different blazars. In case of LSPs, X-ray bands lie below the first peak of the SED where inverse Compton mechanism is dominating rather than synchrotron cooling. As a result, changes in the efficiency of particle acceleration and the rate of emission would lead to slower variability in these bands. Hence, reducing their intra-day variability in X-ray bands as compared to the variability in optical bands.

6.3 Origin of X-ray in 3C 273

Chapter 5 is based on the X-ray spectral analysis of the luminous quasar 3C 273 in the energy range 2.5–10 keV, and study of simultaneous observations in UV wavelengths, as obtained during *XMM–Newton* pointings toward the source from 2000 through 2015. A new minimum flux state of 3C 273, even lower than the historical minimum during 2003–2004, was observed in 2015 in the 2.5–10 keV spectra. The continuum emission from 3C 273 is best described by an absorbed power law, but in one case, during extremely low activity of the source, presence of a fluorescence K-shell iron line was detected which can be attributed due to emission from BLR region moving with a velocity $\sim$ 20,000 km s^{-1} residing at a distance of 1 pc from the core. We have studied the spectral evolution of the source during its low or quiescent state over an extended period and also examined connections between

the X-ray and ultraviolet emissions from the source, which have been seen in some previous work but not in others. A harder-when-brighter trend for the X-ray spectrum is observed in these long-term multi-epoch observations of 3C 273 for the first time which can be explained through smaller accretion rate of the central engine as observed in BHXRBs or by outflow of disc material to low density space situated above and below an untruncated disc. Our study finds a significant detection of an anti-correlation between these two bands during the low state that characterized 3C 273 for most of this period; however, the relation we have found is not applicable during a flaring state of the FSRQ. These results are statistically stronger and more significant than the previous claim for this reported in Walter & Courvoisier (1992) in support of the same origin for UV and X-ray emission.

From our study, we conclude that the 2.5–10 keV X-ray emission in 3C 273 is the result of inverse Compton scattering of soft UV seed photons (emitted from the local environment of the AGN), most likely in a thermal corona. We can explain the significant temporal variation of the spectral continuum in 2.5–10 keV as an outcome of changing optical depth of the comptonizing medium, along the lines of the wind-shock model proposed by Courvoisier and Camenzind (1989).

6.4 Current Work & Future Plan

This thesis is mainly focused on the multi-wavelength variability properties of blazars and spectral evolution of the FSRQ 3C 273, utilizing the observations taken by *XMM-Newton* satellite. A short discussion on our ongoing work and future research plans are presented below.

In order to improve our understanding about the complex emission from the relativistic jet and the jet structure, an extensive investigation for possible correlations, variability timescales and QPOs in a sample of ISP blazars in their outburst state has being carried out, with the most efficient techniques like Structure Function (SF), Auto-Correlation Function (ACF), Discrete correlation function (DCF) & Power Spectral Density (PSD). The key motivation of this work is to search for IDV in X-ray bands and examine the different variability nature in a sample of ISP blazars

in their high state. The reason behind particularly selecting sample of ISP blazars is that, the intermediate class of blazars are not well explored as high synchrotron peaked blazars (HSPs or widely known as HBLs) and the low synchrotron peaked blazars (LSPs or LBLs). Since ISPs are the connecting link between HSPs and LSPs, their study should reveal some interesting information about all these classes of blazars. Choosing ISPs specifically in high state has two advantages; firstly, in high state the emission is jet dominated, so this will help us to understand the jet dynamics and structure together with different emission mechanisms involved in the jet and secondly, in high state the SED synchrotron peak of ISP blazars shifts to X-ray range (Abdo et al., 2010c; Gaur et al., 2012; Gupta, Kalita et al., 2016) which is expected to fall in the range of *XMM-Newton*. With these two aspects we will try to understand the different emission mechanisms, dynamics and structure of the relativistic jet.

The preliminary results of this work is discussed briefly in this section. The techniques mentioned above are being applied for one ISP blazar, ON 231 so far, which was the 1st ISP detected in TeV range. The source was detected in outburst state in June 2008 in almost all wavebands including X-ray and XMM-Newton observed the blazar during the outburst in three consecutive periods covering multiple X-ray flares. Genuine IDV has been detected in all these exposures with F_{var} value lying in the range $\sim 27-38$ % with 100% duty cycle. To check the frequency dependent variability and emission, we split the $0.3-10$ keV light curve into different energy ranges i.e., 0.31, $1-2$, $2-3$, $3-4$, $4-7$ and $7-10$ keV bands. We have observed that the source was highly variable in the softer energy bands as compared to harder one and also emission in soft X-ray bands ($0.3-1$, $1-2$, $2-3$ keV) are much more higher than that in high energy bands. Variability timescale search with SF indicates that any possible timescale is either equal to or greater than the observation length. We also search for QPO with PSD analysis, but found that no quasi-periodic oscillation was hidden in the red noise data set. With DCF analysis, we have found that the $0.3-1$, $1-2$, $2-3$ keV bands are emitted through emission mechanisms in a single region, while the $0.3-1$ & $4-7$ keV time series data shows a negative lag of 1800 s indicating that they were emitted through same mechanisms but in different emitting regions. As far as we know, the soft lag in the inter-bands X-ray variabil-

ity in the blazar ON 231 has been detected for the first time in this study. But the $0.3-1$ & $7-10$ keV light curves are not correlated to each other which implies that they emitted through different emission mechanisms. The observed results can be interpreted through synchrotron cooling of the high-energy electrons from different parts in the inhomogeneous relativistic jet; as the higher frequencies being emitted from the inner and denser parts of the jets, while the lower frequencies being emitted from comparatively more distant and less dense parts. Also it may be result of material propagating through a rotating helical path in the jet. (This work is in under progress.)

The X-ray spectral study presented in this thesis is based on only one object, 3C 273. Further investigation is needed in order to obtain a generalized view of our findings and their application to other FSRQs. In this context a study of X-ray spectra of a sample of FSRQs in different energy bands with XMM−Newton and other available X-ray facilities will be made. Different emission lines in high resolution X-ray spectra obtained from different X-ray observatory including spectra extracted from Reflection grating spectrometer (RGS) on board of XMM−Newton satellite mission will be studied and their origin will be investigated to understand the black hole physics, its dynamics and surrounding geometry and to estimate their mass. In addition to this, study of the soft excess emission in the energy range 0.1-3 keV found in Seyfert like FSRQs, e.g. 3C 273, 3C279 will be carried out mainly focusing on its origin.

In order to understand the variability pattern and classification of a sample of newly discovered blazars (BZCAT catalog), optical photometry in different optical bands will be carried out with observations taken by 1.3 m and 1.04 m telescopes at ARIES, Nainital, India during the period 2014–2015. For this sample there is no information about their behavior and physical condition in the literature.

We have undertaken the study of simultaneous multi-frequency correlation and spectral energy distribution (SED) of 3C 273 from radio to X-ray bands in different state of the source. We have made use of optical/UV and X-ray data from SMARTS optical/IR telescope and XMM-Newton satellite and Radio data at 4.8,

8.0, 14.5 22.2 and 36.8 GHz are collected from the University of Michigan Radio Astronomical Observatory (UMRAO), Crimean Astrophysical Observatory (CrAO) & Aalto University Metsahovi Radio Observatory in Finland. Temporal variation of its physical properties in the context of SED model parameters will be studied and corresponding emission mechanisms will be discussed.

$\star$ $\star$ $\star$ $\star$

References

Abdo, A. A., et al. 2010a, ApJ, 716, 30 77

Abdo, A. A., et al. 2010b, ApJS, 188, 405 78

Abdo, A. A., et al. 2011, ApJ, 730, 101 90

Abdo, A. A., et al. 2010c, ApJ, 714, L73 24, 54, 90, 133

Acero, F., et al. 2015, ApJS, 218, 23 78

Ackermann, M., et al. 2012, ApJ, 751, 159 90

Agarwal, A., et al. 2015, MNRAS, 451, 3882 78, 93

Agudo, I., et al. 2011, ApJ, 735, L10 85

Aharonian, F., et al. 2002, A&A, 393, 89 78

Aharonian, F., et al. 2005, A&A, 430, 865 78

Aharonian, F., et al. 2007, ApJ, 664, L71 22

Akyuz, A., et al. 2013, A&A, 556, A71 88

Aller, M. F., Aller, H. D., & Hughes, P. A. 1992, ApJ, 399, 16 21

Andruchow, I., Romero, G. E., & Cellone, S. A. 2005, A&A, 442, 97 21

Antonucci, R. 1993, ARA&A, 31, 473 6, 13

Antonucci, R. R. J., & Miller, J. S. 1985, ApJ, 297, 621 13

REFERENCES

Attridge, J. M., Wardle, J. F. C., & Homan, D. C. 2005, ApJ, 633, L85 54

Baath, L. B., et al. 1991, A&A, 241, L1 124

Bachev, R., et al. 2011, A&A, 528, L10 91

Barthel, P. D. 1989, ApJ, 336, 606 13

Beaklini, P. P. B., & Abraham, Z. 2014, MNRAS, 437, 489 67

Beckmann, V., & Shrader, C. R. 2012, Active Galactic Nuclei, Wiley-VCH xx, 14

Begelman, M. C., Fabian, A. C., & Rees, M. J. 2008, MNRAS, 384, L19 22, 53

Bezler, M., Kendziorra, E., Staubert, R., Hasinger, G., Pietsch, W., Reppin, C., Truemper, J., & Voges, W. 1984, A&A, 136, 351 117

Blandford, R. D., & Königl, A. 1979, ApJ, 232, 34 8

Blandford, R. D., & Ostriker, J. P. 1978, ApJ, 221, L29 13

Blandford, R. D., & Payne, D. G. 1982, MNRAS, 199, 883 126

Błażejowski, M., Sikora, M., Moderski, R., & Madejski, G. M. 2000, ApJ, 545, 107 25

Boettcher, M. 2012, ArXiv e-prints 26

Bonning, E. W., et al. 2009, ApJ, 697, L81 91

Bottacini, E., et al. 2010, A&A, 509, A69 87

Böttcher, M., et al. 2003, ApJ, 596, 847 22, 90

Bowyer, C. S., Lampton, M., Mack, J., & de Mendonca, F. 1970, ApJ, 161, L1 96

Brightman, M., & Nandra, K. 2012, MNRAS, 422, 1166 55

Brinkman, A., et al. 1998, in Science with XMM 42

Caballero-Garcia, M. D., Papadakis, I. E., Nicastro, F., & Ajello, M. 2012, A&A, 537, A87 121

Carnerero, M. I., et al. 2015, MNRAS, 450, 2677 89

Chatterjee, R., et al. 2008, ApJ, 689, 79 90

Chernyakova, M., et al. 2007, A&A, 465, 147 56, 89, 95, 97, 98, 99, 113, 117, 120

Ciprini, S. 2005, Multifrequency variability of OJ 287 during the expected outburst, XMM-Newton Proposal 88

Ciprini, S., et al. 2007, Mem. Soc. Astron. Italiana, 78, 741 88

Clements, S. D., & Carini, M. T. 2001, AJ, 121, 90 90

Collmar, W., et al. 2000, A&A, 354, 513 54

Connolly, S. D., McHardy, I. M., Skipper, C. J., & Emmanoulopoulos, D. 2016, MNRAS, 459, 3963 122

Courvoisier, T. J.-L., et al. 2003, A&A, 411, L343 54, 98

Courvoisier, T. J.-L., & Camenzind, M. 1989, A&A, 224, 10 126

Courvoisier, T. J.-L., et al. 1987, A&A, 176, 197 56, 95

Dai, B. Z., et al. 2009, MNRAS, 392, 1181 54

Dai, Y., Wu, J., Zhu, Z.-H., Zhou, X., & Ma, J. 2011, AJ, 141, 65 89

Daniel, M. K., et al. 2005, ApJ, 621, 181 78

Della Ceca, R., Lamorani, G., Maccacaro, T., Wolter, A., Griffiths, R., Stocke, J. T., & Setti, G. 1994, ApJ, 430, 533 10

den Herder, J. W., et al. 2001, A&A, 365, L7 42

Dermer, C. D., & Schlickeiser, R. 1993, ApJ, 416, 458 25

Dickey, J. M., & Lockman, F. J. 1990, ARA&A, 28, 215 108

Edelson, R., Griffiths, G., Markowitz, A., Sembay, S., Turner, M. J. L., & Warwick, R. 2001, ApJ, 554, 274 78

REFERENCES

Edelson, R., Turner, T. J., Pounds, K., Vaughan, S., Markowitz, A., Marshall, H., Dobbie, P., & Warwick, R. 2002, ApJ, 568, 610 58, 81

Edge, D. O., Shakeshaft, J. R., McAdam, W. B., Baldwin, J. E., & Archer, S. 1959, MmRAS, 68, 37 2, 54

Emmanoulopoulos, D., Papadakis, I. E., McHardy, I. M., Arévalo, P., Calvelo, D. E., & Uttley, P. 2012, MNRAS, 424, 1327 120

Espaillat, C., Bregman, J., Hughes, P., & Lloyd-Davies, E. 2008, ApJ, 679, 182 56, 98

Esposito, V., Walter, R., Jean, P., Tramacere, A., Türler, M., Lähteenmäki, A., & Tornikoski, M. 2015, A&A, 576, A122 89, 99, 113, 120

Fabian, A. C., Rees, M. J., Stella, L., & White, N. E. 1989, MNRAS, 238, 729 112

Fan, J. H., Kurtanidze, O., Liu, Y., Richter, G. M., Chanishvili, R., & Yuan, Y. H. 2014, ApJS, 213, 26 54, 64

Fan, J. H., Peng, Q. S., Tao, J., Qian, B. C., & Shen, Z. Q. 2009, AJ, 138, 1428 54

Fanaroff, B. L., & Riley, J. M. 1974, MNRAS, 167, 31P 11

Fath, E. A. 1909, Popular Astronomy, 17, 504 2

Ferrero, E., Wagner, S. J., Emmanoulopoulos, D., & Ostorero, L. 2006, A&A, 457, 133 87

Foschini, L., et al. 2006, A&A, 453, 829 88, 98

Foschini, L., Tagliaferri, G., Ghisellini, G., Ghirlanda, G., Tavecchio, F., & Bonnoli, G. 2010, MNRAS, 408, 448 91

Fromm, C. M., et al. 2013, A&A, 551, A32 27

Fuhrmann, L., et al. 2006, A&A, 445, L1 91

Gaur, H., et al. 2015, MNRAS, 452, 4263 78, 90, 93

Gaur, H., Gupta, A. C., Lachowicz, P., & Wiita, P. J. 2010, ApJ, 718, 279 93

Gaur, H., et al. 2012a, MNRAS, 420, 3147 78, 131

Gaur, H., et al. 2012b, MNRAS, 420, 3147 78, 131

Gaur, H., et al. 2012c, MNRAS, 425, 3002 78, 79, 131

Gaur, H., Gupta, A. C., & Wiita, P. J. 2012, AJ, 143, 23 133

Ghisellini, G., Celotti, A., Fossati, G., Maraschi, L., & Comastri, A. 1998, MNRAS, 301, 451 24

Ghisellini, G., et al. 2010, MNRAS, 405, 387 88

Ghisellini, G., Foschini, L., Tavecchio, F., & Pian, E. 2007, MNRAS, 382, L82 91

Ghisellini, G., & Maraschi, L. 1989, ApJ, 340, 181 25

Ghisellini, G., & Tavecchio, F. 2008, MNRAS, 387, 1669 25, 56

Giebels, B., et al. 2002, ApJ, 571, 763 78

Giommi, P., et al. 2006, A&A, 456, 911 91

Giommi, P., Cavazzuti, E., Cutini, S., Tramacere, A., & Raino', S. 2009, in The Extreme Sky: Sampling the Universe above 10 keV, 40 24

Giommi, P., et al. 2008, A&A, 487, L49 24, 87

Giommi, P., et al. 1999, A&A, 351, 59 87

Gliozzi, M., Sambruna, R. M., Jung, I., Krawczynski, H., Horan, D., & Tavecchio, F. 2006, ApJ, 646, 61 120

González-Martín, O., & Vaughan, S. 2012, A&A, 544, A80 56, 98

Goyal, A., Gopal-Krishna, Wiita, P. J., Anupama, G. C., Sahu, D. K., Sagar, R., & Joshi, S. 2012, A&A, 544, A37 93

Grandi, P., & Palumbo, G. G. C. 2004, Science, 306, 998 97, 111, 117

REFERENCES

Gregory, P. C., & Taylor, A. R. 1981, ApJ, 248, 596 85

Greve, A., et al. 2002, A&A, 390, L19 54

Gu, M., & Cao, X. 2009, MNRAS, 399, 349 121, 122

Gupta, A. C., Banerjee, D. P. K., Ashok, N. M., & Joshi, U. C. 2004, A&A, 422, 505 22, 53

Gupta, A. C., Fan, J. H., Bai, J. M., & Wagner, S. J. 2008, AJ, 135, 1384 78, 85, 87, 89, 90, 93

Gupta, A. C., & Joshi, U. C. 2005, A&A, 440, 855 78

Gupta, A. C., et al. 2012, MNRAS, 425, 1357 23, 78, 93

Gupta, A. C., Srivastava, A. K., & Wiita, P. J. 2009, ApJ, 690, 216 63

Gupta, Kalita, A. C., Kalita, N., Gaur, H., & Duorah, K. 2016, ArXiv e-prints 133

Haardt, F., et al. 1998, A&A, 340, 35 63, 64, 96, 97

Haardt, F., & Maraschi, L. 1991, ApJ, 380, L51 97, 124

Harris, D. E., & Krawczynski, H. 2006, ARA&A, 44, 463 8

Hayashida, M., et al. 2012, ApJ, 754, 114 90

Hayashida, M., et al. 2015, ApJ, 807, 79 90, 120

Hazard, C., Mackey, M. B., & Shimmins, A. J. 1963, Nature, 197, 1037 2

Heckman, T. M. 1980, A&A, 87, 152 11

Heidt, J., & Wagner, S. J. 1996, A&A, 305, 42 78, 87

Ho, L. C., Filippenko, A. V., & Sargent, W. L. W. 1994, in IAU Symposium, Vol. 159, Multi-Wavelength Continuum Emission of AGN, ed. T. Courvoisier & A. Blecha, 275 11

Jansen, F., et al. 2001, A&A, 365, L1 34

Jester, S., Meisenheimer, K., Martel, A. R., Perlman, E. S., & Sparks, W. B. 2007, MNRAS, 380, 828 54, 74

Jester, S., Röser, H.-J., Meisenheimer, K., & Perley, R. 2005, A&A, 431, 477 54

Jethwa, P., Saxton, R., Guainazzi, M., Rodriguez-Pascual, P., & Stuhlinger, M. 2015, A&A, 581, A104 46

Jorstad, S. G., et al. 2010, ApJ, 715, 362 90

Jorstad, S. G., et al. 2005, AJ, 130, 1418 95

Jorstad, S. G., Marscher, A. P., Mattox, J. R., Aller, M. F., Aller, H. D., Wehrle, A. E., & Bloom, S. D. 2001, ApJ, 556, 738 27, 95

Jorstad, S. G., et al. 2013, ApJ, 773, 147 91

Joshi, M., & Böttcher, M. 2011, ApJ, 727, 21 26

Joshi, M., Marscher, A. P., & Böttcher, M. 2014, ApJ, 785, 132 94

Kalita, N., Gupta, A. C., Wiita, P. J., Bhagwan, J., & Duorah, K. 2015, MNRAS, 451, 1356 81, 89, 93, 98, 105

Kaspi, S., Smith, P. S., Netzer, H., Maoz, D., Jannuzi, B. T., & Giveon, U. 2000, ApJ, 533, 631 56

Kataoka, J., Tanihata, C., Kawai, N., Takahara, F., Takahashi, T., Edwards, P. G., & Makino, F. 2002, MNRAS, 336, 932 54, 55, 97, 111, 118, 120, 122

Kellermann, K. I., Sramek, R., Schmidt, M., Shaffer, D. B., & Green, R. 1989, AJ, 98, 1195 10

Kembhavi, A. K., & Narlikar, J. V. 1999, Quasars and Active Galactic Nuclei 18

Khachikian, E. Y., & Weedman, D. W. 1974, ApJ, 192, 581 10

Kirsch, M. G. K., et al. 2014, SpaceOps Conferences 33

Kohler, S., & Nalewajko, K. 2015, MNRAS, 449, 2901 91

REFERENCES

Konopelko, A., Mastichiadis, A., Kirk, J., de Jager, O. C., & Stecker, F. W. 2003, ApJ, 597, 851 78

Koski, A. T. 1978, ApJ, 223, 56 7

Krawczynski, H., Coppi, P. S., & Aharonian, F. 2002, MNRAS, 336, 721 78

Krawczynski, H., et al. 2004, ApJ, 601, 151 120

Krolik, J. H. 1999, ApJ, 515, L73 17

Lachowicz, P., Gupta, A. C., Gaur, H., & Wiita, P. J. 2009, A&A, 506, L17 93

Laor, A. 1991, ApJ, 376, 90 112

Lawrence, A. 1987, PASP, 99, 309 10

Lawrence, A. 1993, in The Nearest Active Galaxies, ed. J. Beckman, L. Colina, & H. Netzer, 3 10

Leach, C. M., McHardy, I. M., & Papadakis, I. E. 1995, MNRAS, 272, 221 55, 95, 117

Liu, L., & Zhang, Y. 2011, Journal of Astrophysics and Astronomy, 32, 173 55

Livio, M., Pringle, J. E., & King, A. R. 2003, ApJ, 593, 184 126

Lumb, D. H., Schartel, N., & Jansen, F. A. 2012, ArXiv e-prints xx, 33

Madejski, G., Takahashi, T., Tashiro, M., Kubo, H., Hartman, R., Kallman, T., & Sikora, M. 1996, ApJ, 459, 156 93

Madsen, K. K., et al. 2015, ApJ, 812, 14 120

Malkan, M. A., & Sargent, W. L. W. 1982, ApJ, 254, 22 17

Mangalam, A. V., & Wiita, P. J. 1993, ApJ, 406, 420 53

Mannheim, K., & Biermann, P. L. 1992, A&A, 253, L21 26

Mantovani, F., Junor, W., McHardy, I. M., & Valerio, C. 2000, A&A, 354, 497 54

Marscher, A. P. 1996, in Astronomical Society of the Pacific Conference Series, Vol. 110, Blazar Continuum Variability, ed. H. R. Miller, J. R. Webb, & J. C. Noble, 248 8, 26, 27, 73

Marscher, A. P. 2014, ApJ, 780, 87 73

Marscher, A. P., & Gear, W. K. 1985, ApJ, 298, 114 xx, 25, 26, 27

Marscher, A. P., Gear, W. K., & Travis, J. P. 1992, in Variability of Blazars, ed. E. Valtaoja & M. Valtonen, 85 94

Marscher, A. P., et al. 2010, ApJ, 710, L126 90

Mason, K. O., et al. 2001, A&A, 365, L36 41, 58

Massaro, E., et al. 2003, A&A, 399, 33 88

Massaro, E., Nesci, R., Maesano, M., Montagni, F., & D'Alessio, F. 1998, MNRAS, 299, 47 90

Massaro, E., Perri, M., Giommi, P., Nesci, R., & Verrecchia, F. 2004, A&A, 422, 103 78

McHardy, I., Lawson, A., Newsam, A., Marscher, A., Robson, I., & Stevens, J. 1999, MNRAS, 310, 571 55, 124

McHardy, I., Lawson, A., Newsam, A., Marscher, A. P., Sokolov, A. S., Urry, C. M., & Wehrle, A. E. 2007, MNRAS, 375, 1521 54, 57

McHardy, I. M. 2013, MNRAS, 430, L49 56

Miller, H. R., Carini, M. T., & Goodrich, B. D. 1989, Nature, 337, 627 78

Mimica, P., Aloy, M. A., Müller, E., & Brinkmann, W. 2004, A&A, 418, 947 26

Mohan, P., Mangalam, A., Chand, H., & Gupta, A. C. 2011, Journal of Astrophysics and Astronomy, 32, 117 56

Molendi, S., & Sembay, S. 2003, XMM-SOC-CAL-TN-0036 50

Montagni, F., Maselli, A., Massaro, E., Nesci, R., Sclavi, S., & Maesano, M. 2006, A&A, 451, 435 78

Mücke, A., Protheroe, R. J., Engel, R., Rachen, J. P., & Stanev, T. 2003, Astroparticle Physics, 18, 593 26

Mukherjee, R., et al. 1997, ApJ, 490, 116 77

Nandra, K. 2006, MNRAS, 368, L62 111

Nandra, K., George, I. M., Mushotzky, R. F., Turner, T. J., & Yaqoob, T. 1997, ApJ, 477, 602 111

Nandra, K., Le, T., George, I. M., Edelson, R. A., Mushotzky, R. F., Peterson, B. M., & Turner, T. J. 2000, ApJ, 544, 734 124

Nandra, K., & Papadakis, I. E. 2001, ApJ, 554, 710 124

Neronov, A., Semikoz, D., Taylor, A. M., & Vovk, I. 2015, A&A, 575, A21 86

Netzer, H. 2013, book 19

Nolan, P. L., et al. 2012, ApJS, 199, 31 78

Orr, M. J. L., & Browne, I. W. A. 1982, MNRAS, 200, 1067 13

Osterbrock, D. E. 1978, Proceedings of the National Academy of Science, 75, 540 13

Pacciani, L., et al. 2009, A&A, 494, 49 54, 113

Pacciani, L., Tavecchio, F., Donnarumma, I., Stamerra, A., Carrasco, L., Recillas, E., Porras, A., & Uemura, M. 2014, ApJ, 790, 45 91

Paczynski, B. 1978, Acta Astron., 28, 241 8

Padovani, P. 1993, MNRAS, 263, 461 10

Padovani, P., & Giommi, P. 1995, MNRAS, 277, 1477 10, 77

Page, K. L., Turner, M. J. L., Done, C., O'Brien, P. T., Reeves, J. N., Sembay, S., & Stuhlinger, M. 2004, MNRAS, 349, 57 56, 63, 64, 89, 95, 96, 98, 111, 113, 120, 124

Paliya, V. S. 2015, ApJ, 804, 74 88

Palma, N. I., et al. 2011, ApJ, 735, 60 86

Paltani, S., Courvoisier, T. J.-L., & Walter, R. 1998, A&A, 340, 47 96

Paltani, S., & Türler, M. 2005, A&A, 435, 811 56

Papadakis, I. E., Villata, M., & Raiteri, C. M. 2007, A&A, 470, 857 90

Peterson, B. M. 1997, An introduction to active galactic nuclei 4, 5, 6, 11, 12, 13

Pian, E., et al. 2006, A&A, 449, L21 91

Pietrini, P., & Torricelli-Ciamponi, G. 2008, A&A, 479, 365 55, 56, 63, 64, 89, 95, 101

Ponti, G., Miniutti, G., Cappi, M., Maraschi, L., Fabian, A. C., & Iwasawa, K. 2006, MNRAS, 368, 903 121

Raino', S., Cavazzuti, E., Colafrancesco, S., Giommi, P., Tramacere, A., & the Fermi-LAT Collaboration. 2009, ArXiv e-prints xx, 23

Raiteri, C. M., et al. 2001, A&A, 377, 396 85

Raiteri, C. M., et al. 2010, A&A, 524, A43 91

Raiteri, C. M., et al. 2009, A&A, 507, 769 90

Raiteri, C. M., et al. 2013, MNRAS, 436, 1530 90

Raiteri, C. M., et al. 2005, A&A, 438, 39 85

Raiteri, C. M., Villata, M., Kadler, M., Krichbaum, T. P., Böttcher, M., Fuhrmann, L., & Orio, M. 2006, A&A, 452, 845 85

Raiteri, C. M., et al. 2008, A&A, 491, 755 91

Raiteri, C. M., et al. 2007, A&A, 473, 819 91

Rani, B., Lott, B., Krichbaum, T. P., Fuhrmann, L., & Zensus, J. A. 2013, A&A, 557, A71 67

Ravasio, M., et al. 2002, A&A, 383, 763 90

Ravasio, M., Tagliaferri, G., Ghisellini, G., Tavecchio, F., Böttcher, M., & Sikora, M. 2003, A&A, 408, 479 90

Reeves, J. N., et al. 2001, A&A, 365, L116 87

Reynolds, C. S. 2001, in Astronomical Society of the Pacific Conference Series, Vol. 224, Probing the Physics of Active Galactic Nuclei, ed. B. M. Peterson, R. W. Pogge, & R. S. Polidan, 105 111

Reynolds, C. S., & Nowak, M. A. 2003, Phys. Rep., 377, 389 xix, 8, 9

Robson, E. I., et al. 1993, MNRAS, 262, 249 95

Romero, G. E., Cellone, S. A., & Combi, J. A. 1999, A&AS, 135, 477 79

Romero, G. E., Cellone, S. A., & Combi, J. A. 2000, A&A, 360, L47 85

Rybicki, G. B., & Lightman, A. P. 1979, Radiative Processes in Astrophysics 18, 125

Sambruna, R. M., Maraschi, L., & Urry, C. M. 1996, ApJ, 463, 444 94

Sambruna, R. M., Tavecchio, F., Ghisellini, G., Donato, D., Holland, S. T., Markwardt, C. B., Tueller, J., & Mushotzky, R. F. 2007, ApJ, 669, 884 87, 88

Sambruna, R. M., Urry, C. M., Tavecchio, F., Maraschi, L., Scarpa, R., Chartas, G., & Muxlow, T. 2001, ApJ, 549, L161 54

Sasada, M., et al. 2014, ApJ, 784, 141 91

Savolainen, T., Wiik, K., Valtaoja, E., & Tornikoski, M. 2006, A&A, 446, 71 54

Scheuer, P. A. G., & Readhead, A. C. S. 1979, Nature, 277, 182 13

Schmidt, M. 1963, Nature, 197, 1040 3, 54, 89

Schmitt, J. L. 1968, Nature, 218, 663 3

Schneider, P. 2006, Extragalactic Astronomy and Cosmology, An Introduction 4, 5, 6

Schwadron, N. A., Lee, M. A., & McComas, D. J. 2008, ApJ, 675, 1584 26

Seyfert, C. K. 1943, ApJ, 97, 28 2

Shakura, N. I., & Sunyaev, R. A. 1973, A&A, 24, 337 5, 16

Shemmer, O., Brandt, W. N., Netzer, H., Maiolino, R., & Kaspi, S. 2006, ApJ, 646, L29 121

Sikora, M., Begelman, M. C., & Rees, M. J. 1994, ApJ, 421, 153 25, 56

Sillanpaa, A., Haarala, S., Valtonen, M. J., Sundelius, B., & Byrd, G. G. 1988, ApJ, 325, 628 88

Slipher, V. M. 1917, Lowell Observatory Bulletin, 3, 59 2

Sobolewska, M. A., & Papadakis, I. E. 2009, MNRAS, 399, 1597 121

Sobolewska, M. A., Papadakis, I. E., Done, C., & Malzac, J. 2011, MNRAS, 417, 280 122

Soldi, S., et al. 2008, A&A, 486, 411 54, 55, 89, 97, 98, 120

Spada, M., Ghisellini, G., Lazzati, D., & Celotti, A. 2001, MNRAS, 325, 1559 26

Strüder, L., et al. 2001, A&A, 365, L18 38, 50, 58, 81

Sunyaev, R. A., & Titarchuk, L. G. 1980, A&A, 86, 121 117, 125

Swanenburg, B. N., et al. 1978, Nature, 275, 298 56

Tagliaferri, G., et al. 2015, ApJ, 807, 167 88

Tanaka, Y. T., et al. 2013, ApJ, 777, L18 86

Taylor, R. D., Uttley, P., & McHardy, I. M. 2003, MNRAS, 342, L31 121

Trippe, S., et al. 2011, A&A, 533, A97 124

Türler, M., et al. 2006, A&A, 451, L1 56, 96, 113

Türler, M., Courvoisier, T. J.-L., & Paltani, S. 2000, A&A, 361, 850 95

Turner, M. J. L., et al. 2001, A&A, 365, L27 38

Turner, M. J. L., Courvoisier, T., Staubert, R., Molteni, D., & Trumper, J. 1985, Space Sci. Rev., 40, 623 56, 89, 96

Turner, M. J. L., et al. 1990, MNRAS, 244, 310 96, 111, 120

Turner, T. J., Miller, L., Reeves, J. N., & Kraemer, S. B. 2007, A&A, 475, 121 121

Urry, C. M., & Padovani, P. 1995, PASP, 107, 803 xix, 5, 13, 15, 21, 96

Urry, C. M., Scarpa, R., O'Dowd, M., Falomo, R., Pesce, J. E., & Treves, A. 2000, ApJ, 532, 816 13

Vagnetti, F., Turriziani, S., & Trevese, D. 2011, A&A, 536, A84 55

Valtonen, M. J., et al. 2006, ApJ, 643, L9 89

Valtonen, M. J., et al. 2009, ApJ, 698, 781 89

Vandenbroucke, J., et al. 2010, ApJ, 718, L166 85

Vaughan, S., Edelson, R., Warwick, R. S., & Uttley, P. 2003, MNRAS, 345, 1271 62, 84

Vercellone, S., et al. 2008, ApJ, 676, L13 91

Villata, M., et al. 2006, A&A, 453, 817 91

Villata, M., et al. 2002, A&A, 390, 407 90

Villforth, C., et al. 2010, MNRAS, 402, 2087 89

Wagner, S. J., & Witzel, A. 1995, ARA&A, 33, 163 22, 53

Walter, R., & Courvoisier, T. J.-L. 1990, A&A, 233, 40 125

Walter, R., & Courvoisier, T. J.-L. 1992, A&A, 258, 255 97, 99, 117, 118, 124, 125

Wen, S.-l., Peng, Z.-m., Fan, J.-h., & Xie, G.-z. 2002, Chinese Astron. Astrophys., 26, 398 54

Wiita, P. J. 1996, in Astronomical Society of the Pacific Conference Series, Vol. 110, Blazar Continuum Variability, ed. H. R. Miller, J. R. Webb, & J. C. Noble, 42 73

Woltjer, L. 1959, ApJ, 130, 38 2

Wu, Q., & Gu, M. 2008, ApJ, 682, 212 121

Yaqoob, T., & Serlemitsos, P. 2000, ApJ, 544, L95 96, 111

Younes, G., Porquet, D., Sabra, B., & Reeves, J. N. 2011, A&A, 530, A149 121, 122

Zhai, M., & Wei, J. Y. 2012, A&A, 538, A125 90

Zhang, Y. H. 2010, ApJ, 713, 180 87

Zhang, Y. H., et al. 2002, ApJ, 572, 762 78